SCANNING PROBE MICROSCOPY STUDY OF MOLECULAR NANOSTRUCTURES ON 2D MATERIALS

Chuanhui Chen

Dissertation submitted to the faculty of the Virginia Polytechnic Institute and State University in partial fulfillment of the requirements for the degree of

Doctor of Philosophy
In
Physics

Chenggang Tao
(Committee Chair)
Hans Robinson
Jean Joseph Heremans
Shengfeng Cheng

June 30, 2017
Blacksburg, VA

Keywords: Scanning Tunneling Microscope (STM), Thermal Evaporation, Atomic Force Microscopy (AFM), Two-Dimensional (2D) Materials, One-Dimensional (1D) Nanostructures

SCANNING PROBE MICROSCOPY STUDY OF MOLECULAR NANOSTRUCTURES ON 2D MATERIALS

Chuanhui Chen

ABSTRACT (academic)

Molecules adsorbed on two-dimensional (2D) materials can show interesting physical and chemical properties. This thesis presents scanning probe microscopy (SPM) investigation of emerging 2D materials, molecular nanostructures on 2D substrates at the nanometer scale, and biophysical processes on the biological membrane. Two main techniques of nano-probing are used: scanning tunneling microscopy (STM) and atomic force microscopy (AFM). The study particularly emphasizes on self-assembled molecules on flat and curved 2D materials.

First, we report the preparation of novel 1D C_{60} nanostructures on rippled graphene. Through careful control of the subtle balance between the linear periodic potential of rippled graphene and the C_{60} surface mobility, we demonstrate that C_{60} molecules can be arranged into a 1D C_{60} chain structure of two to three molecules in width. At a higher annealing temperature, the 1D chain structure transitions to a more closely packed, quasi-1D hexagonal stripe structure. The experimental realization of 1D C_{60} structures on graphene is, to our knowledge, the first in the field. It could pave the way for fabricating new C_{60}/graphene hybrid structures for future applications in electronics, spintronics and quantum information.

Second, we report a study on nano-morphology of potential operative donors (e.g., C_{60}) and acceptors (e.g., perylenetetracarboxylic dianhydride, aka. PTCDA) on wrinkled graphene supported by copper foils. We realize sub-monolayer C_{60} and PTCDA on quasi-1D and quasi-2D real periodic wrinkled graphene, by carefully controlling the deposition parameters of both molecules. Our successful realization of acceptor-donor binary nanostructures on wrinkled graphene could have important implications in future development of organic solar cells.

Third, we report an STM and spectroscopy study on atomically thin transition-metal dichalcogenides (TMDCs) material. TMDCs are 2D materials that emerged recently due to their intriguing physical properties and potential applications. In particular, our study focuses on molybdenum disulfide (MoS_2) mono- to few-layers and pyramid nanostructures synthesized through chemical vapor deposition. We observe an intriguing curved region near the edge

terminals on the few-layered MoS_2 nanoplatelets grown on gallium nitride (GaN) as well as the pyramid nanostructures grown on the highly oriented pyrolytic graphite (HOPG). The measured band gap in these curved regions is consistent with the direct band gap in MoS_2 monolayers. The curved features near the edge terminals and the associated electronic properties may contribute to understanding catalytic behaviors of MoS_2 nanostructures and have potential applications in future electronic devices and catalysts based on MoS_2 nanostructures.

Finally, we report a liquid-cell AFM study on the endosomal protein sorting process on the biological lipid membranes, a different type of 2D materials. The sorting mechanism relies on complex forming between Tom1 and the cargo sorting protein, Toll interacting protein (Tollip). The induced conformational change in Tollip triggers its dissociation from the lipid membrane and commitment to cargo trafficking. This collaborative study aims at characterizing the dynamic interaction between Tollip and the lipid membrane. To study this process we develop the liquid mode of AFM. We successfully demonstrate that Tollip is localized to the lipid membrane via association with PtdIns3P (PI(3)P), a major phospholipid in the cell membrane involved in protein trafficking.

SCANNING PROBE MICROSCOPY STUDY OF MOLECULAR NANOSTRUCTURES ON 2D MATERIALS

Chuanhui Chen

General Audience Abstract

Two-dimensional (2D) materials are layered materials with thickness of single atom or few atoms. The ultimate thickness leads to novel properties that are useful for a wide range of applications in photovoltaics, electronics and quantum information. In order to explore these properties at the nanometer scale, we used scanning probe techniques, i.e., scanning tunneling microscopy (STM) and atomic force microscopy (AFM), to perform comprehensive investigations on these emerging materials.

2D materials, such as graphene and atomically thin transition-metal dichalcogenides (TMDCs), are promising candidates for building economic, safe and mechanically flexible solar cells with desirable optical and electronic properties, e.g. tunable sunlight absorption. The first part of the thesis focuses on graphene, a single-atom-thick carbon sheet. We deposited key components in organic solar cells, such as perylenetetracarboxylic dianhydride (PTCDA) and C_{60} molecules, on graphene. On these materials we observed various novel nanostructures, like quasi-1D C_{60} nanochains. The second part of the thesis focuses on mono- to few-layered MoS_2, which can be used as an active layer in high-efficiency solar cells. Our study has important implications in improving efficiency of organic solar cells in the future.

In the final part of the thesis, we extended our subject to the biological lipid membrane, a 2D material critical in biology, and biophysical processes occurring on the membrane. Using a liquid-cell AFM, we investigated the endosomal protein sorting process on the biological membranes. Our study contributes to understanding of the interactions between the adaptor proteins and cell membranes in the protein sorting process that guides proteins to their proper destinations.

Dedication

To my parents: Junye Chen and Chuanhua Wang

To my husband: Zuoping Zhang

Acknowledgements

I would express deep gratitude to my research advisor, Professor Chenggang Tao, for his academic guidance and support during my PhD training. He has been my role model as a scientific researcher. He always encouraged me to independently and bravely try a lot of experiments. He also gave me rigorous training on the domain knowledge, as well as methodology, in physics. Overall, he taught me how to be a good experimenter in physics.

I am grateful to many faculty members in the Physics Department. Professor Shengfeng Cheng, as one of my committee members, taught me to learn physics more intuitively, without heavily depending on mathematics. Professor Jean Joseph Heremans guided me to schedule my exams carefully. Professor Hans Robinson gave me good suggestions on scientific presentation. Professor James R. Heflin helped and supported me in the program of organic solar cells. Professor Daniel Capelluto, our collaborator on the biophysical project, helped me understand membrane trafficking and protein degradation. Professor Giti Khodaparast encouraged me a lot in my PhD study and life.

The Nano Probe Lab has prepared me well for the PhD degree. It is a small, yet supportive and collegial group. I particularly want to thank Adam Mills, who helped me a lot in operating the instruments, and Bevin Huang, who helped me a lot in my first publication. Both were undergraduate students at Virginia Tech. I also need to thank Husong Zheng and Fan Zhang, who helped me a lot in the theoretical calculation in my projects.

A huge thank to Yanlong Li, for teaching me how to run an AFM, as well as for numerous other favors during our collaboration. I also need to thank Xiong Wen, my collaborator in the Biological Department, for helping me a lot for understanding biology and for editing my writing in Chapter 6.

Table of Contents

List of Figures

Chapter 2

Chapter 3

Chapter 4

Chapter 5

Chapter 6

Chapter 1. Introduction

1.1 Motivation

1.1.1 2D Materials

Two-dimensional (2D) materials, also referred to as single-layer or atomically-thin materials, have attractive characteristics and countless applications in semiconductors, photovoltaics, and electrodes [5-13]. Graphene is the first discovered 2D material, extracted from bulk graphite with micromechanical cleavage techniques introduced by Andre Geim and Konstantin Novoselov in 2004 [14]. A single layer of graphene consists of a honeycomb lattice of sp^2 hybridized carbon atoms. It is this bonding arrangement that makes graphene unique, exhibiting fascinating physical properties with numerous potential applications [15, 16]. Significant effort has recently been given to studying the adsorption and desorption of different molecules on graphene, and to further optimize the molecule/graphene hybrid structures in order to better understand the unique physical and chemical properties of graphene. For those studies, graphene grown by chemical vapor deposition (CVD) on different metals (Cu, Ru, Ir, Pt, Ni) is regarded as an ideal platform, providing scalable production of high-quality graphene [17, 18]. Thus, a lot of scientific research has already been focused on synthesizing large continuous graphene sheets through various ways and on different substrates [17, 19-25]. Recent advancements in organic photovoltaic cells use graphene as a flexible transparent electrode because of its high transparency, physical flexibility, huge abundance, and semi-metallic conductivity [27-32]. Beyond graphene, there has also been a large effort focused on other 2D materials due to their unusual characteristics. Atomically-thin transition-metal dichalcogenides (TMDCs) are another family of 2D materials because of their semiconducting and photonic properties [5-13]. TMDCs materials have the chemical formula, MX_2, with the M standing for the transition metal element (Mo, W, Ti, Ta, …) and the X signifying the chalcogenide element (S, Se, and Te). In the family of layered TMDCs, MoS_2 is a widely used semiconductor material, composed of planar atomic thin S-Mo-S sandwich layers held together by van der Waals interactions [26]. The bulk form of MoS_2 has been extensively studied for decades as solid lubricant [27-29]. Recently, mono- to few-layered MoS_2 has captured increasing broad applications due to its optical, electronic, and catalytic properties [11, 30-42]. More specifically,

atomically-thin MoS_2 can be utilized as a hole-transport layer, electron-transport layer, interfacial layer, and protective layer in fabricating heterojunctions solar cells [43, 44].

1.1.2 1D Nanostructures

Research during the recent decades has been very proficient at studying phenomena at the microscale, but only very recently becomes effective at studying nanoscale phenomena. Already, their particular properties and potential applications are promising for microelectronics and optoelectronics applications as the rising demand for small, delicate electronic systems naturally stimulates further research on these smaller dimensional nanostructures. Electronic and optoelectronic devices are very common in modern society in simple household equipment or in sophisticated hospital instruments, computers, and signal transmission equipment. The rising demand for the smaller and also delicate electronic systems stimulates the development of research on the smaller dimensional nanostructures. As such, 1D nanostructure will potentially break through the physical and economic limitations of the microelectronic industry, reduce energy consumption, and increase the speed of future electronic and optoelectronic devices [45, 46].

1D nanostructures transfer electrons or holes more effectively in one dimension due to the reduction in dimensionality from 3D and even 2D materials, and from the fewer defects present in these nanostructures. They can be synthesized into a single crystal form with controlled core conditions during growth, and are stable as nanotubes, nanorods, nanowires, and nanobelts [45, 47-52]. Functional devices with these 1D nanostructures have been realized, ranging from field-effect transistors and ultraviolet detectors, to light-emitting diodes, p-n diodes, nano-lasers, and single nanowire solar cells [45-47, 53-56]. Furthermore, compared to 2D materials, 1D nanostructures with fewer defects or grain boundaries offer inherent charge transport properties [57-59].

1.1.3 Organic Solar Cells

The rapid increase of power conversion efficiencies in organic solar cells has given rise to recent scientific and economic interests to an otherwise aging field developed over forty years ago. Although organic materials have a relatively poor charge-carrier mobility, most of the organic

semiconductors have a large optical band gap around 2 eV, higher than that of silicon, and thus enlarge the spectrum of the solar systems [60]. This, along with the physical flexibility to meet different requirements as well as the advantage of lower cost, larger-scale production capacity, and stronger light absorption coefficients, still promotes its development [61]. Solar cells can be divided into three main generations according to their different junction types: single layer, bilayer heterojunctions, and bulk heterojunctions [62]. For the single layer device, the efficiency is typically well below 0.1% with poor ability to split the exciton pairs [63-65]. For bilayer solar cells, the efficiency is less than 1% due to the much smaller fraction of excitons that can diffuse to the interface of layers and thus split into carriers [66]. The diffusion length of excitons is around 10 nm, much shorter than the thickness of the active layers in bilayer heterojunctions, which is on the order of 100 nm in order to effectively absorb sunlight. The bulk heterojunctions have mixed absorption layers consisting of donor and acceptor organic molecules or polymers on the order of nanometers, allowing excitons to reach an interface within their short lifetimes and dissociate at the large donor-acceptor interfacial surface, so the efficiency has significantly increased to about 10%, but still very low compared to the inorganic solar cells (up to 46%), so there is an urgent need to improve the efficiency of organic solar cells in order to capitalize on the aforementioned advantages of them [67-71]. The bilayer and bulk heterojunctions are based on two types of organic materials: electron donor and electron acceptor. Firstly, the donor-acceptor heterojunctions take advantage of the photon to separate the electron from the hole in the electron donor material. Then, the electron transfers from the excited state of the donor (lowest unoccupied molecular orbital, LUMO) to the LUMO of the acceptor, which must be a good electron acceptor with a stronger electron affinity. Subsequently, the electron and the hole have to reach the opposite electrodes, the cathode and the anode, respectively. Thus a direct current can be achieved to an outer circuit [72, 73]. Almost all the research is focused on improving the power efficiency of organic solar cells. Various factors would impact it, such as: solvent/thermal annealing conditions, weight ratio of acceptor and donor materials, thickness of active layers and as well as other synthesis parameters [74-77]. Since the active layers are critical determining factors in the performances of organic solar cells, the challenging part of making effective organic solar cells becomes how to choose the right donor and acceptor combinations [78]. There are many choices for donor and acceptor materials proposed by previous studies [70, 73, 79-86]. There are also numerous types of organic solar cells including small molecule-small molecule, small molecule-polymer, and polymer-polymer [78, 87-

92]. In these new studies, C_{60} combined with graphene as its transparent electrode has been investigated, which gave us a hint about the combination of organic solar cells and 2D materials. Although there are thousands of papers about organic solar cells, few of them talk about the nanoscale characteristics, so the nanostructure of donor and acceptor materials for organic solar cells needs more SPM research [93].

1.2 Outline of This Thesis

All the content above is a compact review on the popular 2D materials, novel 1D nanostructures, and advantages of organic solar cells. The development and importance of 2D materials is the starting point of this thesis. In the motivation part, we also explained the rising demands of 1D nanostructures, and also the application and development of organic solar cells.

In chapter 2, we will introduce the physical mechanism of the STM—quantum tunneling. I will mainly introduce the Omicron STM designs including the electronics, the pumping system, and the vibration isolation mechanisms. A home-made Knudsen cell is mounted in our STM system in order to perform molecular deposition. I will illustrate the components, parts, and also the complete version of the load lock part in the form of photos. Besides the experiments done with STM, I also do a lot of measurements in AFM, so I briefly introduce the different measuring modes and also the mechanism of it.

In chapter 3, we will show and discuss the formation of the quasi-1D C_{60} nanostructures on rippled graphene. Rippled graphene provides a novel quasi-1D template for C_{60} molecules, where C_{60} molecules accommodate themselves to forming a quasi-1D chain structure. This kind of hybrid structure is pretty sensitive to the thermodynamic effect, so we explore a new quasi-1D C_{60} stripe nanostructure after a gentle annealing. We will use 3D schematic models to compare the chain structure and the stripe structure. We also demonstrate that rippled graphene is formed on the Cu(100) facet. Finally we will discuss the formation of the bimolecular chains and the trimolecular chains, and the mechanism how these two typical chain nanostructures transform into the C_{60} stripe structure after gentle annealing.

In chapter 4, firstly, we will talk about this new graphene wrinkles forming 1D and 2D structures. And we will discuss the formation of this kind of novel quasi-1D or quasi-2D wrinkled graphene substrate. Secondly we will show and discuss the formation of the quasi-self-assembled

C_{60} and PTCDA nanostructures on quasi-1D or quasi-2D wrinkled graphene. These real wrinkles have the modulation in the range of 0.2 nm to 0.4 nm, can provide a novel suspended template for C_{60} and PTCDA molecules, where C_{60} molecules can still form quasi-hexagonal close-packed structure, and PTCDA also can still accommodate the wrinkled graphene with the herringbone pattern too. Meanwhile we will discuss the differences between this graphene wrinkles and moiré patterned graphene ripples (in chapter 3) from the aspects of the van der Waals binding energies. We also find an interesting dynamic decay process of PTCDA on flat graphene substrate.

In chapter 5, we examine mono- to few-layered MoS_2 nanoplatelets and MoS_2 pyramid nanostructures on gallium nitride (GaN) and highly ordered pyrolytic graphite (HOPG) by using STM and STS. We firstly observe characteristic curved ripple regions close to the edge terminals of MoS_2 on both GaN and HOPG substrates through STM measurement. The STS measurement on the curved regions reveals a band gap of 1.96 ± 0.10 eV, which is larger than the band gap of bulk material. Finally we will discuss the reason of the discrepancy of band gaps on the curved regions and on basal planes.

In chapter 6, we will introduce the effect of Tom1 in mediating Tollip's dissociation from PtdIns3P (PI(3)P) and committing Tollip to cargo trafficking. Then the mechanism of the liquid mode of AFM will be illustrated. After that, we will show the surface of mica substrate, the morphology of suspended lipid bilayers (SLBs), the morphology of Tollip on SLBs, and finally we successfully demonstrate that the Tollip is located on the endosome membrane via association with PI(3)P.

In chapter 7, we will summarize this dissertation briefly and propose possible works in the future.

Chapter 2. Experimental Methods—Scanning Probe Microscopy

To characterize the morphology of molecules and atoms, a tool with nanometer spatial resolution is essential in observing and mapping these nano-structures at the atomic scale. In addition, the measurements need to be non-destructive, i.e. the structure should not be distorted or damaged during the measurement process. Scanning tunneling microscopy (STM) is a fitting choice due to its ultra-high atomic resolution, ultra-high vacuum, and weak sample interactions compared to other measurement tools. In this thesis, all STM experiments are performed using the ultrahigh vacuum (UHV) STM from Omicron Nanotechnology at a base pressure of 1×10^{-10} Torr.

In this chapter, STM will be introduced, including the brief history of STM development and the fundamental physical mechanism of it. Then we will show the main designs for the Omicron STM in our lab. Finally, we will explain the other important parts mounted in our STM including the thermal evaporator.

2.1 Introduction to Scanning Tunneling Microscopy

STM was invented by Gerd Binnig and Heinrich Rohrer at the IBM Zurich Research Lab in 1982, and they won the Nobel Prize in physics as a result in 1986 [94, 95]. Since then, a variety of STMs with different sizes in different environments have been designed over a wide range of pressures and temperatures [96-101]. The versatility and precision of the STM has made it one of the most advanced atomic structure probing instruments in the world.

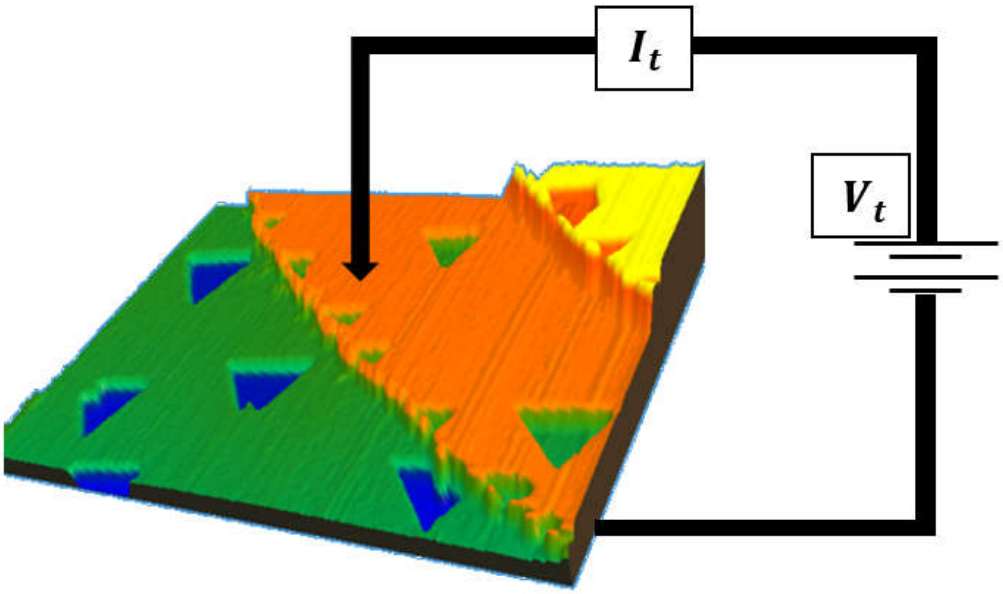

Fig. 2.1. Schematic diagram of the basic characterizing mechanism of STM.

Fig. 2.1 shows the fundamental working diagram of STM. There are two widely-used operating modes of STM: constant-current mode and constant-height mode. In constant-current mode, the more frequently used mode of the two, a feedback circuit is used to compare the tunneling current with a preset current. This allows the real-time adjustment of the vertical positioning of the tip with respect to the sample surface (z-position). Constant-height measurements, on the other hand, keep the tip at a constant z-position so that the location-varying tunneling current will be mapped when it scans over the sample surface. From the diagram, we can see the atomically-sharp conducting tip at the nanometer scale as well as the scanned sample. I will take the constant-current mode as an example to explain the working mechanism of STM. A bias voltage V_t is applied between the sharp tip and scanned sample so that a current forms in this circuit even with an open vacuum gap due to the quantum tunneling effect. When the tip moves parallel to the sample plane, i.e. varying the tip location (x, y), the tunneling current changes, an indicator for the feedback circuit to adjust the distance z between the tip and the scanning point. The morphology of the sample at that particular point z(x, y) on the surface can be detected after finishing one measurement.

2.1.1 Quantum Tunneling Current

A fundamental requirement to performing STM is understanding how to calculate the tunneling current. The real tunneling situation is pretty complicated due to different varieties of samples and tips, but we only think about the simplest one: both tip and sample are metals, separated by tiny vacuum. So the whole problem is simplified to a particle attempting to travel between a potential barriers. In 1961, Bardeen proposed the time-dependent perturbation theory that was used most widely [102].

There are three presumptions in Bardeen's treatment: there is overlap in the density of states between the tip and the sample because of the super small gap; this kind of the weak overlap does not influence each density of states; wave functions exponentially drop to zero in the gap area.

Under all the prerequisites, we can calculate the tunneling current between the tip and the sample. We apply the positive bias V to the sample, then the Fermi level of the sample will be dropped the amount of eV compared to the tip electrons, so electrons will prefer to tunnel from the filled states of tip to the empty states of sample. The tunneling current passes through the barrier with energy, E, relative to the Fermi level of the sample as described by Eq. 2.1:

$$I_{t\to s} = -2e \cdot {}^{2\pi}/_{\hbar} \cdot |M_{ts}|^2 \cdot \rho_t(E) f(E) \cdot (\rho_s(E+eV)[1-f(E+eV)]) \quad 2.1$$

In this equation, the factor 2 stands for the spin up and spin down states, -e represents the classical negative electron charge, ${}^{2\pi}/_{\hbar}$ is the factor from the time-dependent perturbation theory, $|M_{ts}|$ is the tunneling matrix influenced by the separation distance between the tip and the sample, $\rho_t(E)$, $\rho_s(E)$ are the density of states for the tip and sample, respectively, and $f(E) = 1/(1+e^{E/k_BT})$ is the famous Fermi distribution [103].

Eq. 2.1 is the dominant tunneling current between the tip and the sample, but there are still electrons tunneling from the sample to the tip:

$$I_{s\to t} = -{}^{4e\pi}/_{\hbar} \cdot |M_{st}|^2 \cdot \rho_s(E+eV) f(E+eV) \cdot (\rho_t(E)[1-f(E)]). \quad 2.2$$

The two tunneling currents are in opposite directions, so the total current should be the integral over the all energies E after the subtraction of Eq. 2.2 from Eq. 2.1. Then we get the total tunneling current from the tip to the sample:

$$I_{total} = -{}^{4e\pi}/_{\hbar} \cdot \int_{-E_{F(sample)}}^{\infty} |M|^2 \cdot \rho_t(E) \cdot \rho_s(E+eV) \cdot \{f(E)[1-f(E+eV)] - [1-f(E)]f(E+eV)\} dE. \quad 2.3$$

We can simplify Eq. 2.3 according to properties of Fermi distribution to:

$$I_{total} \approx -{}^{4e\pi}/_{\hbar} \cdot \int_{-eV}^{0} |M|^2 \cdot \rho_t(E) \cdot \rho_s(E+eV) \cdot dE. \quad 2.4$$

For the simplest situation, the vacuum barrier is a square barrier with a smaller bias compared to the sum of the work function of both the tip and sample, the tunneling matrix $|M|$ can be written as Eq. 2.5 under the WKB approximation:

$$|M|^2 = e^{-2s\sqrt{\frac{2m}{\hbar}\left(\frac{\phi_s+\phi_t}{2}\right)}}. \quad 2.5$$

Where ϕ_s and ϕ_t represent the work functions of the sample and the tip, respectively [103, 104]. Finally, we get the total tunneling current:

$$I_{total} = -{}^{4e\pi}/_{\hbar} \cdot e^{-2s\sqrt{\frac{2m}{\hbar}\left(\frac{\phi_s+\phi_t}{2}\right)}} \int_{-eV}^{0} \rho_t(E) \cdot \rho_s(E+eV) \cdot dE. \quad 2.6$$

Tersoff, J and D.R. Hamann proposed a s-wave-model to simplify the density of states of the tip to a constant, so, we can simplify the tunneling current [106]:

$$I_{total} = -{}^{4e\pi}/_{\hbar} \cdot e^{-2s\sqrt{\frac{2m}{\hbar}\left(\frac{\phi_s+\phi_t}{2}\right)}} \cdot \rho_t(0) \int_{-eV}^{0} \rho_s(E+eV) \cdot dE. \quad 2.7$$

Therefore, we can differentiate the Eq. 2.7 to get the straightforward relationship:

$$\frac{dI}{dV} \propto \rho_s(E+eV). \quad 2.8$$

Thus, the simplified dynamic tunneling current conductance is just proportional to the local density states of the surface.

2.2 Omicron STM Designs

2.2.1 STM Overview

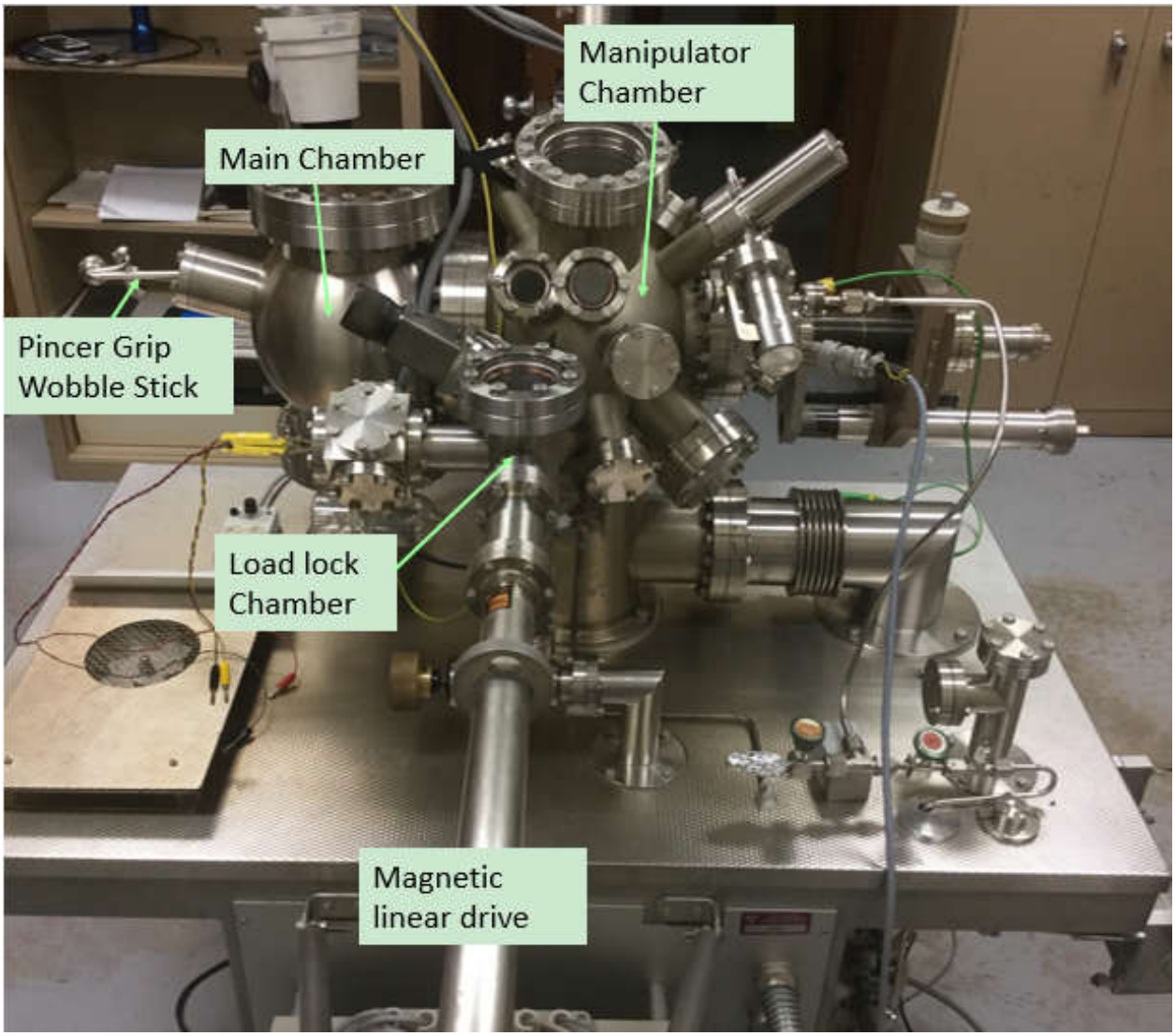

Fig. 2.2. The RT-STM system.

Our main machine is the first generation of STM, from Omicron Company, as shown in Fig. 2.2. The load lock chamber is an important transfer station through which we can transfer our samples and tips in or out of the main chamber easily without destroying the high vacuum in the main chamber. The magnetic linear drive is responsible for all transferring processes. Manipulator chamber is the place where we can prepare the sample for our main chamber, for example, annealing or sputter annealing the sample, depositing molecules on the sample. Main chamber is

the main part in a STM used to scan samples, including a tip, a scanner, sample stage and coarse runner, which are suspended by springs, shown in Fig. 2.3

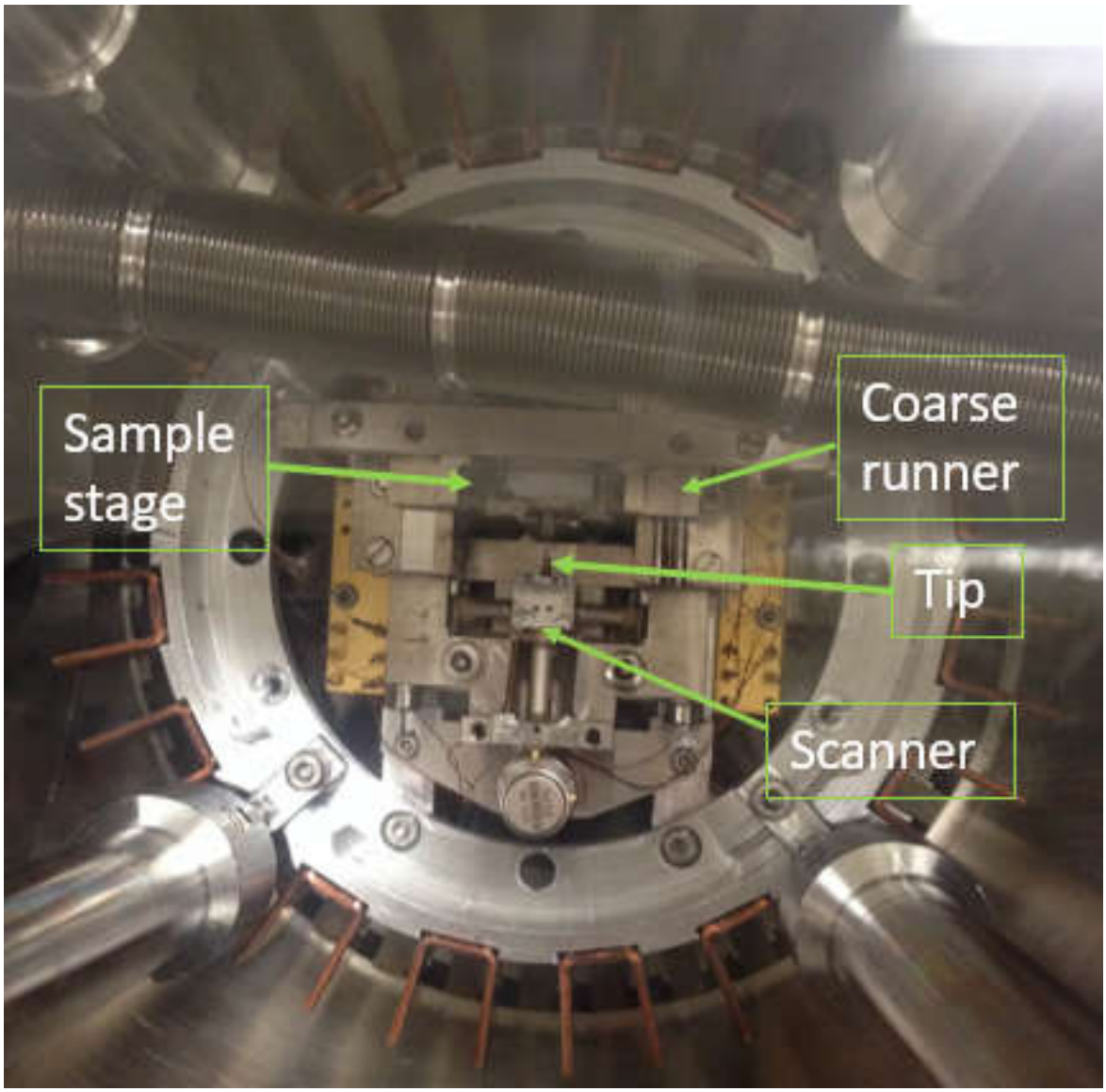

Fig. 2.3. Photos showing the main part of the scanning head in RT-STM.

Due to the high-resolution requirement in the angstrom level, the shape of the tip end is important. We use the hand-cut platinum-iridium tip as our backup tip in our chamber, and the most common tip we used is the chemically etched tungsten (W) tip. We use the 2-step methods to fabricate and polish a W wire with a diameter of 0.01 inch in the KOH solution and bubble in order to get a good tip with one single atom at the top end of cone base. In order to check whether

a tip is good or not, we need to check its overall shape with optical microscope first, then transfer to the main chamber with Au (111) as the standard sample to test it. The basic requirement for a good tip is that it can resolve the steps clearly in Au surface. A perfect tip can even resolve the herringbone structure on stepped Au at room temperature.

In order to get the tunneling current, the distance between the tip and a sample is a few angstroms only, so we need the help of a device to move a tip precisely in angstrom scale. This part is the scanner. There are five requirements for a good scanner: high resolution in both lateral (1 Å) and vertical (0.01 Å) direction; enough range – the tip should be moved to scan every spot in a sample; good orthogonality – the dependence of three orthogonal directions; linearity – the movement should be controlled precisely by the applied voltage; mechanical rigidity – vibration isolation and feedback system need a rigid scanner in order to tone the high resonant frequency. Commercial piezoelectric ceramic (PZT) satisfying all of these requirements is chosen to make the scanners in most STMs.

2.2.2 Electronics of Scanning

From the Eq. 2.6, we can clearly notice the total tunneling current is related to the bias V, the relative distance between the tip and the sample surface, s. In our real equipment, we utilize these two parameters to get the topography of the surface.

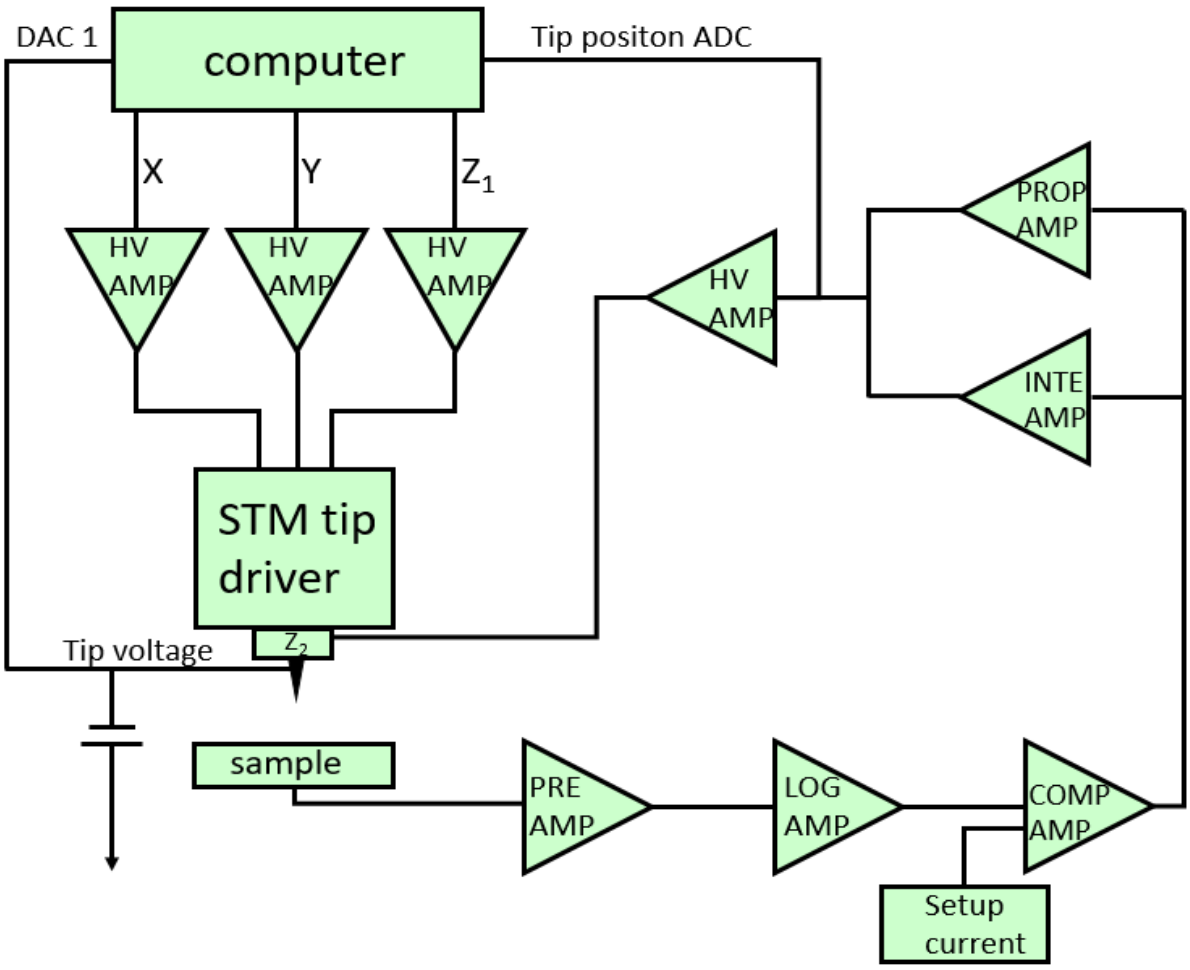

Fig. 2.4. Schematic drawing for the block feedback circuit of a classical STM.

The block feedback circuit of a classical STM is illustrated in Fig. 2.4. The electronic part in the STM is designed with great attention paid towards avoiding any electronic noises or instabilities from the feedback system. Computer-controlled digital-to-analog converter (DAC) can provide the bias voltage to the tip or sample, and the range is usually from 1 mV to 4 V. A preamplifier can measure the tunneling current between the tip and sample with a gain of 10^6-10^9 V/A, when the tip and sample are in the range of a few angstroms. Because the tunneling current is exponentially related to the distance between the tip and sample, the logarithmic amplifier can linearize the tunneling current to improve the dynamic range. This logarithmic amplifier is not that necessary when the surface is pretty flat, but it is significantly essential for a rough surface. There is a setup current (10 pA to 10 nA) to compare with the measured current, and the relative error signal will be sent to the feedback loop, usually includes a proportional amplifier and an integrator

amplifier. This feedback signal will finally go to a high-voltage amplifier in order to adjust the z position of the tip through the z piezoelectric drive. Computer-controlled DACs with a subsequent high-voltage amplifiers can control scanning the X-Y plane [107].

2.2.3 Pumping System

STM is kept in UHV conditions, and the base pressure is in the range of 10^{-10} Torr. There are two main purposes to maintain an STM in such high vacuum. First of all, a tip and samples can keep clean for longer time periods (up to one month in UHV), which is crucial for getting topographic images with better quality. The scanning distance between the tip and the sample is only a few angstroms, so a cleaner sample has a lower chance of contaminating the tip, in return. Secondly, the mechanism of STM relies on the tunneling current going through vacuum between the tip and the sample, the existence of air will make the tunneling between tip and sample more complicated, leading to inaccuracies in the measured topography [108].

In our pumping system, the mechanical backing pump, as the first backing pump, can pump the pressure low enough before turning on the turbo molecular pump. Typically, this backing pressure by mechanical backing pump is around 0.1 mbar and usually can even go down to 0.01 mbar. It is very hard to pump the backing pressure below 10^{-3} mbar where the mean free path of air is around 70 mm because of the increased flow resistance of the vacuum pipe between the turbo molecular pump and the mechanical baking pump. Once the pressure is pumped low enough so that the turbo molecular pump is ready to be turned on, the whole pressure then can be pumped down to intermediate high vacuum ($\sim 10^{-4}$ mbar), and even down to the UHV conditions ($\sim 10^{-10}$ mbar) after pumping for enough long time. When the vacuum is high enough, the ion pump can be turned on to help keep the UHV pressure. The mechanism of ion pump is ionizing gas within the vessel of STM using a high electrical potential, typically 3 kV–7 kV, which can accelerate the ionized molecules into the solid electrode forming a residue. Ideally, 10^{-11} mbar UHV pressure condition can be reached when all the pumps work well without any leaking.

2.2.4 Vibration Isolation

High resolution is essential to STM measurement and therefore careful attention must be paid to eliminating vibrations in order to get clear data. The source of the vibration noise can be any vibrations in the building, such as walking along the lobby, moving chairs in the classroom, noises from the repairmen of the building, or sometimes even loud speaking. The vertical resolution of the STM is around 1 pm, which means the stability of the distance between the tip and the sample should be in the level of 0.1 pm. But the normal floor vibration amplitude is around 1 μm, six orders larger than the stable measurement requirement of STM, so a series of vibration isolation design should be set for a STM [107].

STM instruments commonly make use of the combination of a set of passive damping systems to isolate the environmental vibration. Viscoelastic materials (usually Viton and rubber), and metal springs are the most commonly used methods for reducing vibrations. Depending totally on the stretched length of the spring, metal springs have a rather low resonance frequency (1~6 Hz). Hence, in the real STM instrument, all these passive damping systems are combined together. An eddy-current damping system composed of copper elements and permanent magnets is combined in the whole damping system sometimes [107]. In our lab STM, commercial pneumatic feet are a part of the vibration isolation system.

Besides the external damping combination system, a rigid STM makes good use of the inherent damping mechanism to get better vibration isolation. The important relative part should be the construction of the tunnel unit, the requirement of which is stiff and tiny. By combining the rigid internal design and the external passive damping system, the high resolution requirement of STM can be achieved.

In order to get the best vibration isolation, the STM has to be built in the basement. The floor of the basement room should be covered by acoustic shielding. With all of the above damping systems work together, the resolution of STM can go down to 0.1 pm.

2.3 Other Experimental Equipment

2.3.1 Thermal Evaporator

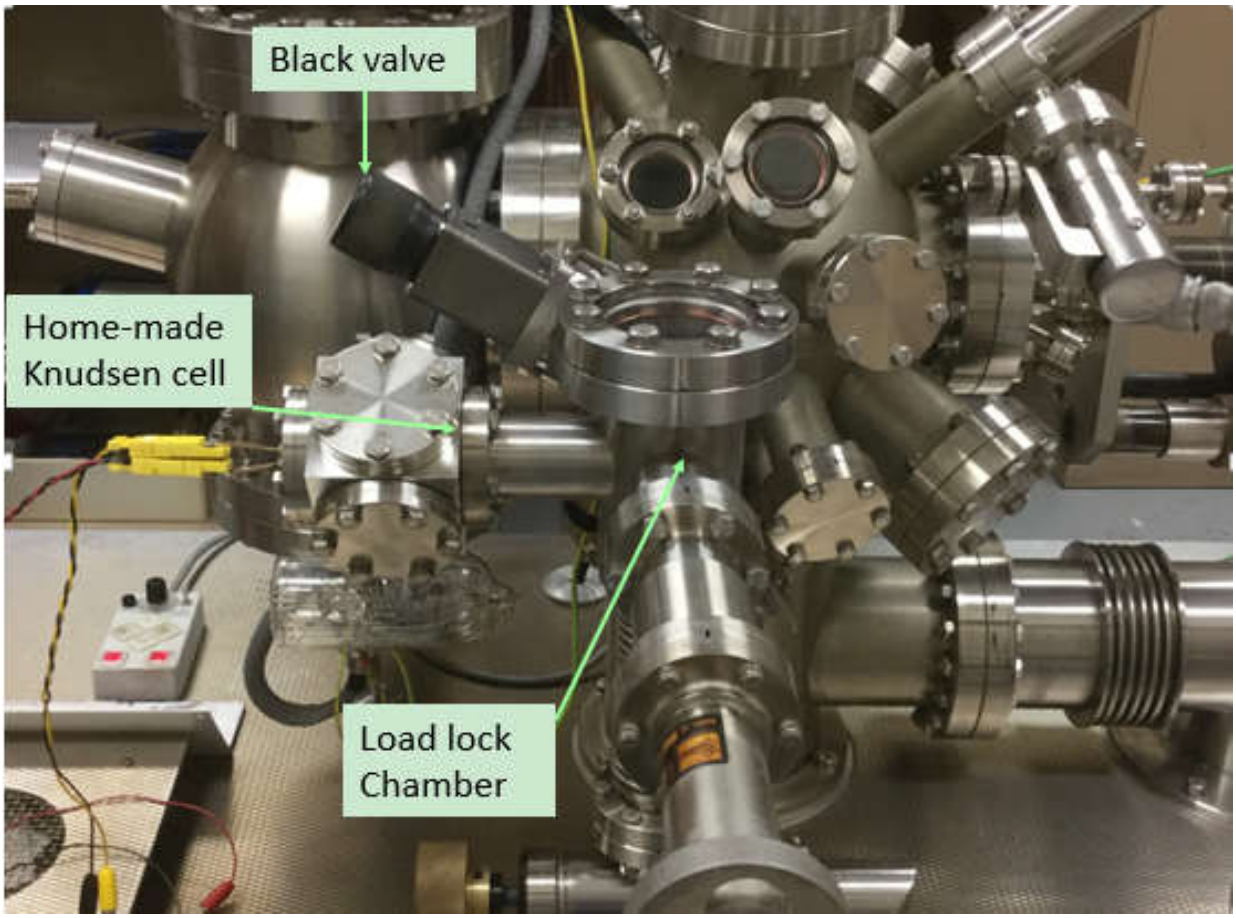

Fig. 2.5. Thermal deposition sub-system.

In our designs, different molecules need to be deposited onto the substrate surface such that the aimed hybrid structures can be obtained. The standard UHV STM equipment does not have a built-in setup for molecule deposition which will help in avoiding contaminations from outside sources. We mount a home-made Knudsen cell evaporator in the load lock chamber separated from the main chamber by a valve (Fig. 2.5). Normally the black valve is closed in order to keep the UHV in the main STM chamber. The Knudsen cell evaporator is mounted in the load lock chamber and can be baked separately, which is also helpful for changing the molecules or refilling the evaporator. The separated evaporator can also shorten the pumping time before the annealing process, otherwise, the whole STM needs to be pumped and baked for one single deposition.

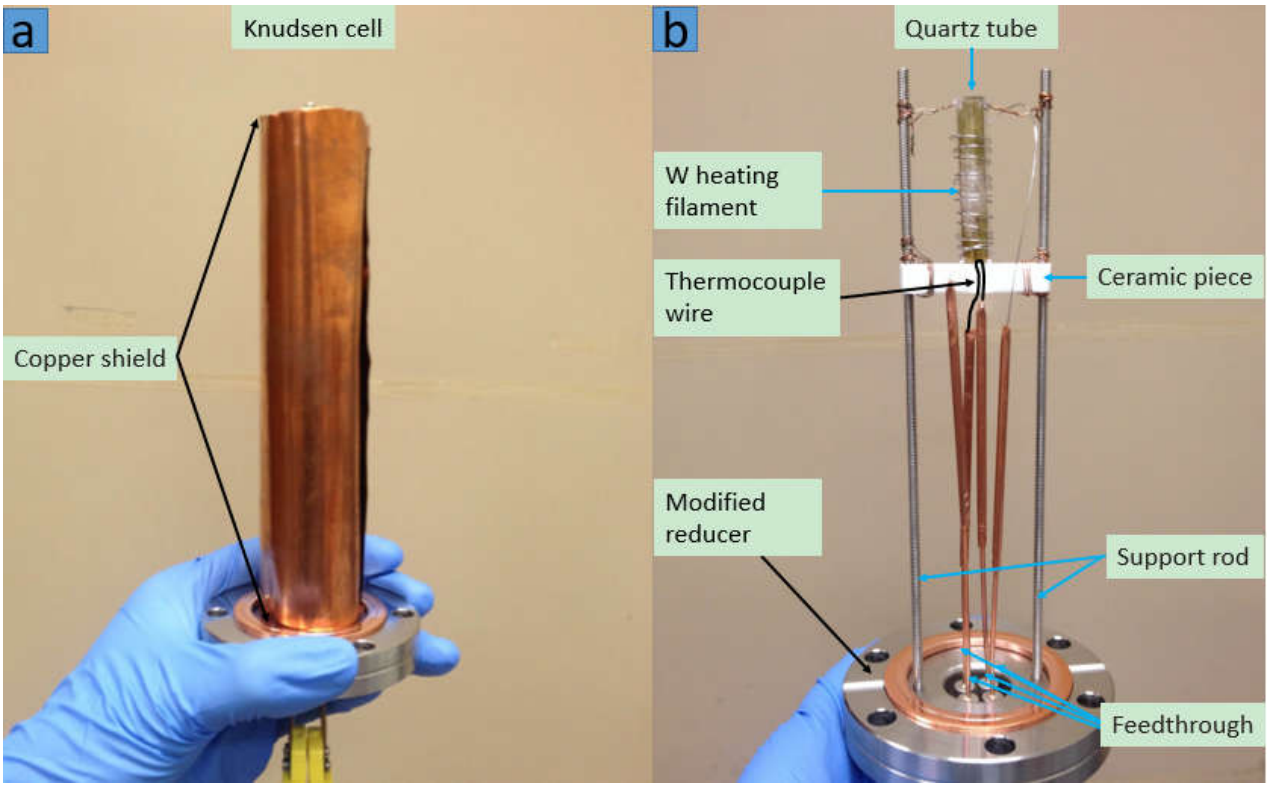

Fig. 2.6. The photos of the home-made Knudsen cell. (a) The home-made Knudsen cell with the copper shell. (b) The detailed structure of the home-made Knudsen cell.

Fig. 2.6a shows the whole evaporator mounted in the load lock chamber. The copper shield can prevent the molecules from contaminating the load lock chamber. This Knudsen cell evaporator mainly consists of a quartz tube, W heating filament, thermocouple wire and feedthrough illustrated in Fig. 2.6b. The quartz tube is used to accommodate the molecules; the spiral W wire will heat the molecules in the quartz tube through applied current; the thermocouple wire is used to measure the temperature of the molecules; the white ceramic piece is for holding the quartz tube. The heated molecules will be sublimated out when the temperature is higher than its melting point, and the amount of the sublimated molecules is determined by the temperature and the deposition time. A small amount of the sublimated molecules will be in a gaseous phase, so we usually check the change of the pressure in the load lock carefully in order to control the amount of molecules deposited onto the substrate. The substrate is always kept in the main chamber before the final deposition in order to keep fresh. After a long time pumping, we can get the monolayer or sub-monolayer thin film in a pretty low pressure condition.

2.3.2 Atomic Force Microscopy (AFM)

AFM is one kind of the scanning probe microscopies, with resolution on the order of nanometer, 1000 times higher than the optical microscope. Because it can probe the surface on both conductors and insulators, it is widely used across academic fields. Additionally, the scanning efficiency of the AFM overall is much higher than that of STM, because of the ease of changing a new AFM tip compared to the time consuming process of keeping a sharp tip during the STM measurement. Thus the AFM is a fast probe instrument in labs and companies, therefore it is a good supplement for STM in the lab experiment. We usually use AFM to take a quick look at our new samples first, especially when the overall morphology of the samples is not so clear. In this thesis, we used AFM to study Tollip on the endosome membrane via association with PI(3)P under the liquid tapping mode.

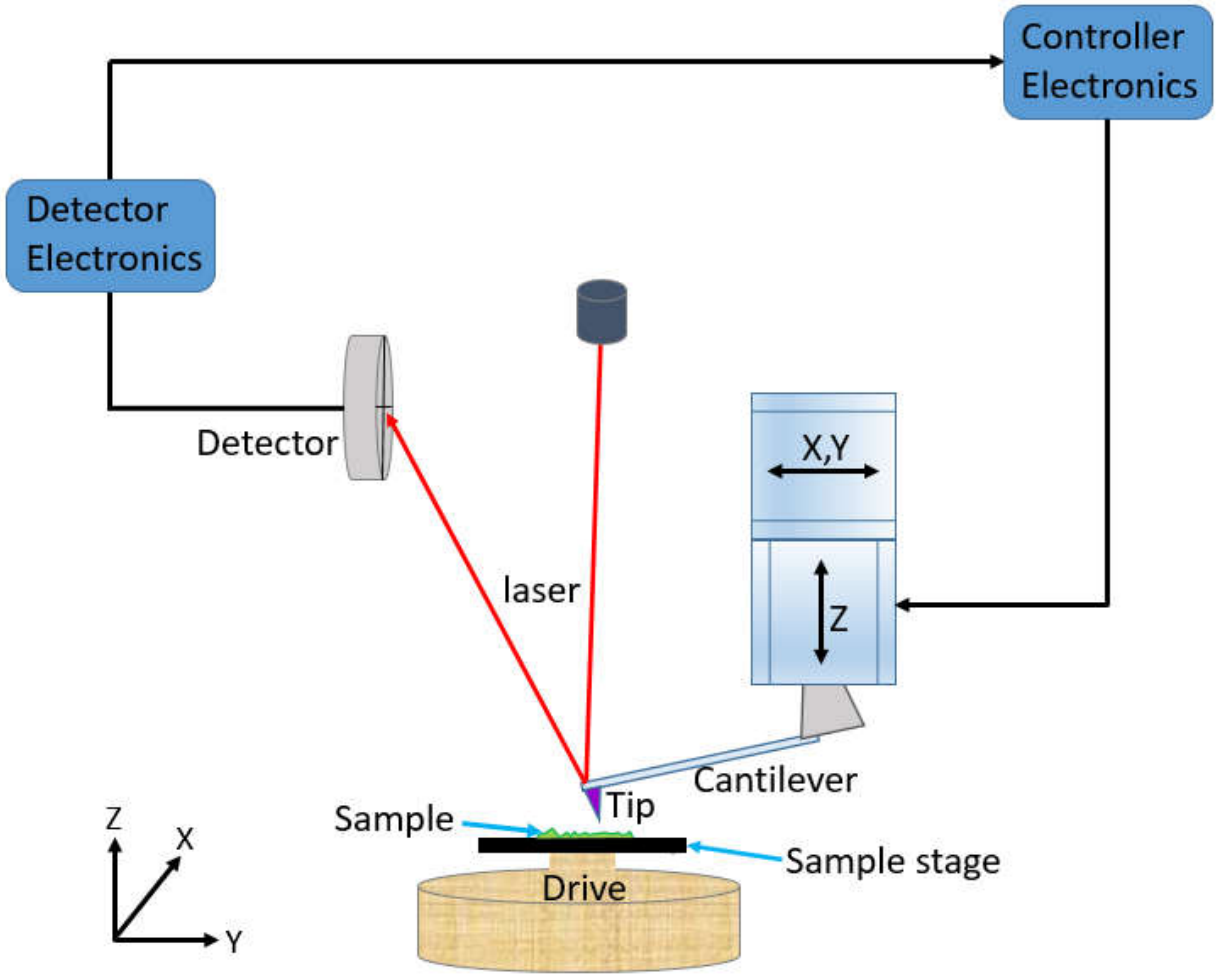

Fig. 2.7. Schematic drawing for the mechanism of imaging mode in AFM.

The mechanism of imaging mode in AFM is due to the atomic force between the tip end and the sample. The air mode is the most used one compared to the liquid mode in AFM. Both modes have the contact, tapping and noncontact modes in the measurement. We will take the contact mode in air as an example to explain how the AFM works to get an image. Just as shown in Fig. 2.7, an atomically sharp tip mounted at the end of the cantilever is automatically approached to contact with the sample. Then the height variations of the sample surface will change the deflection of the cantilever, the deflection will then be detected by the laser detector, and the signal from the detector will be as an input to the controller electronics. This feedback loop will keep the atomic force between the tip end and the sample a constant value through Z piezo. The voltage information of the Z piezo will be recorded as the Z information of the sample. When the sample is raster scanned over the aimed area of the sample along the X-Y grid, we can get the AFM image with X-Y-Z information plotted in a pseudocolor style.

Chapter 3. Quasi 1D C_{60} Structures on Graphene

3.1 Introduction

Graphene, a single atom thick layer of sp^2 hybridized carbon atoms, is a unique 2D material that exhibits fascinating physical properties and has numerous potential applications [15, 16]. To understand the physical and chemical properties of graphene and explore its potential applications, significant research efforts have recently been devoted to investigate the adsorption and desorption of various molecules on graphene, and to further optimize and control the molecule/graphene hybrid structures. For these studies, graphene grown by CVD method on metals is emerging as an ideal platform, which is also one of the most promising candidates for practical applications of graphene that require scalable production of graphene [17, 18].

Buckminsterfullerene, C_{60}, is a closed-cage structure composed of 60 carbon atoms linked by single and double bonds to form a hollow sphere. Due to its many exciting chemical and physical properties, numerous applications have been demonstrated in single-electron transistors, superconductivity, and photovoltaics [109, 110]. Due to its single element composition and highly symmetrical shape, C_{60} often serves as a model system for understanding molecule-surface interactions. C_{60} on epitaxial graphene, a system exclusively formed of elemental carbon, provides an ideal model system to study interactions at the molecular level, electromigration, molecular electronics and spintronics. On most metal or graphite surfaces, C_{60} molecules self-assemble into isotropic thermodynamically favorable hexagonal close-packed monolayers [111-114].

A particularly interesting arrangement of C_{60} is the quasi-1D structure. Highly ordered 1D molecular configurations are excellent model systems and prototypes of 1D quantum confinement of electronic states, and thus have potential importance in electronic nanodevices, spintronics and solid-state quantum computation [115-118]. However, quasi-1D C_{60} nanostructures have been rarely realized experimentally due to their highly anisotropic configuration. A few previously reported experimental results include C_{60} peapods by embedding C_{60} molecules in carbon nanotubes, 1D C_{60} structures aligned along step edges on vicinal surfaces of metal single crystals, and C_{60} chains on self-assembled molecular layers [119-122]. For CVD graphene, periodically linear rippled structures have been previously observed on various growth substrates [123, 124]. Here we experimentally realize quasi-1D C_{60} nanostructures on rippled graphene by utilizing the

linear periodic potential in graphene as a template. Through carefully controlling the subtle balance between the weak periodic potential and the surface mobility of C_{60}, C_{60} molecules on rippled graphene are arranged into a novel 1D C_{60} chain structure with widths ranging from two to three molecules wide. At a higher annealing temperature, the 1D chain structure transitions to a more compact hexagonal close packed quasi-1D stripe structure. To the best of our knowledge, this is the first experimental realization of 1D C_{60} structures on graphene. Our experimental results may pave a way for fabricating new C_{60}/graphene hybrid structures for future applications in electronics, spintronics (e.g. endohedral fullerenes with magnetic spins can be aligned in 1D configurations), and quantum information.

3.2 Thermal Evaporation

C_{60} molecules were deposited onto graphene grown by the CVD method on Cu foil at the background pressure below 2.0×10^{-8} mbar. All experiments were carried out in an UHV scanning tunneling microscope system (Omicron LT-STM). Before C_{60} deposition, the graphene grown by the CVD method on Cu foil was annealed for 12 hours at 673 K in a preparation chamber with a base pressure of low 10^{-10} mbar. C_{60} powder (MER Corporation, 99.5% purity) was loaded into the homemade Knudsen cell mounted on the load lock of the LT-STM system. The C_{60} source was degassed at a pressure of low 10^{-8} mbar before deposition. C_{60} molecules were then sublimated at a deposition rate of ~ 0.9 monolayer per minute (ML/min) with the background pressure below 2.0×10^{-8} mbar. During the deposition process, the substrate was kept at room temperature. The sample was then subsequently annealed at 423 K, 487 K, and 578 K respectively in the preparation chamber of the STM system with the base pressure at low 10^{-10} mbar. All the STM measurements were performed at room temperature in the STM characterization chamber with a base pressure of about 3.0×10^{-11} mbar.

3.3 Results

3.3.1 Chain Structures

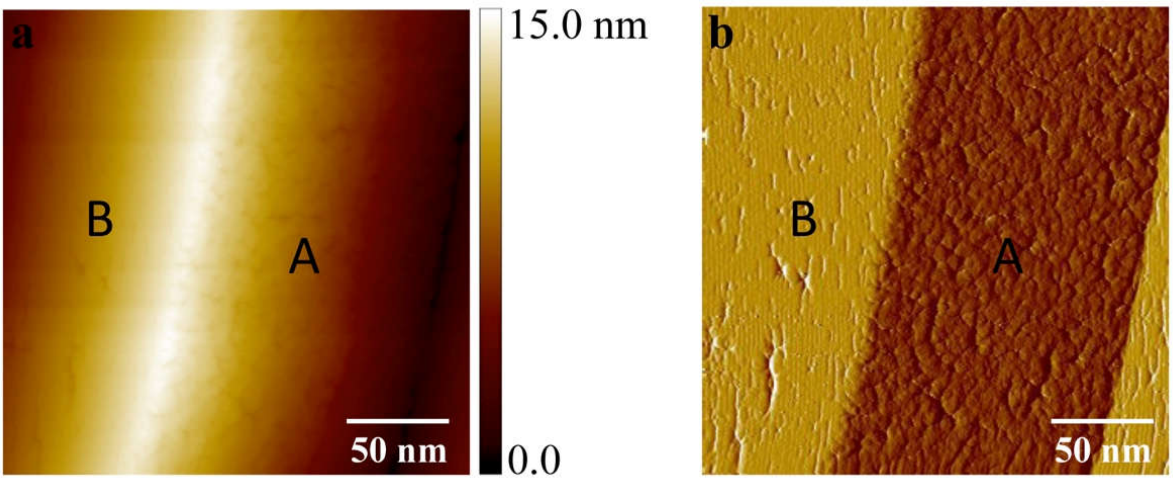

Fig. 3.1. STM images of type A and type B facets with C_{60} molecules covered after 423 K annealing. (a) The topographic and (b) corresponding current images of type A and type B facets with C_{60} after 423 K annealing (V_s = 2.00 V, I = 0.30 nA) [1].

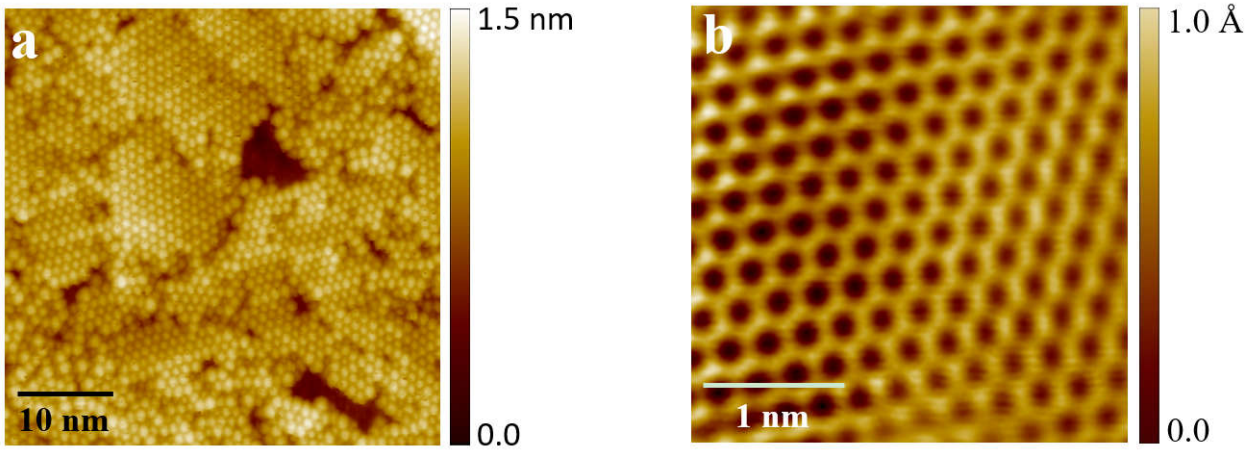

Fig. 3.2. (a) The high-resolution STM image of C_{60} islands on type A facets (V_s = 1.20 V, I = 0.50 nA). (b) Atomic resolution STM image of flat graphene on an empty area adjacent to a close-packed C_{60} island (V_s = 0.10 V, I = 3.50 nA) [1].

C_{60} molecules were deposited onto graphene grown by the CVD method on Cu foil at the background pressure below 2.0×10^{-8} mbar. After post-deposition annealing at 423 K, we observed

small atomically flat facets with typical sizes ranging from 50 nm to 200 nm. These facets can be classified into two predominant types based on the distinguishable surface characteristics, labeled as type A and type B, shown in Fig. 3.1. On type A facets, C_{60} molecules form hexagonal close packed monolayers and islands shown in Fig. 3.2a.

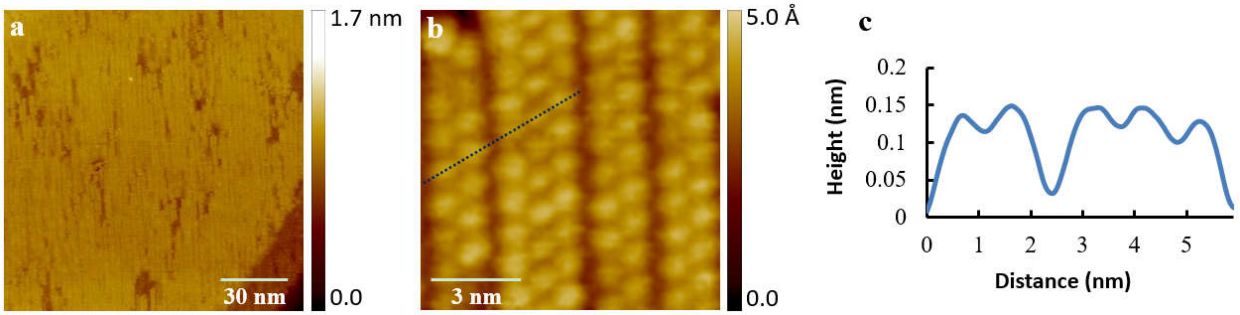

Fig. 3.3. 1D bimolecular and trimolecular C_{60} chains after annealing at 423 K. (a) Large scale STM image of C_{60} on graphene showing well ordered 1D structure on Cu facets (V_s = 1.90 V, I = 0.40 nA). (b) High-resolution image of bimolecular and trimolecular C_{60} chains. Within the chains, the C_{60}-C_{60} intermolecular spacing is ~ 1.0 nm, and the inter-chain distance, defined as the distance between the centers of adjacent C_{60} rows belonging to neighboring chains, is 1.23 nm (V_s = 1.95 V, I = 0.50 nA). (c) A line profile along the close packed orientation as marked with the dashed blue line in (b) [1].

On type B facets we observed a characteristic quasi-1D feature of C_{60} molecules as shown in the large-area overview STM image in Fig. 3.3. A closer inspection of the high-resolution STM images reveals the details of this 1D structure featured in Fig. 3.3b, in which each bright protrusion represents a C_{60} molecule. Typically, the 1D chains consist of two or three C_{60} rows, referred to as bimolecular and trimolecular C_{60} chains, respectively. Within a chain, the C_{60}-C_{60} intermolecular spacing is 1.00 ± 0.01 nm, indicating that C_{60} molecules arrange in a close packed manner. From the line profile shown in Fig. 3.3c that corresponds to the dashed line marked in Fig. 3.3b, the isolation between adjacent C_{60} chains can be clearly seen from the gap between the second and the third peaks. Here, the second and the third peaks represent the C_{60} molecules belonging to neighboring chains. The measured average inter-chain distance, defined as the distance between the centers of adjacent C_{60} rows belonging to neighboring chains, is 1.23 ± 0.02 nm, as schematically shown in Fig. 3.6a and Fig. 3.6c. In our measurements, we observed that the chains

consist exclusively of two or three C_{60} rows. From statistical analysis, the bimolecular chains are shown to be more numerous, with a ratio of number of bimolecular to trimolecular chains of about 2.0. As observed in large-scale STM images, the chains are usually arranged in a 3-2-2 or 2-3-2 manner. In our measurements, we observed that the orientation of these C_{60} chains was exclusively along the same direction, nearly parallel to the bending axis. In the chain structure we also observed some junctions where a bimolecular segment transitions into a trimolecular segment, or vice versa.

3.3.2 Stripe Structures

In order to investigate the temperature evolution of the C_{60} nanostructures on graphene, we performed subsequent annealing at a higher temperature, 487 K, for 2 hours. After annealing at this temperature, the C_{60} chain structure disappeared and a new， more compact hexagonal close packed quasi-1D stripe structure emerged, as shown in Fig. 3.4a. The zoom in topographic STM image in Fig. 3.4b reveals hexagonal close packed quasi-1D stripes with widths of three and six C_{60} rows. A noticeable difference from the C_{60} chain structure is that these quasi-1D stripes are formed on staggered narrow terraces, which are between nearly straight and parallel step edges (Figs. 3.4b and 3.4d). In the stripe structure there is no spacing between neighboring stripes. In contrast, the quasi-1D stripe structure appears more crowded than the close packed structure. The lateral inter-row distance between the two rows adjacent to the step edges, on the upper and lower terraces respectively, is 0.75 ± 0.01 nm, as schematically shown in the ball models in Figs. 3.6b and 3.6d. This high-density arrangement seems to accommodate the underlying narrow terraces that formed after annealing at 487 K. On the narrow terraces, C_{60} molecules are arranged in a close packed manner with a characteristic C_{60}-C_{60} intermolecular spacing of 1.00 ± 0.02 nm. We also noticed that the C_{60} row near the step edge on the upper terrace is with a measured height higher than the other rows on the same terrace as shown in Figs. 3.4b and 3.4d. Different from the dominance of C_{60} chains with widths of two or three C_{60} rows, the width of the stripes varies from three to eight rows of C_{60}. The most common stripes have a width of 6 C_{60} rows. Fig. 3.4c is the normalized distribution of the C_{60} stripe width in terms of the number of C_{60} rows.

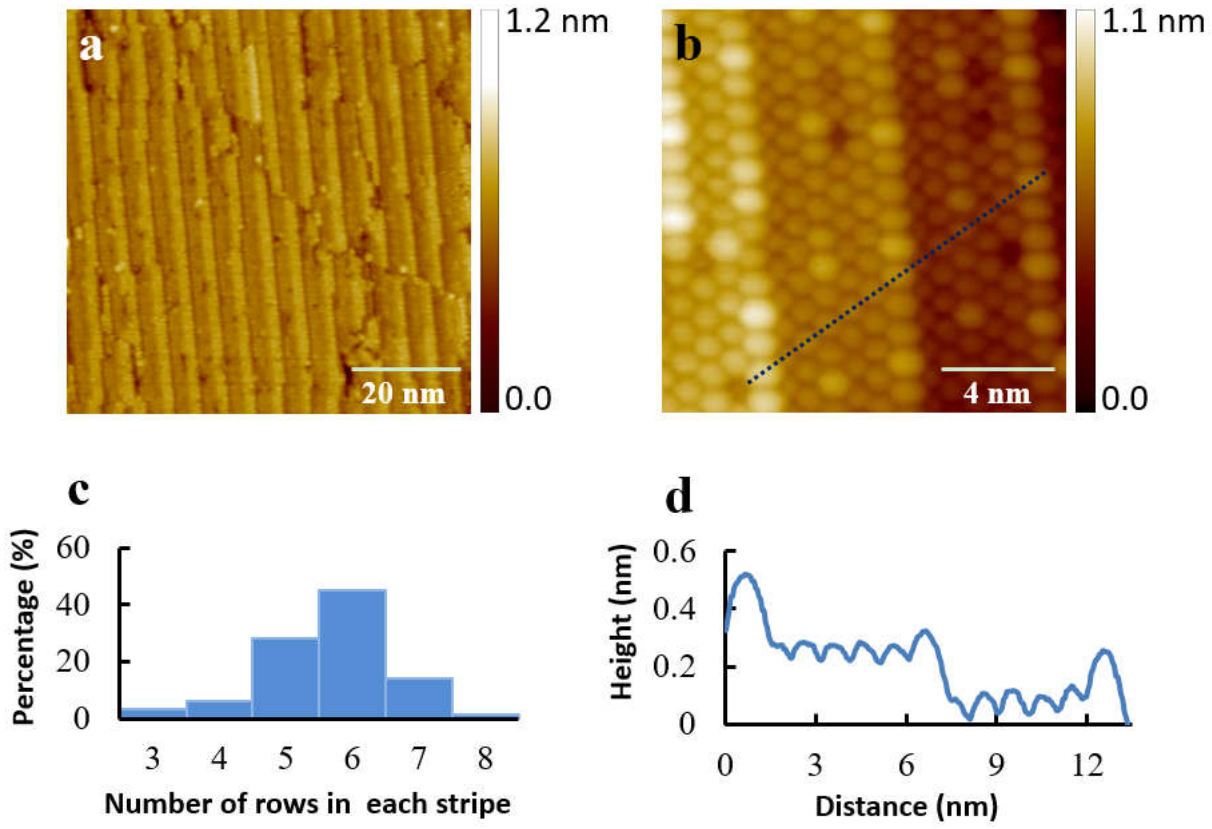

Fig. 3.4. Self-assembled quasi-hexagonal close packed 1D C_{60} stripe structure on rippled graphene after annealing at 487 K. (a) Large-scale STM image of C_{60} on graphene showing quasi-hexagonal close packed 1D stripe structure (V_s = 2.20 V, I = 0.20 nA). (b) High-resolution image of the quasi-hexagonal close packed 1D stripes (V_s = 2.40 V, I = 0.20 nA). (c) Normalized distribution of C_{60} stripe widths in terms of the number of rows. (d) A line profile along the close packed orientation as marked with the dashed blue line in (b) [1].

The 6-row stripes are the most common stripe structure, with a probability of 45%, and 5-row stripes are the second most likely stripe structure. The 8-row and 3-row stripes are minority groups. The lateral periodicity of these typical 6-row stripes is 5.08 ± 0.02 nm, almost exactly the same as the lateral spacing of a bimolecular chain plus a neighboring trimolecular chain in the chain structure, which is also 5.08 ± 0.02 nm. The stripes are nearly parallel to each other and the orientation of the stripes is along the same orientation with the C_{60} chains. Similar to the chain structure, there are junction regions in these quasi-1D stripes. Another detail worth noticing is that the downhill direction of the stripes is determined by the boundaries of the facets. The protrusion

boundaries are the downhill side while the depression boundaries correspond to the uphill side shown in Figs. 3.5a and 3.5b.

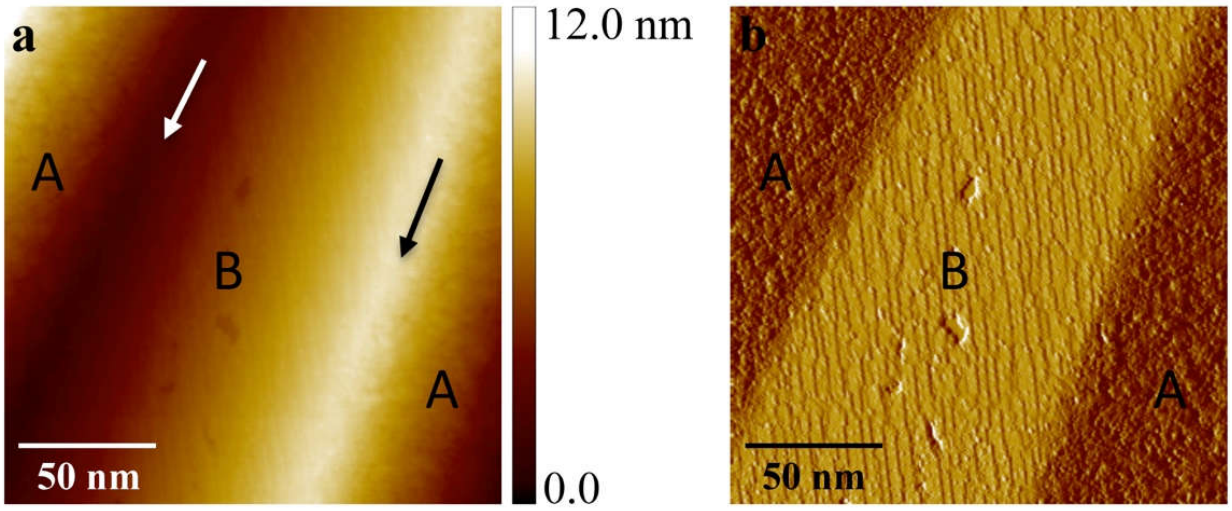

Fig. 3.5. STM images of type A and type B facets with C_{60} molecules covered after 487 K annealing. (a) The topographic and (b) corresponding current images of type A and type B facets with C_{60} after 487 K annealing (V_s = 1.50 V, I = 0.30 nA) [1].

Fig.3.5 (a) shows the large scale STM image with both well-ordered (type B) and less-ordered facets (type A). The left and right sides are type A facets with a type B facet in the middle. Here we can see the connecting lines between vicinal type A and type B facets, which appear as either a protrusion (marked by the black arrow) or a depression line (marked by the white arrow), reflecting the different angles between the vicinal facets. Fig.3.5 (b) is the corresponding current image, clearly showing the well-ordered C_{60} quasi-1D structures on type B facets and less-ordered C_{60} structures on type A facets.

3.3.3 Schematic Modes for Chain and Stripe Structures

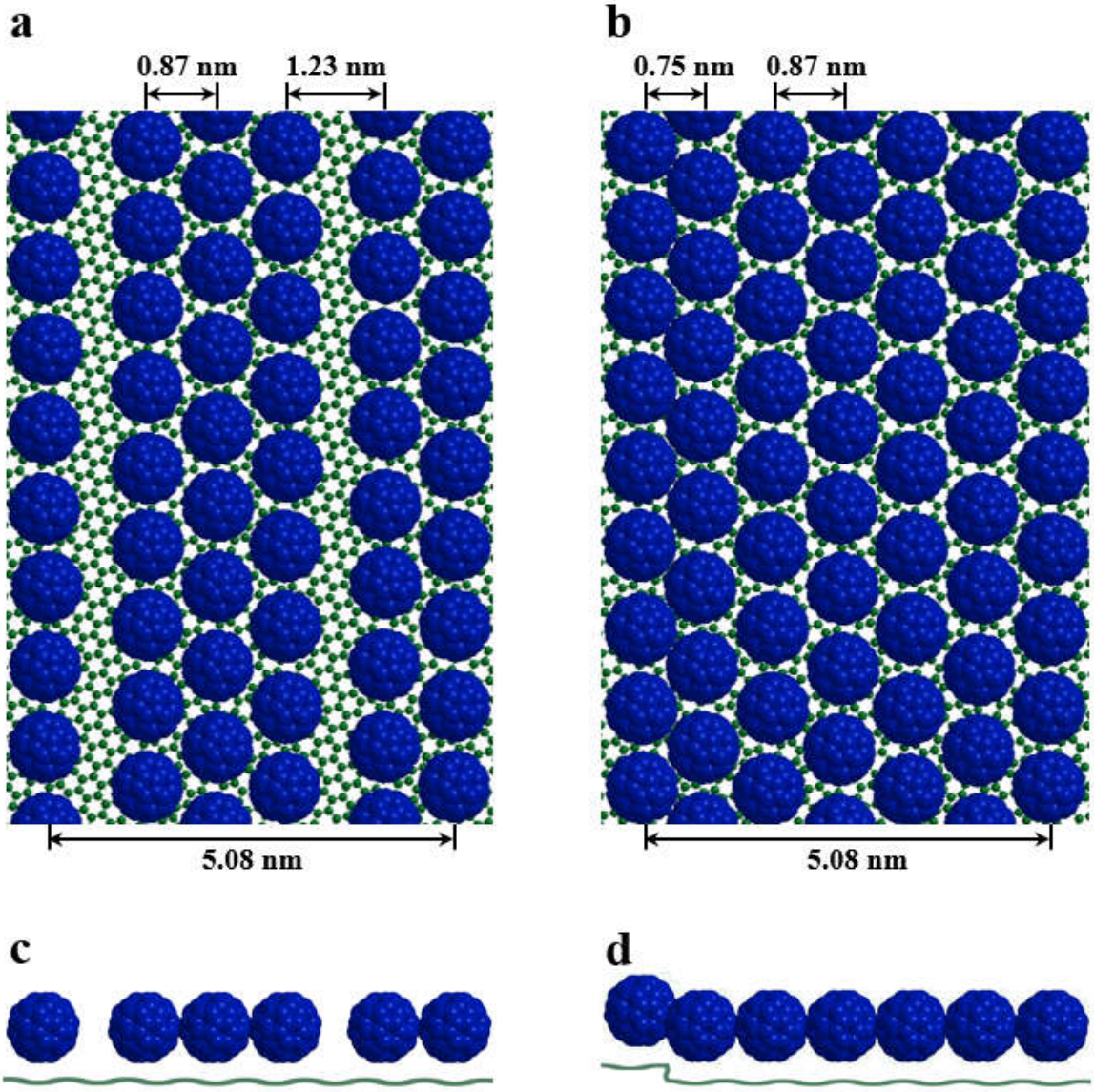

Fig. 3.6. Schematic models of the C_{60} chain and stripe structures showing the graphene layer (small dark green balls) and the C_{60} layer (dark blue space filling spheres) on top of the graphene layer. (a) and (c) Bimolecular and trimolecular C_{60} chains on graphene after annealing at 423 K. (b) and (d) C_{60} stripe structure with 6-row width after annealing at 487 K [1].

To compare the chain structure and the stripe structure more clearly and visually, we try to use a 3D model to explain it. Figs. 3.6a and 3.6c is the schematic model for the bimolecular and trimolecular C_{60} chains with dark blue spheres representing C_{60} molecules and green spheres

representing carbon atoms of underlying graphene. The single C_{60} row on the left side is the adjacent row in the next bimolecular or trimolecular chain. The width of a bimolecular cell (chain plus the interchain spacing) plus a trimolecular cell is 5.08 ± 0.02 nm. From these models, we can clearly see the large spacing (1.23 nm) between adjacent chains (Fig. 3.6a). In the stripe structures, the inter-row spacing between the C_{60} rows adjacent to step edges from both sides is 0.75 nm, narrower than the other C_{60} rows arrange in a hexagonal close packed manner (Figs. 3.6b and 3.6d).

3.3.4 Rippled Graphene on Cu(100)

To gain detailed insight into the growth mechanisms of the quasi-1D C_{60} chain and stripe structures, we used STM to characterize the underlying graphene of the empty areas adjacent to the C_{60} quasi-1D structures, and the bare graphene surface before C_{60} deposition and after C_{60} desorption. After annealing the sample up to 578 K, all C_{60} molecules were desorbed from the surface, and the surface was restored to bare graphene on Cu. The desorption temperature is close to the desorption temperature of C_{60} molecules on HOPG [125]. The similar deposition temperature indicates a similar activation energy, which is 1.69 eV for C_{60} on graphite based on the thermal desorption spectroscopy study [125]. Atomic-resolution images taken on small flat facets of the substrates, where the quasi-1D C_{60} chains and stripes are grown, show a well-defined linear periodic graphene rippled superstructure with an orientation close to the chain and stripe orientation.

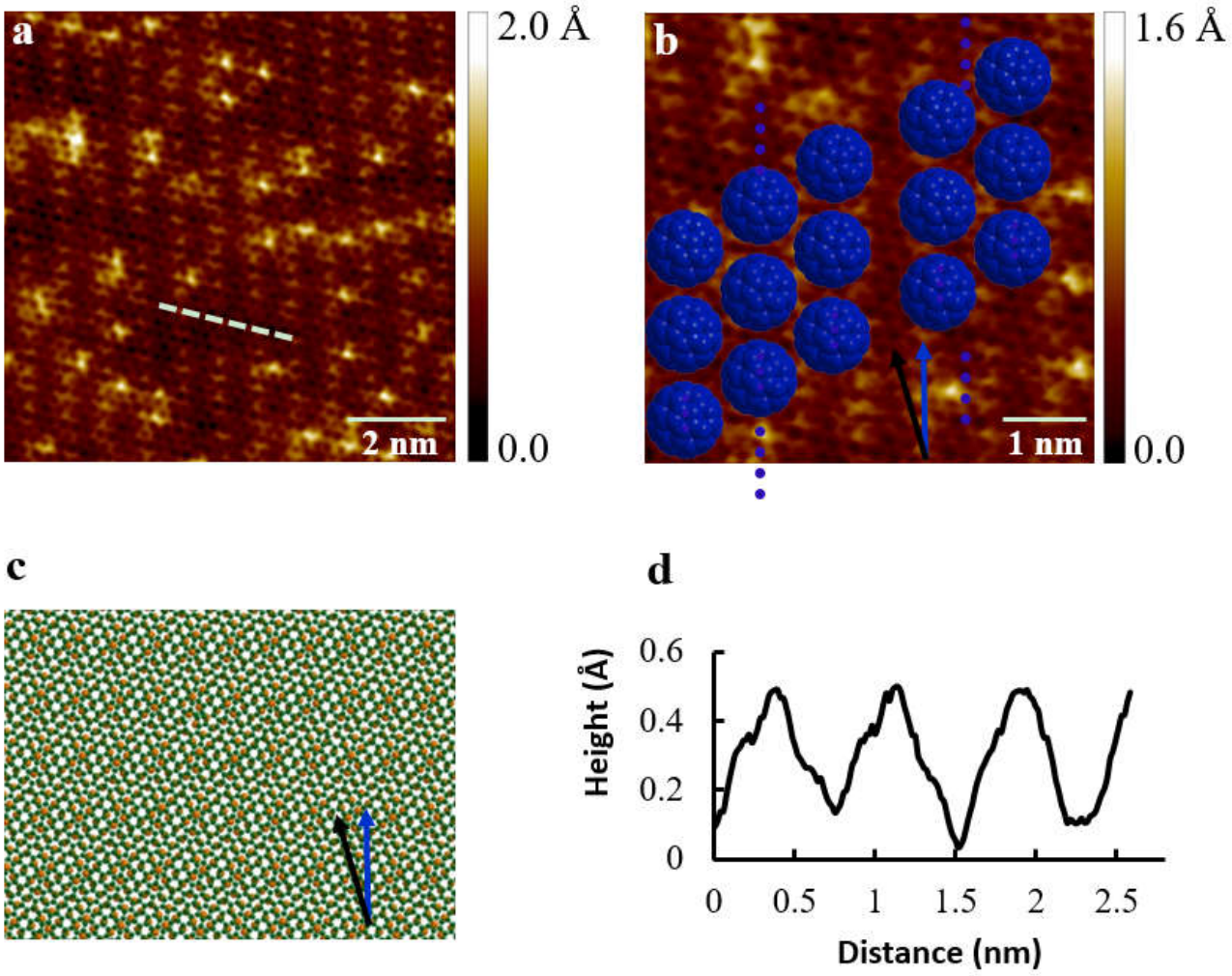

Fig. 3.7. STM topographic images of rippled graphene on Cu. (a) Large area STM topographic image of the rippled graphene showing well-defined linear periodic modulation with a 0.75 nm spatial modulation frequency (V_s = 0.80 V, I = 1.0 nA). (b) Magnified STM image of the rippled graphene with the ball model of C_{60} molecules in the arrangement of a bimolecular (right) and trimolecular (left) chain with the orientation along the ripples. The blue arrow indicates the orientation of the linear graphene ripples and the C_{60} chains, with a measured angle of 15.0° ± 0.5° relative to the zigzag direction of graphene, indicated by the black arrow. The periodicity of the linear modulation is 0.75 ± 0.01 nm (V_s = 0.80 V, I = 1.0 nA). (c) Suggested ball and stick model of the overlay of graphene on Cu(100). The zigzag direction of graphene is rotated by 13.0° with respect to the [01$\bar{1}$] direction of the Cu(100) underneath. The green balls represent carbon atoms of graphene, and the yellow balls represent Cu atoms of the underlying Cu surface. The blue arrow indicates the orientation of the linear moiré pattern, and the black arrow indicates the zigzag

direction of graphene. (d) Line profile along the zigzag orientation of graphene (marked as a dashed light green line in (a)) showing the periodic modulation [1].

Fig. 3.7a shows the typical linear periodic modulation of graphene with the periodicity of 0.75 ± 0.01 nm and with the same orientation of the observed C_{60} chains and stripes, as indicated by the blue arrow in Fig. 3.7b. The linear periodic structure as shown in Figs. 3.7a and 3.7b is attributed to the case where the underlying Cu facet is Cu(100). To confirm that, we checked two characteristic surface features. The step edges have a height of ~ 0.18 nm, which is the characteristic step height of monoatomic steps on Cu (100) surface [126, 127]. This kind of linear modulation of graphene due to the square lattice symmetry of the Cu(100) surface has been experimentally observed before [123, 124, 126]. The superposition of a graphene lattice on a Cu(100) surface with various angles produces linear rippled patterns with different periodicity [123, 124, 126]. At some certain angle, there will be maze-like reconstruction of graphene on Cu(100) [128]. However, superstructures of graphene on Cu(111) surface have characteristic six-fold symmetry [129-134], which can be distinguished easily from the linear periodic ripple structure in our experiments. In a few cases, linear superstructures of graphene on Cu(111) were also observed, but they usually have a much larger periodicity and disappear after annealing to 500 K [135]. The graphene ripples in our experiments survive after annealing to 693 K. From all these observations, it is reasonable to conclude that the Cu surface underneath rippled graphene is Cu(100). Based on the periodicity of the ripples, we are able to calculate the relative angle between graphene and the underlying Cu(100) surface. Fig. 3.7c is a suggested atomic model for the rippled graphene. The zigzag direction of graphene has an angle of 13.0° relative to the $[01\bar{1}]$ direction of the underlying Cu(100). The calculated periodicity is 0.80 nm and the orientation of ripples is with a relative angle of 15.2° to the zigzag direction of graphene, consistent with the measured angle of 15.0° ± 0.5°. The calculated periodicity is slightly larger than the measured periodicity of 0.75 nm. This difference may attribute to the out of plane distortion of graphene ripples, as shown in the line profile in Fig. 3.7d.

In both C_{60} chain and stripe structures (Figs. 3.3 and 3.4), we notice that a few C_{60} molecules appear higher than others, and the relative height shows bias dependence. The difference is

possibly due to the defect sites in the underlying graphene that appear as bright sites in the STM images of graphene (Fig. 3.7a).

3.4 Discussion

The orientation of the graphene ripples is fully consistent with that of the C_{60} chain structure. Based on the rippled graphene structure, it is possible for us to explain the formation of the chain structure from the point of view of mechanical stability [136]. The most common morphology for the C_{60} on flat graphene is the hexagonal close-packed structure due to the weak diffusion barrier on flat graphene and the much stronger C_{60}-C_{60} interaction [137, 138]. On rippled graphene, the linear periodic potential provides a template for C_{60} to arrange into more stable 1D configurations. The linear periodicity of rippled graphene, 0.75 ± 0.01 nm, is smaller than the typical inter-row distance of 0.87 nm in the C_{60} closed packed arrangement. C_{60} molecules randomly occupy the valley sites of the linear periodic potential at the initial stage of growth. It is possible for C_{60} molecules to settle down in the adjacent ripples at a less stable state because C_{60} molecules are forced to stay slightly off the valley sites. In this way, two or three adjacent linear graphene ripples are filled up. This is consistent with the observation that almost all C_{60} chains consist of two or three rows. Based on a geometrical and energetic argument, it is easy to see that chains with four or more rows are less likely to form. Compared with the formation of the bimolecular chains, the possibility to form trimolecular chains (both sides need a C_{60} molecule sitting down around the middle C_{60} molecule) is about half the probability of the formation of the bimolecular chains, which only need one side to be occupied with C_{60} molecules. From a Monte Carlo statistical approach, C_{60} molecules adsorbed on such a linear graphene sheet will be stabilized in one of the valleys, and if a second or a third molecular row packs closely to the stabilized molecular row, the chain structure consequently forms [136]. We expect that C_{60} molecules with less thermal energy can form monomolecular chains. That is one of the possible directions to further tune and control the formation of these 1D structures.

In order to understand how the bimolecular and trimolecular chains transform into the C_{60} stripe structure after annealing at 487 K, we will start by considering the diffusion of Cu atoms underneath graphene and the arrangement of C_{60} molecules on graphene. When annealing at a higher temperature of 487 K, C_{60} molecules have a higher probability to overcome the potential

energy difference between the hilltop and the valley sites of rippled graphene and rearrange into chains with larger width due to the higher thermal excitation. The junction structure in the bimolecular and trimolecular chains probably provides diffusion channels for C_{60} molecules to transfer between adjacent chains resulting in emergent chains with larger widths. Considering that the arrangement of bimolecular and trimolecular chains is usually 2-3-2 or 3-2-2 as described above, it is reasonable to assume that the emergent chains with width of five C_{60} rows are the configuration with highest probability to form, compared with chains of other widths. The distribution of chains widths and stripe widths may imply that at the annealing temperature of 487 K, the thermal excitation can only drive C_{60} molecules to cross over one or two energy barriers, but not more. When adjacent bimolecular and trimolecular chains merge into a 5-row chain, the interchain spacing between the merged 5-row chain to its neighboring chains can be generated from the initial inter-chain spacing in the chain configuration (1.23 nm), which is 1.59 nm. This spacing is slightly smaller than the interchain spacing of 1.73 nm required for a new C_{60} row to fill in the empty space. It has been previously reported that Cu atoms can easily diffuse underneath a graphene sheet even at room temperature [126]. These detailed observations suggest that copper atoms can diffuse along smooth step edges and kinked sites, and even dissociate from step edges, indicating a weak interaction between the graphene sheet and the underlying copper atoms [126]. Considering the boundaries of the facets (see the Fig. 3.5a), it is likely that the depression boundaries provide a source of copper atoms while the protrusion boundaries provide a drain. Fig. 3.5a shows the large scale STM image with both well-ordered (type B) and less-ordered facets (type A). The left and right sides are type A facets with a type B facet in the middle. We can see the connecting lines between vicinal type A and type B facets, which appear as either a protrusion (marked by the black arrow) or a depression line (marked by the white arrow), reflecting the different angles between the vicinal facets. Fig.3.5b is the corresponding current image, clearly showing the well-ordered C_{60} quasi-1D structures on type B facets and less-ordered C_{60} structures on type A facets. Here the surface reconstruction due to diffusion of underlying copper atoms provides the possibility for another C_{60} row to form along the straight step edges and results in quasi-hexagonal close packed 1D C_{60} stripes with the typical width of six rows. The origin of C_{60} stripes with other number of rows can be attributed to the emergence of different combinations of C_{60} chains, such as two bimolecular chains emerging into a stripe with five C_{60} rows.

3.5 Other Structures

Besides the aforementioned quasi-1D C_{60} chained and striped structures on rippled graphene, we also have some other interesting structures during our measurements, including the single C_{60} chain structure (Fig. 3.8) and rhombic shaped structures (Fig. 3.9).

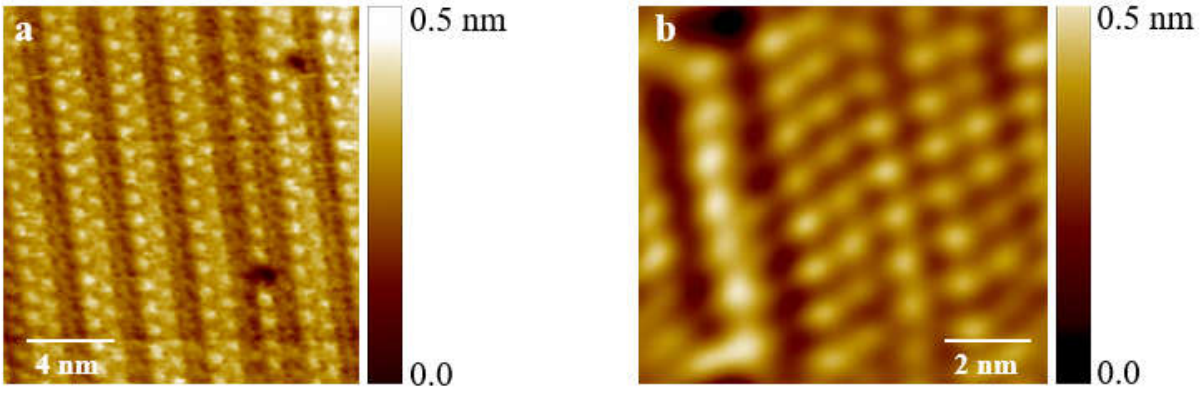

Fig. 3.8. 1D single, bimolecular and trimolecular C_{60} chains. (a) 1D single, bimolecular C_{60} chains on rippled graphene (V_s = 1.90 V, I = 0.40 nA). (b) High-resolution image of single molecular, bimolecular and trimolecular C_{60} chains (V_s = 1.95 V, I = 0.50 nA).

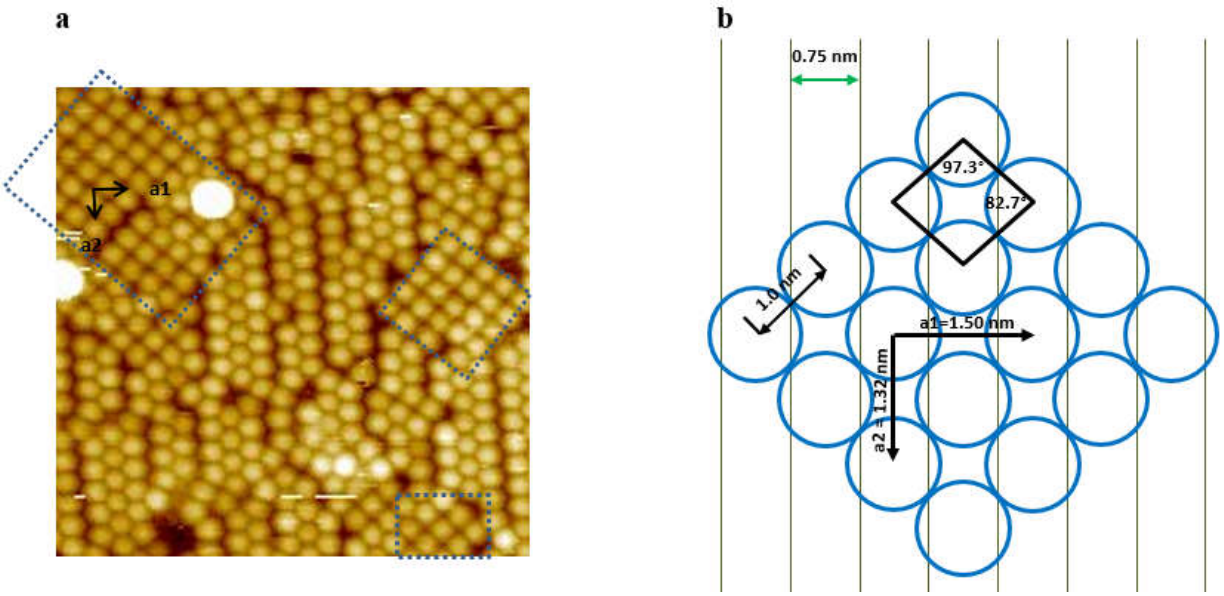

Fig. 3.9. Self-assembled rhombic shaped C_{60} structures on rippled graphene. (a) High-resolution STM image of rhombic shaped C_{60} structures on rippled graphene (V_s = 2.10 V, I = 0.30 nA). (b) Schematic drawing of the rhombic shaped C_{60} arrangement.

The C_{60} single chains and rhombic structures appear after direct deposition of C_{60} molecules, without any further annealing. The existence of the single molecule chain structure further confirms the mechanism of formation of the bimolecular and the trimolecular chains in our previous discussion part. For the rhombic structure (dashed rectangular area in Fig.3.9 a), we define a1 and a2 in the diagonal directions of the rhombic as the characteristic lengths. Surprisingly, the dimension of a1 is 1.5 nm, exactly double the size of the graphene ripple periodicity, and a2 has the dimension of 1.32 nm, which form a rhombic shape with one of the supplementary angle as 82.7˚. This rhombic structure of perfectly matches our rippled graphene substrate shown in Fig. 3.9 b. In the modeling process, we find C_{60} molecules can form this rhombic structure if they are exactly in the valley sites of graphene ripples. That means all the C_{60} molecules occupy the most stable sites on the rippled graphene substrate in the rhombic structure.

3.6 Conclusion

In summary, our results demonstrate that novel C_{60} 1D structures can be realized on rippled graphene. The chain width is controllable by tuning the temperature, with a range from single C_{60}

to three C_{60} molecules, and then to a quasi-hexagonal close packed 1D stripe structure. Our results pave a way for fabricating 1D C_{60}/graphene hybrid structures. In our experiments, temperature is the main tunable parameter. Based on the subtle balance between the intermolecular and the molecule-substrate interactions, as well as the size of the ripples due to the moiré patterns, we expect that we will be able to further tune and control the 1D C_{60} molecule structures on rippled graphene by varying the size of the ripples, the coverage of adsorbed C_{60} molecules, and the temperature.

Chapter 4. STM Measurements of Donor and Acceptor Molecular Nanostructures: C_{60} and PTCDA

4.1 Introduction

Within two decades, organic solar cells have risen to rival the power conversion efficiencies seen in conventional silicon solar cells, with up to 1% and 10% power conversion in bilayer and bulk heterojunction solar cells respectively [66-71]. Unlike the older designs of single-layer solar cells, bilayer and bulk heterojunction solar cells utilize p-n junctions, allowing incident photons to form excitons, bound electron-hole pairs, in the n-type electron donor region [63-65]. In bulk heterojunctions, the excitonic lifetime is long enough for excitons to traverse to the large donor-acceptor interface, where they are dissociated to electrons and holes. To create efficient organic solar cells, however, different factors that would impact their efficiencies need to be considered, such as solvent/thermal annealing, weight ratios between donor and acceptor, as well as the thickness of the active layer [74-77]. Of these different factors, the active layer plays a significant role in the solar cell's performance, so one of the challenges is to choose suitable donor and acceptor materials for the active layer that maximize power conversion efficiency [78]. Previous research has tested many combinations of donors and acceptors [70, 73, 79-86]. There are also numerous types of organic solar cells according to different choices of active layer, including small molecule-small molecule, small molecule-polymer, and polymer-polymer [78, 87-92]. In our work, we test C_{60}-PTCDA bilayer solar cells.

Bulk heterojunctions are based on two types of materials: electron acceptor and electron donor. C_{60}, as a good donor, has been studied in many works related to the photoexcitation [73, 81-83]. Meanwhile, as a small molecule, it is easy to determine the morphology in the hybrid structure. PTCDA, as a good electron acceptor for C_{60} according to their energy levels, can be combined together with C_{60} in the potential organic solar cells. PTCDA is an organic dye molecule and an organic semiconductor widely used as a precursor to a class of molecules known as rylene dyes, which are useful for pigments and dyes. It is a dark red solid with low solubility in aromatic solvents. This compound has attracted much interest as an organic semiconductor. In this chapter, we will focus on the submonolayer of C_{60} and PTCDA on wrinkled graphene. Research on these

binary molecular nanostructures may potentially pave a way for improving the efficiencies of organic solar cells in the future.

4.2 Experimental Methods

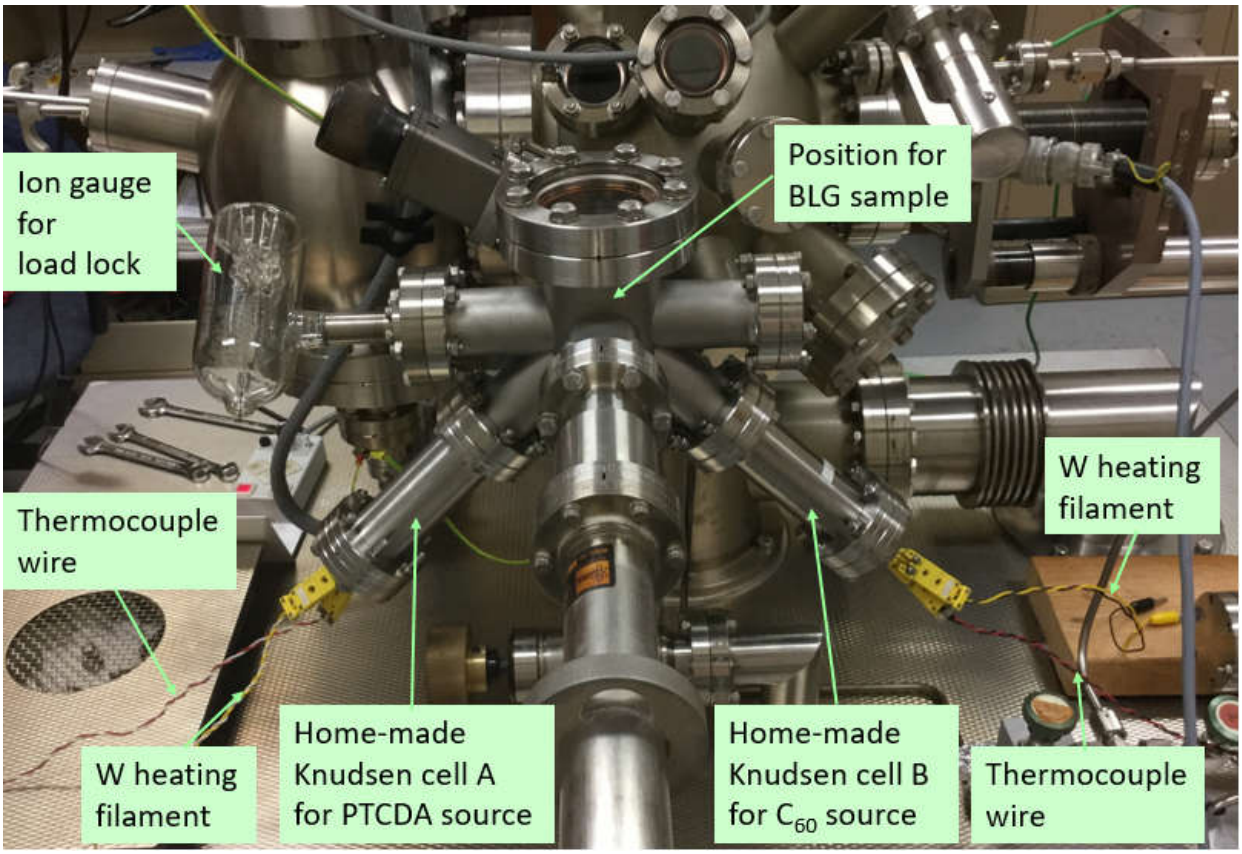

Fig. 4.1. The setup for thermal deposition in the load lock chamber of the room temperature STM (RT-STM). The home-made Knudsen cells A and B are filled with PTCDA and C_{60} powders, respectively. When the temperature of two molecules is high enough, the graphene substrate will be transferred to the specified position in the chamber, facing down, with an angle of 45˚ relative to the gas flow of molecules. An ion gauge is used to monitor the pressure in the load lock chamber.

In order to control the deposition rate of both C_{60} and PTCDA molecules, we have done many test experiments and related calibrations. Before the evaporation of C_{60} and PTCDA molecules, the graphene grown by the CVD method on Cu foil is annealed for 12 hours at 693 K in the preparation chamber with a base pressure of low 10^{-10} Torr. PTCDA powder (TCI AMERICA, 99.0% purity) is loaded into the homemade Knudsen cell A mounted in the load lock of the RT-STM system. C_{60} powder (MER Corporation, 99.5% purity) is loaded into the homemade Knudsen

cell B shown in Fig. 4.1. The PTCDA and C_{60} sources are degassed at a pressure of low 10^{-7} Torr before deposition. All experiments are carried out in an UHV STM system (Omicron RT-STM). C_{60} and PTCDA molecules are deposited simultaneously onto graphene at the background pressure below 2.0×10^{-8} Torr at a deposition rate of 1.0 ML/min. During the deposition process, the graphene substrate is kept at 413 K. This well-prepared sample is then subsequently annealed at 423 K for 1 hour in the preparation chamber of the RT-STM with the base pressure at low 10^{-10} Torr. All the STM measurements are performed at room temperature in the STM characterization chamber with a base pressure of about 1.9×10^{-10} Torr.

4.3 Results and Discussion

PTCDA and C_{60} molecules are deposited simultaneously onto graphene substrate. After post-deposition annealing at 423 K for one hour, we observe small atomically flat facets with typical sizes ranging from 250 nm^2 to 40000 nm^2. These facets are covered by PTCDA or C_{60} or just bare, most of facets can be classified into three predominant types based on the distinguishable surface characteristics, labeled as type A, type C and type D. On type A facets, graphene forms normal flat or hexagonal close packed Moiré patterns, and either PTCDA or C_{60} forms normal herribone structures or hexagonal close packed structures. On type C and type D facets, we get the large curved wrinkled graphene structures with height modulation from 0.2 nm to 0.4 nm and periodicity from 3.2 nm to 5 nm. The difference between type C and type D facets is that type C facets have quasi-1D wrinkles, but type D facets have quasi-2D perpendicular wrinkles. PTCDA or C_{60} just randomly grows on the whole substrate, so both molecules on three types of facets are observed.

4.3.1 Quasi-1D Wrinkled Graphene/Cu (Type C)

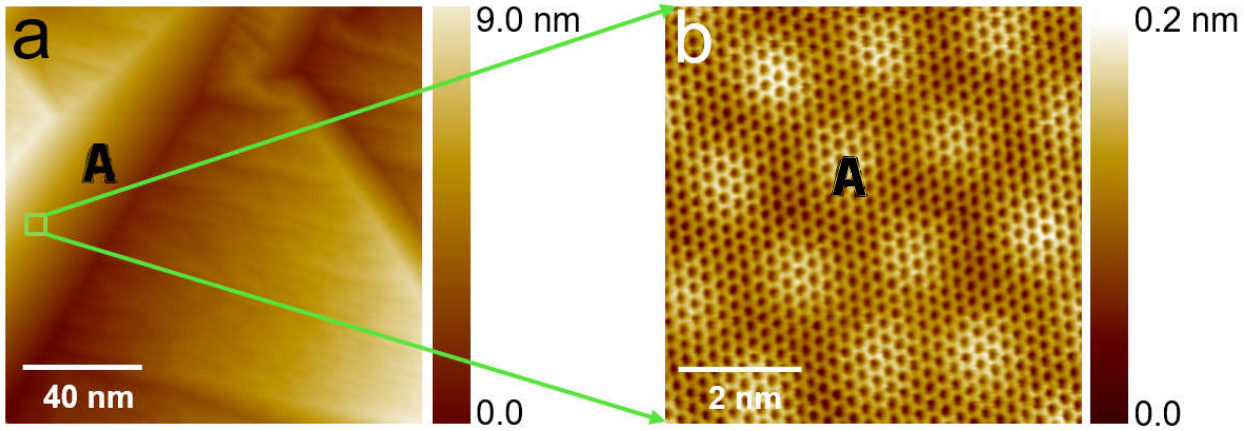

Fig. 4.2. STM topographic images of graphene on Cu showing graphene moiré pattern labeled as A. (a) Large area STM topographic image of graphene (V_s = -1.850 V, I = 0.340 nA). (b) Atomic STM image of the flat moiré pattern graphene type A, measured from the green squared region in (a) (V_s = -1.850 V, I = 0.450 nA).

We check our annealed graphene on copper foil substrate first before the molecular deposition process. On one spot of the bare graphene substrate, type A graphene forms moiré pattern labeled with the capital letter A in image 4.2a. From the zoomed-in atomic STM image in Fig. 4.2b, we can clearly observe the moiré pattern due to the superposition between graphene and Cu(111) facet. The moiré pattern has a hexagonal super lattice with the periodicity of 2.0 nm , a classical moiré pattern of graphene on Cu(111) facet with a misorientation-angle of around 7˚ that has already been reported by Li Gao et al. [131]. Except for this small area flat graphene in Fig. 4.2a, all the other surrounding facets present as wrinkled properties. In order to obtain more details about these special wrinkles, we will explore them next.

Following the principle of researching from simple surfaces to complicated ones, we will talk about the quasi-1D graphene wrinkles first, then the quasi-2D wrinkles.

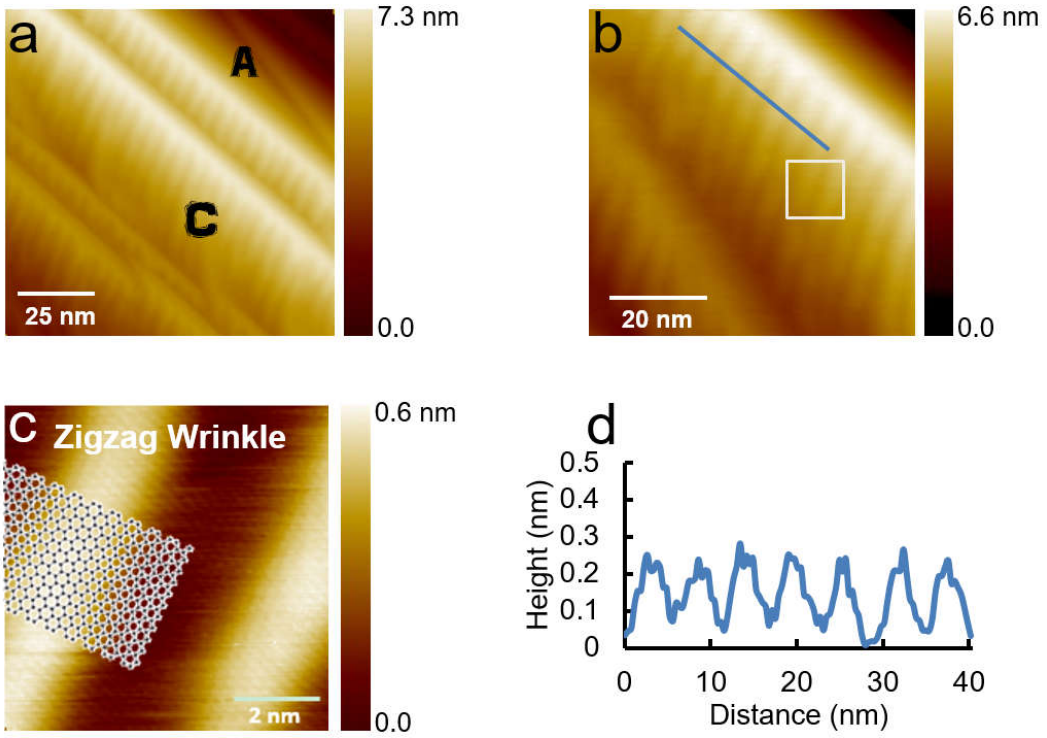

Fig. 4.3. STM topographic images of wrinkled graphene type C on Cu. (a) Large area STM topographic image of the wrinkled graphene showing linear periodic modulation (V_s = -2.340 V, I = 0.110 nA). (b) High-resolution STM image of type C wrinkled graphene (V_s = -0.340 V, I = 1.900 nA). (c) Atomically resolved STM image of the wrinkled graphene measured from the white squared region marked in (b). The schematic model on top of it shows the wrinkles along zigzag direction (V_s = -0.280 V, I = 1.900 nA). (d) Line profile perpendicular to the wrinkled graphene (marked as a blue line in (b)) showing the periodic modulation.

Besides the flat graphene facet we presented in Fig. 4.2, we observe another facet with quasi-1D wrinkled graphene structures, labeled as C in Fig. 4.3. On this facet the graphene forms quasi-1D wrinkles along one single orientation. The high-resolution STM image (Fig. 4.3c) reveals the honey-comb lattice of graphene on top of each wrinkle measured from the white frame in Fig. 4.3b. In order to vividly illustrate the wrinkled graphene, we directly draw the schematic honey-comb graphene wrinkle model on top of this atomic image shown in Fig. 4.3c, which shows these wrinkles are zigzag graphene wrinkles. Our measurement is consistent with the simulation from density functional theory based tight-binding approximation and the ab initio calculations for the force model, due to the lower energy of zigzag wrinkles at the total energy minimum compared to that of the armchair wrinkles [139, 140]. From this line profile shown in Fig. 4.3d measured along

the blue line in Fig. 4.3b, we know that this group of wrinkles has the periodicity of 5 nm with the modulation of 0.24 nm. Typically, these type C quasi-1D wrinkles have the height in the range from 0.2 nm to 0.4 nm, and their periodicities are around 3.2 nm to 5 nm. The size of these quasi-1D graphene wrinkles is much bigger than our previous graphene moiré patterns, which can rule out the formation of the misorientation between graphene and copper substrate [1].

4.3.2 Quasi-2D Wrinkled Graphene/Cu (Type D)

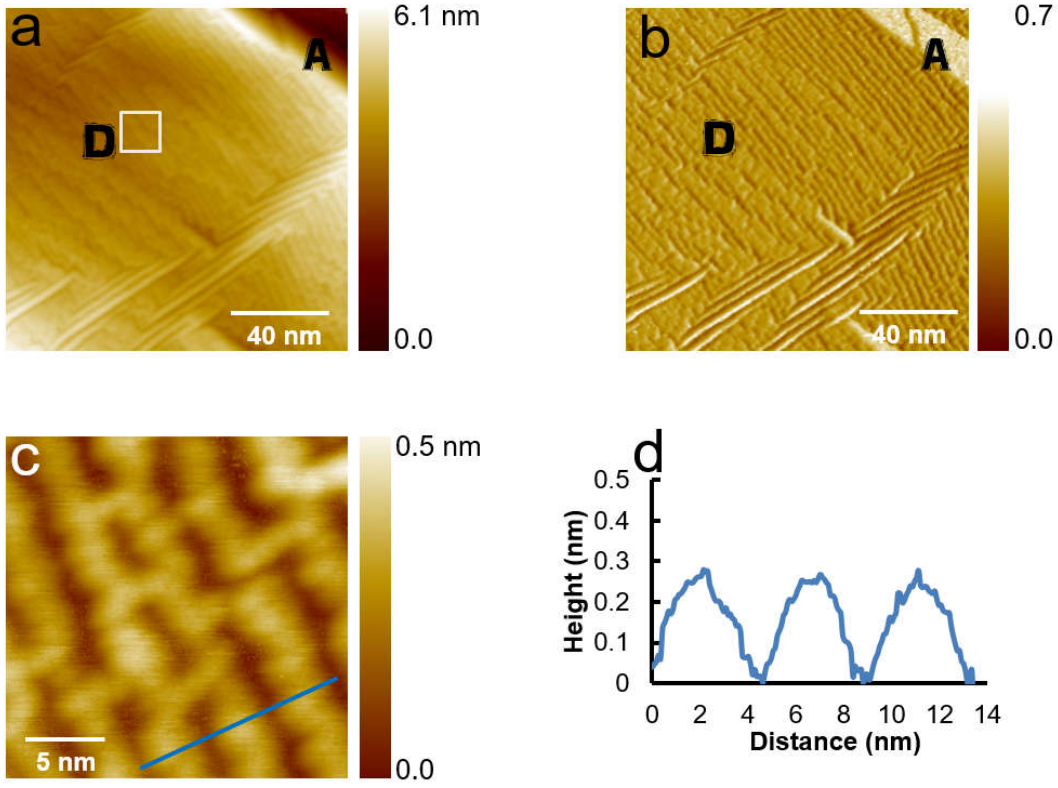

Fig. 4.4. STM images of graphene showing type A and type D facets. (a) STM topographic image of continuous graphene on two different Cu facets, labeled as A and D: flat graphene and quasi-2D wrinkled graphene, respectively (V_s = -2.74 V, I = 0.045 nA). (b) STM current image of (a) clearly showing the two different graphene nanostructures. (c) High-resolution STM image of the quasi-2D wrinkled graphene, measured from the white squared region marked in (a) (V_s = -2.600 V, I = 0.068 nA). (d) Line profile along the blue line in (c) showing the periodic modulation of graphene wrinkles with a spatial period of 4.2 nm and a height of 0.27 nm.

Graphene wrinkles are quasi-2D wrinkles on this type D graphene facet in Fig. 4.4. Compared to the quai-1D type C graphene wrinkles, they are shorter, crossed, and more complicated. This quasi-2D graphene has one dominant wrinkled direction, especially shown in the closer high-resolution STM image in Fig. 4.4c. The blue line crosses three leading wrinkles in Fig. 4.4c. We measure its wavelength as 4.2 nm and the modulation as 0.27 nm.

According to our observation, periodicities of either quasi-1D or quasi-2D wrinkles are 4 nm in average and modulations are in the range of 0.2 nm to 0.4 nm. In order to get more details for the wrinkled facets, we try to inspect different characteristics of these structures.

4.3.3 The Formation of Wrinkled Graphene Nanostructures

To gain detailed insight into the mechanisms of these three types of nanostructures, we use STM to characterize the bare graphene areas with both flat and wrinkled surfaces. We find the flat graphene surface is always on Cu(111) facet (labeled as A in Fig. 4.2a, 4.3a and 4.4a), which can therefore form a hexagonal moiré super lattice. All the other copper facets lead to the formation of graphene wrinkles. Dae Woo Kim et al. demonstrated that the surfaces of Cu foils were easily wrinkled to a particular direction along abundant terraces and step edges except Cu(111) surface due to the weak interaction between graphene and copper foil [141]. This is reasonable because graphene and Cu(111) facet have similar symmetries and rather matched lattice constants, so their interactions are relatively stronger than the other copper facets. Although, in 2012, Levente Tapasztó et al. reported a wrinkled graphene on Cu(111) measured through STM, where graphene nano wrinkles exhibited highly regular periodic oscillations, with a wavelength of ~0.7nm and modulation of ~0.1nm, their wrinkle structures were only formed in confined vacancy trenches with well-defined widths of 5 nm and length in the range of 20 nm to 80 nm, different from our continuous wrinkles along certain whole Cu facets [139]. Also, their nano wrinkles have much smaller wavelength and amplitude than the wrinkles we measured. We can conclude they are two different kinds of graphene nanostructures.

During our experiments, we find either type C quasi-1D wrinkled or type D quasi-2D wrinkled graphene facet always appears together with the flat graphene facet type A. Sometimes we can observe the three different nanostructures in one image in our STM measurement (Figs. 4.5a and 4.5b). But these three facets can be easily distinguished by their different characteristics: type A is

an overall flat surface; type C shows quasi-1D wrinkled nanostructure and type D has quasi-2D wrinkles. As we already confirmed, the flat facet is on top of Cu(111) facet, so the other two wrinkled facets C and D are certainly not on Cu(111) facet. They may have a larger possibilities found on Cu(100) and Cu(110), the second two most common copper facets.

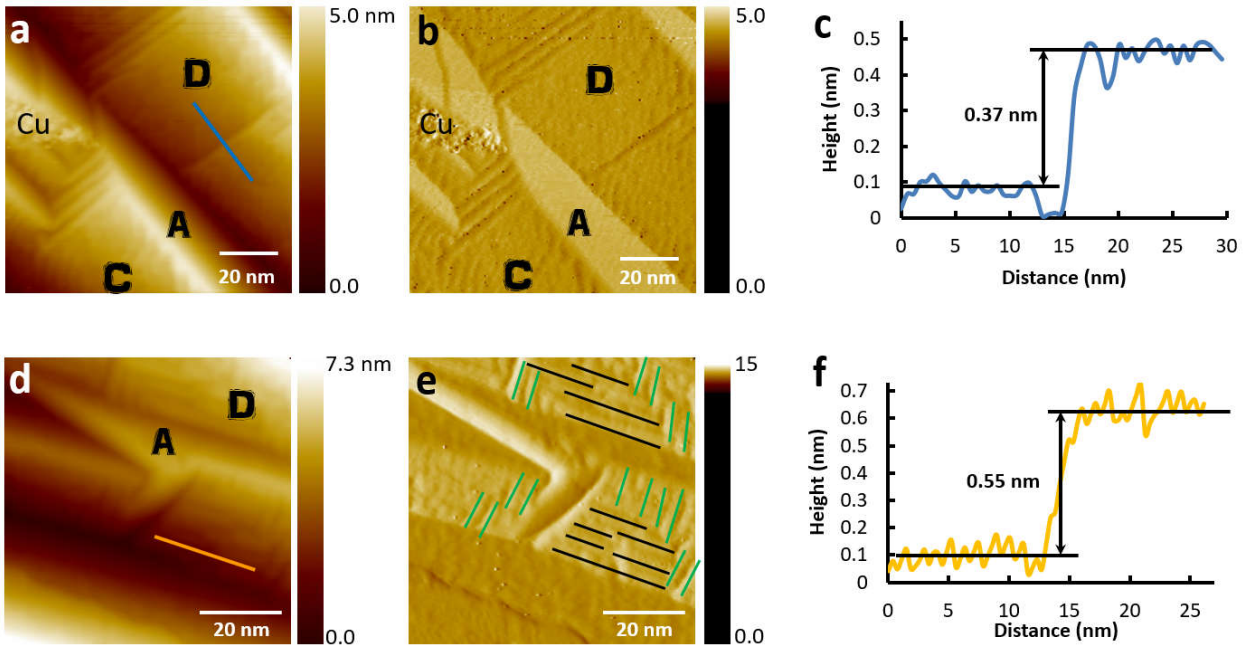

Fig. 4.5. STM images of wrinkled graphene on Cu(100) facet. (a) STM topographic image of continuous graphene forming on facets A, C and D of Cu foil (V_s = -1.900 V, I = 0.060 nA). (b) Current image of (a). (c) Line profile of the wrinkled graphene on Cu(100) facet, measured along the blue line in (a), and the black arrow shows the height of the step. (d) STM topographic image of continuous graphene showing type A and type D nanostructures (V_s = -2.200 V, I = 0.520 nA). (e) Current image of (d). Green and black lines indicate two orientations of wrinkles. (f) Line profile spans two terraces along the orange line in (d) and the black arrow indicates this step height.

These two sets of type C and D graphene wrinkled structures are attributed to the case where the underlying Cu facet is Cu(100) as shown in Fig. 4.5a and Fig. 4.5d. To confirm that, we measure the height of step edges on the two large facets. The step height of 0.37 nm shown in Fig. 4.5c measured along the blue line in Fig. 4.5a is the characteristic bilayer step height for Cu (100) terrace [126, 127]. However, this kind of linear modulation of graphene is not due to the square lattice symmetry of the Cu(100) surface that has been experimentally observed before or the ripple

graphene we discussed in chapter 3.3.4 [123, 124, 126]. That modulation is only 0.5 Å, much smaller than what we observe now. According to previous studies, linear graphene moiré patterned ripples are formed with different periodicities with modulation less than 0.1 nm, much smaller compared to our wrinkle structures (from 0.2 nm to 0.4 nm) [123, 124, 126]. In Figs. 4.5(d, e, and f), another group of winkles clearly shows typical quasi-2D graphene wrinkles labeled with green and black lines in current image (Fig. 4.5e) with step height 0.55 nm (Fig. 4.5 f). This height demonstrates this step is attributed to triple layers of Cu(100). Another interesting detail in Fig. 4.5a and Fig. 4.5b is the existence of rough copper area labeled as Cu, which gives us a hint about the formation of graphene wrinkles.

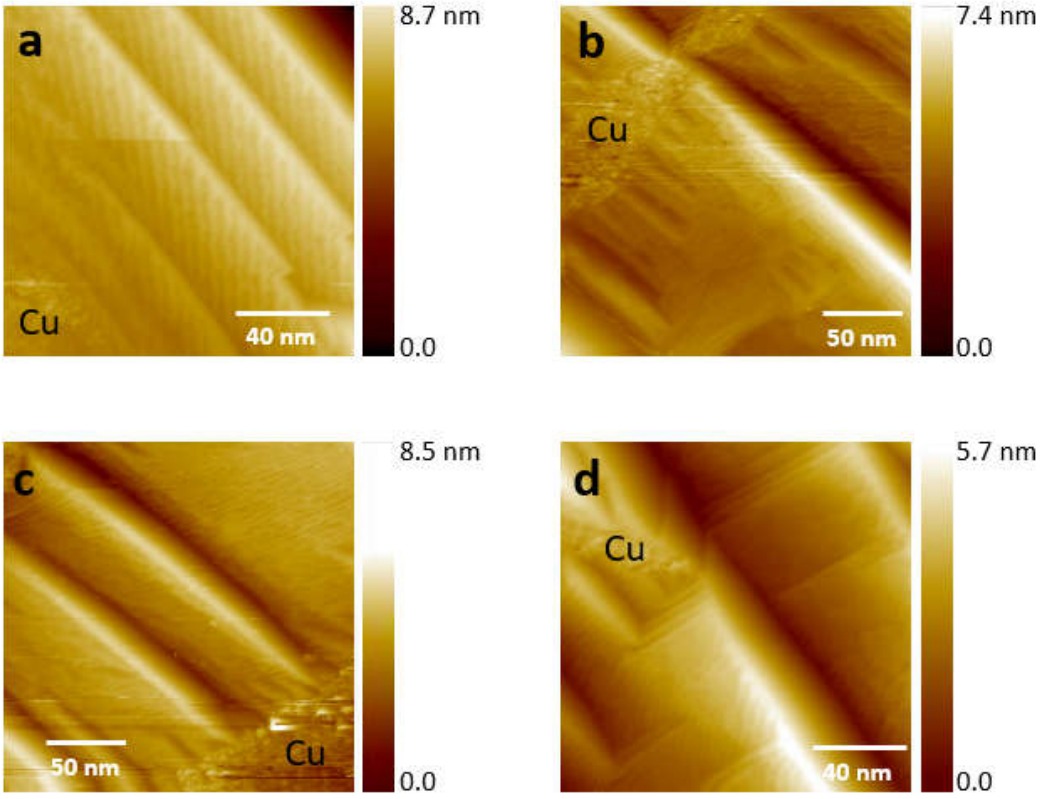

Fig. 4.6. Large-scale STM images of wrinkled graphene near edges. Unlabeled clean areas are wrinkled graphene, and rough areas labeled as Cu in all four images are amorphous oxidized Cu. Scanning parameters are (V_s = -2.300 V, I = 0.100 nA) for (a), (V_s = -2.700 V, I = 0.0380 nA) for (b), (V_s = -2.700 V, I = 0.0380 nA) for (c), and (V_s = -1.900 V, I = 0.040 nA) for (d), respectively.

With that amorphous oxidized Cu boundary in mind, we find these wrinkled structures are always around bare copper boundaries, as shown in Fig. 4.6. Our graphene on Cu foil substrate, annealed only at 693 K, defined as low-temperature annealing according to the report by Jongweon Cho et at., still keeps an amorphous oxidized copper area, with a distinct discontinuity around the graphene island boundary [124]. In these four STM images of Fig. 4.6, we can see the wrinkled graphene and flat graphene on staggered facets surrounding the oxidized copper area, which provides us an excellent tip for the formation of these wrinkled graphene.

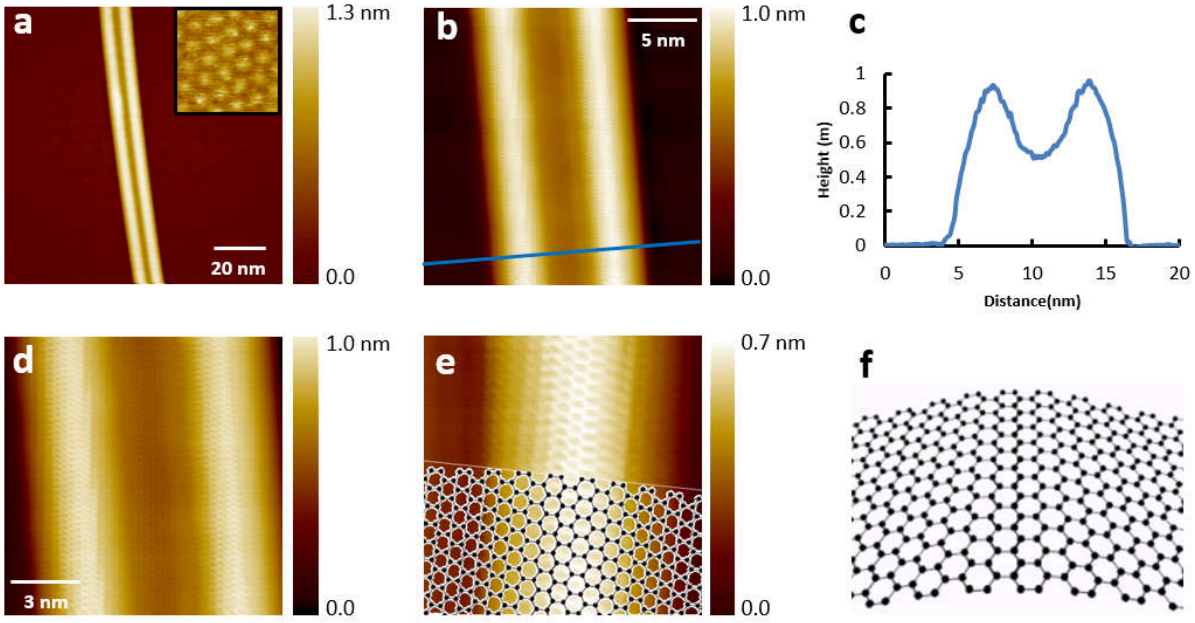

Fig. 4.7. STM topographic images of a collapsed wrinkle of graphene. (a) Large-scale STM topographic image of continuous graphene forming a collapsed wrinkle on Cu(111) (V_s = -1.06 V, I = 0.315 nA). The insert STM image shows the graphene moiré pattern on the right flat area (V_s = -0.750 V, I = 0.315 nA). (b) Zoomed-in image of the collapsed wrinkle (V_s = -0.600 V, I = 0.850 nA). (c) Line profile of the collapsed wrinkle, measured along the blue line in (b). (d) Further zoomed-in STM image of the collapsed wrinkle (V_s = -0.560 V, I = 0.8750 nA). (e) Atomically resolved STM image of one of the collapsed wrinkle showing graphene honey-comb lattices (V_s = -0.560 V, I = 0.8750 nA). (f) Schematic model for the wrinkle.

Besides the step height and the oxidized copper boundary information, we have more data related to the morphology and the formation mechanism of periodic graphene wrinkles. The insert

image of graphene moiré pattern in Fig. 4.7a clearly demonstrates the collapsed wrinkle is formed on Cu(111) facet. This long and uniform collapsed graphene wrinkle on Cu(111) surface can demonstrate that Cu(111) facet inhibits the growth of periodic graphene wrinkles on it. The wavelength and modulation of this collapsed wrinkle measured along the blue line in Fig. 4.7b are in the range of periodic wrinkles we mainly discuss in this chapter. We also have beautiful atomic images of this collapsed wrinkle shown in Fig. 4.7d and 4.7e, from which we can tell the curved wrinkles are along the zigzag direction as the aforementioned wrinkles. This consistency helps us to understand the aforementioned periodic wrinkles a little more. Firstly, the size of this collapsed wrinkle is consistent with the periodic wrinkles. Secondly, the collapsed wrinkle is on Cu(111) surface, but the periodic wrinkles are not on Cu(111) facet, which indicates that the Cu(111) facet is not suitable for the growth of periodic wrinkles. This discovery is consistent with previous observation and theory [141]. Thirdly, the total height of the collapsed wrinkle in Fig. 4.7c is around 0.9 nm, while the height of the saddle is only 0.4 nm, so the pair peaks of the wrinkle are freestanding. These three characteristics demonstrate that the periodic wrinkles we observed in our system are real freestanding suspended wrinkles, not the normal moiré pattern for graphene on different copper facets.

From all these observations, it is reasonable to conclude that the underneath of type A graphene is Cu(111) due to their relatively stronger interaction [141]. Based on the periodicity and the modulation of the real wrinkles, we are able to conclude that these quasi-1D or quasi-2D wrinkles are more complicated than the linear moiré pattern of graphene ripples on Cu(100) facet in chapter 3. It is related to different interactions between graphene and different underneath Cu facets, the boundary between graphene and Cu foil, the lattice mismatch between graphene and Cu foils, and also the mismatch of thermal expansion between graphene and Cu foil [141-143].

In order to systematically understand the formation of the graphene wrinkles along zigzag direction, we need to consider the negative thermal expansion coefficient (TEC) of graphene, because the copper metal has a positive TEC. Extra volume of graphene will be left on copper foil when the annealing temperature begins to go down. This extra-length graphene can diffuse in the middle domain of graphene, but there is no extra space to diffuse along the boundaries. Meanwhile the rough oxidized copper along the graphene boundaries shows higher energy barrier for graphene, so there will be relatively more graphene to distribute along the boundaries. The extra graphene will prefer to form wrinkled structures instead of rough random structures. Because the free energy

of wrinkles is lower than that of the rough structure when the temperature is lower than a specific temperature due to the compression-relaxation mechanism [144]. However, the zigzag wrinkles have lower free energy compared the armchair wrinkles according to the ab initio calculations [140]. Thus, the excess graphene will form the zigzag wrinkles surrounding oxidized copper on copper foil except the Cu(111) facet [141].

4.3.4 C_{60} on Wrinkled Graphene

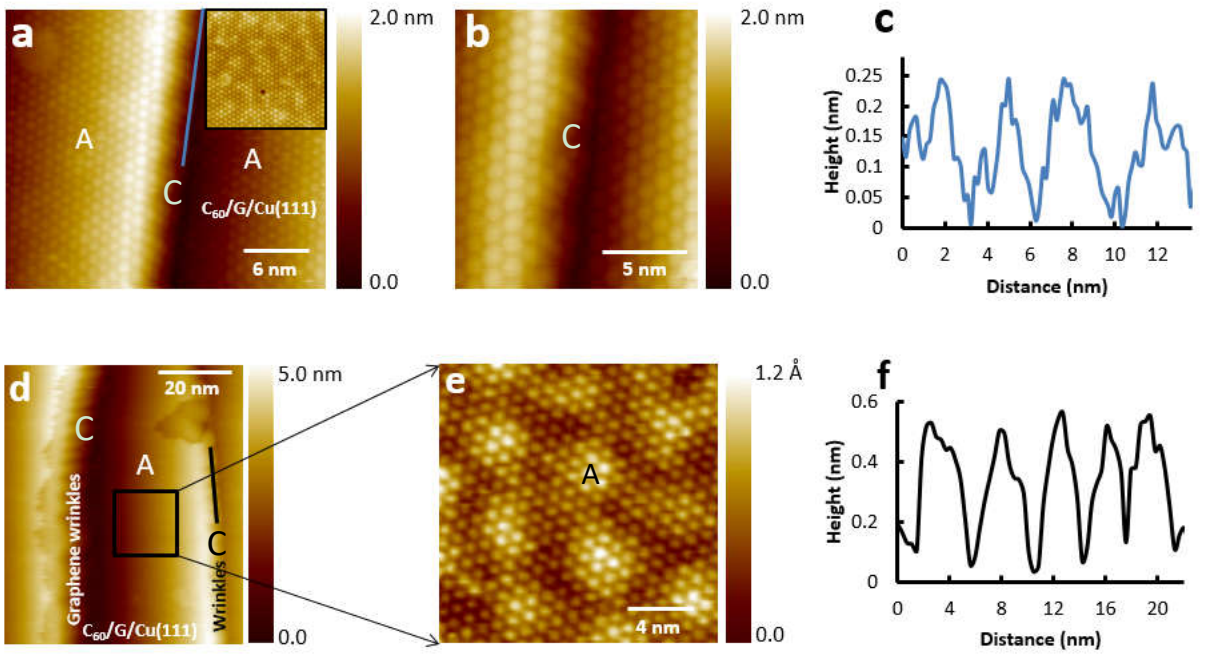

Fig. 4.8. STM images of self-assembled hexagonal close-packed C_{60} on type A and type C graphene. (a) Large-scale STM topographic image of C_{60} on graphene with superlattice showing well-defined moiré patterns on facet A. The inset image in (a) shows moiré pattern of C_{60} on facet A. The letter 'G' indicates graphene (V_s = -2.80 V, I = 0.090 nA). (b) Zoomed-in STM image of self-assembled hexagonal close-packed C_{60} on graphene type C wrinkles (V_s = -2.80 V, I = 0.090 nA). (c) A line profile of C_{60} on wrinkled graphene along the blue line in (a). (d) Another large-scale STM topographic image of the C_{60} on type A and type C graphene (V_s = -2.80 V, I = 0.060 nA). (e) High-resolution STM image of C_{60} moiré pattern image of type A measured from the black squared region of (d) (V_s = -2.80 V, I = 0.060 nA). (f) A line profile showing the periodicity and modulation of C_{60} on wrinkled graphene along the black line in (d).

Since wrinkled graphene type C, type D and flat graphene type A coexist in the same substrate, it is easy to understand C_{60} molecules can be absorbed on all these graphene nanostructures. From Figs. 4.8a and 4.8d, we can observe C_{60} molecules distributed on two types of graphene wrinkles due to different copper facets. On facet A, C_{60} molecules form hexagonal close packed structure shown in Fig. 4.8e. The inset image of Fig. 4.8a shows the same hexagonal close packed C_{60} on type A graphene on Cu(111) too. Then the other slant facets in Figs. 4.8a and 4.8d are definitely not on Cu(111). Its magnified STM image (Fig. 4.8b) reveals the hexagonal close packed arrangement of C_{60} on quasi-1D wrinkles. We also check the wave size of quasi-1D C_{60} wrinkles. Similar to the graphene wrinkles in Fig. 4.3, the wavelength of the C_{60} wrinkles is about 3.2 nm (blue line shown in Fig. 4.8c) with a modulation of 0.22 nm, which is smaller than that of the graphene wrinkles in Fig. 4.3d, but 0.22 nm is correct according to a simple geometric calculation. The other C_{60} wrinkles labeled by the black line shown in Fig. 4.8f have the same size as the graphene wrinkles. This consistency of graphene and C_{60} wrinkles has confirmed they are both relative to the same kind of wrinkles.

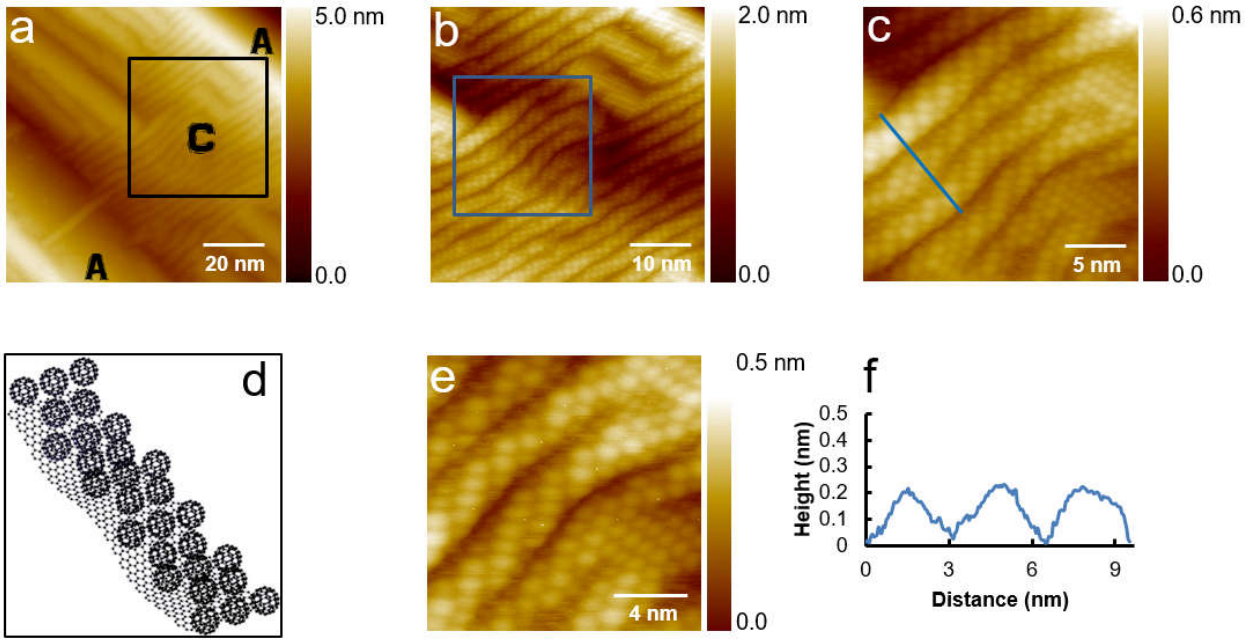

Fig. 4.9. STM images of C_{60} on type C wrinkled graphene. Self-assembled quasi-hexagonal close-packed C_{60} on wrinkled graphene. (a) Large-scale STM topographic image of the C_{60} on wrinkled graphene showing well-defined linear periodic modulated wrinkles defined as C facet (V_s = -2.60

V, I = 0.060 nA). (b) Zoomed-in STM image (measured from the black frame of (a)) of C_{60} on long periodic graphene wrinkles (V_s = -2.60 V, I = 0.050 nA). (c) High-resolution STM image (measured from the blue squared region of (c)) of the quasi-hexagonal close-packed C_{60} on quasi-1D wrinkled graphene (V_s = -2.60 V, I = 0.040 nA). (d) A schematic model of hexagonal close-packed C_{60} on wrinkled graphene sheet. (e) High-resolution image of the quasi-hexagonal close packed C_{60} on quasi-1D wrinkled graphene, showing each molecule clearly (V_s = -2.60 V, I = 0.040 nA). (f) A line profile along the perpendicular direction of the wrinkled graphene as marked with the blue line in (c).

A typical type C graphene wrinkles with C_{60} absorbed on is shown in Fig. 4.9. This set of wrinkled images clearly show C_{60} on the long periodically curved graphene. From Fig. 4.9e, we can observe C_{60} molecules form quasi-1D hexagonal close packed structure on the quasi-1D wrinkled graphene. These wrinkles measured in Fig. 4.9f have the periodicity of 3.2 nm with the modulation of 0.21 nm, pretty consistent with the quasi-1D graphene wrinkles obtained from our previous measurement.

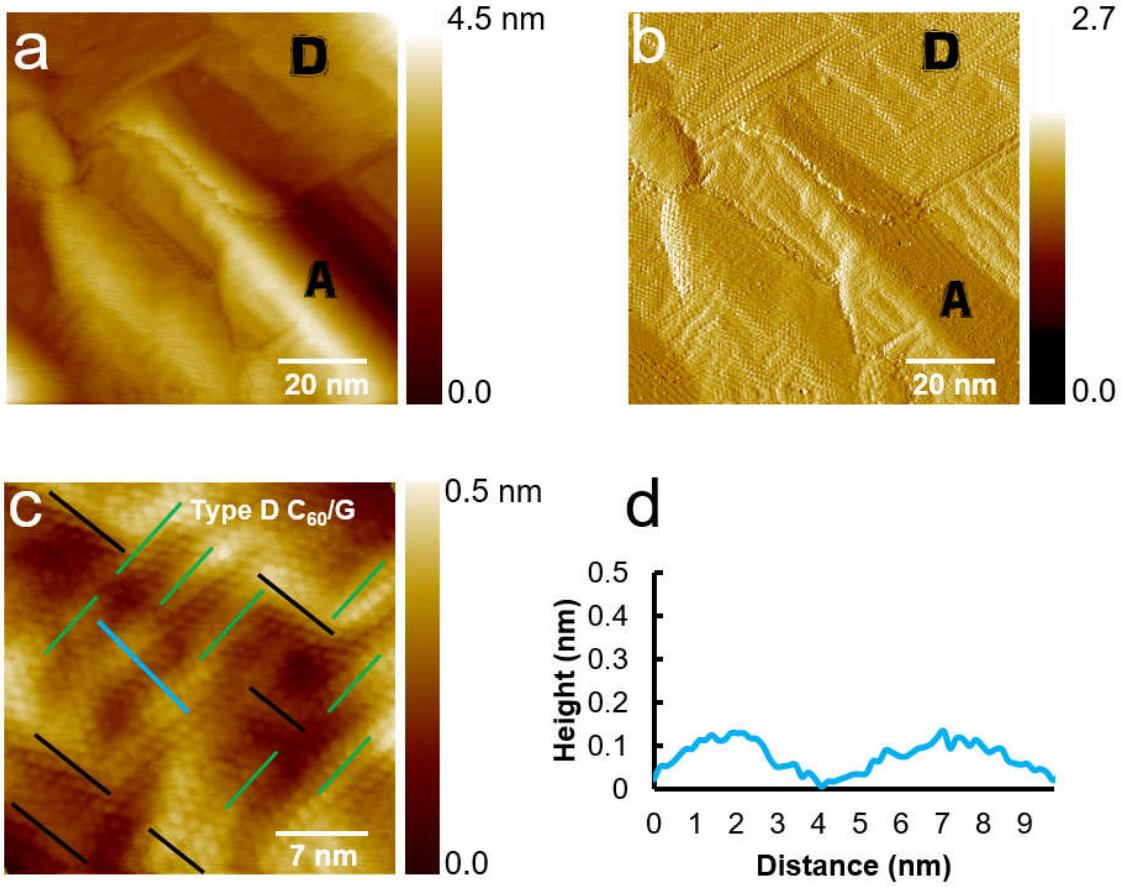

Fig. 4.10. STM images of self-assembled hexagonal close packed C_{60} on wrinkled graphene type D. (a) and (b) Large-scale STM topographic and current image of the C_{60} on graphene(V_s = -2.840 V, I = 0.054 nA). (c) Zoomed-in STM image of self-assembled hexagonal close packed C_{60} on graphene type D wrinkles. Black and green arrows show the perpendicular wrinkles directions (V_s = -2.740 V, I = 0.0460 nA). (d) A line profile showing the size of C_{60} molecules absorbed on type D wrinkled graphene along the blue line in (c).

Besides the coexistence of hexagonal close-packed C_{60} structures on facet A and C, hexagonal close-packed C_{60} structures on facet D are observed in our data shown in Fig. 4.10. From Fig. 4.10c, we can see these quasi-2D winkles more clearly with the help of marked green and black lines, respectively. These two wrinkled directions are perpendicular to each other. The size of these wrinkles shown in Fig. 4.10d is consistent with the quasi-2D bare graphene wrinkles shown in Fig. 4.4d. It demonstrates C_{60} still forms hexagonal close packed structure accommodated to the type D graphene wrinkles.

In a word, either quasi-1D graphene wrinkles or quasi-2D graphene wrinkles cannot influence the normal hexagonal close-packed C_{60} arrangement. We are really curious about why these wider, higher wave modulations cannot change the C_{60} arrangement as much as the smaller subtle graphene ripples in chapter 3. Thus, we compare these two main different graphene structures from both morphology and van der Waals binding energy aspects in Fig. 4.11. We use the same Y scale in 4.11a and 4.11b, so we can directly compare them. From 4.11a and 4.11b, the suspended wrinkles are much higher and obvious in morphology. However, the van der Waals binding energy difference is only 0.5 eV from the valley to the hilltop spot in Fig. 4.11d, while there is 1.1 eV difference for the graphene moiré pattern ripples shown in Fig. 4.11c, which is more than two times bigger than that of the suspended graphene wrinkle structures we discussed in this chapter [136, 138]. The binding energy differences in these two systems are due to different spaces to their underneath copper substrate: moiré pattern rippled graphene is relatively closer to the copper substrate compared to the suspended graphene wrinkles with the modulation up to 0.4 nm. Various binding energy in one system is due to different interacting areas between C_{60} and graphene at different spots. Because of the largest interacting area in the curved valley, the van der Waals binding energy is also the largest, compared to that on the flat graphene or that on the hilltop spot. From the Figs. 4.11c and 4.11d, the smaller energy difference means the smaller energy barrier for the C_{60} molecules to diffuse among these modulations, so it is much easier for C_{60} molecules to transition among adjunct valleys in the suspended graphene wrinkles to form self-assembled hexagonal close packed arrangement. This explains the reason why the bigger graphene wrinkles cannot affect the C_{60} arrangement as much as the smaller subtle graphene ripples. In return, this energy difference demonstrates that the observed quasi-1D and quasi-2D graphene wrinkles are free-standing.

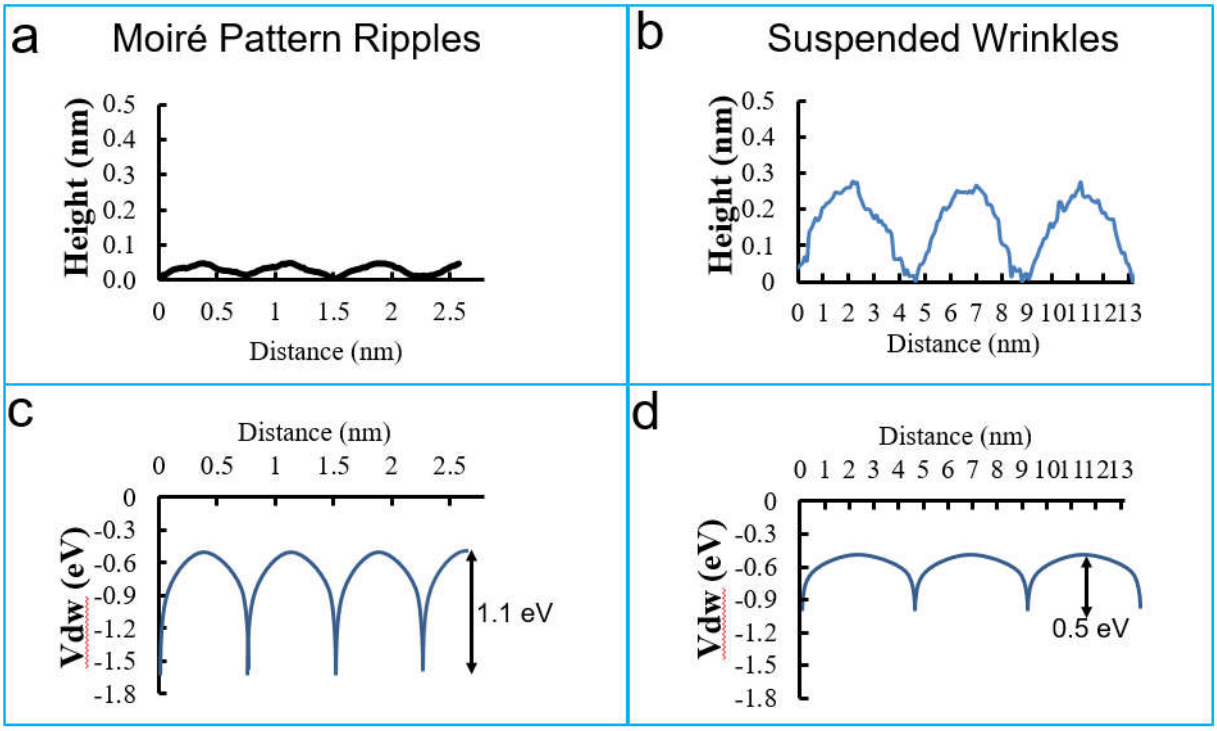

Fig. 4.11. Comparisons between moiré pattern ripples and suspended wrinkles. (a) Morphologic line for the typical 1D graphene moiré pattern ripples shown in Fig. 3.7d in chapter 3. (b) Showing the morphologic line for the typical 1D graphene suspended wrinkles. (c) Van der Waals binding energy from the valley to the hilltop point for the typical 1D graphene moiré pattern ripples shown in (a). (d) Van der Waals binding energy from the valley to the hilltop point for the typical quasi-1D suspended graphene wrinkles shown in (b).

4.3.5 PTCDA on Wrinkled Graphene

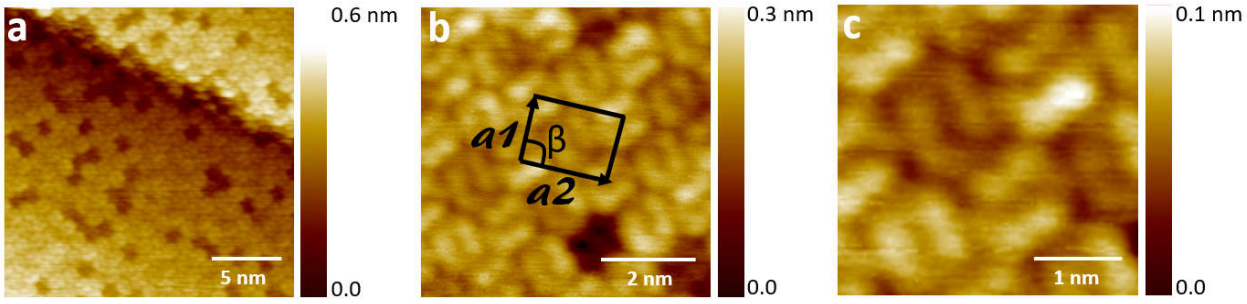

Fig. 4.12. STM images of self-assembled herringbone packed PTCDA on flat graphene. (a) Large-scale STM topographic image of the PTCDA on flat graphene (V_s = 1.800 V, I = 0.030 nA). (b)

Zoomed-in STM image of self-assembled herringbone packed PTCDA showing lowest unoccupied molecular orbital (LUMO) on flat graphene. Black arrows a1 and a2 indicate the short and long lattice vectors of a unit cell of PTCDA herringbone pattern (V_s = 1.800 V, I = 0.030 nA). (c) High-resolution STM image of herringbone packed PTCDA showing LUMO orbital on facet A (V_s = 1.800 V, I = 0.030 nA).

Because of the coexistence of C_{60} on A, C and D types of graphene, it is understandable that we can get similar PTCDA molecule distribution on all these three types of graphene nanostructures, as shown in Fig. 4.12, Fig. 4.13 and Fig. 4.14. The most common arrangement for PTCDA molecules is the herringbone pattern on graphene as reported previously [145-153]. From the large STM image of PTCDA on flat graphene in Fig. 4.12a, PTCDA can continuously cross over two terraces without changing their herringbone arrangement. The size of herringbone pattern of PTCDA can be easily measured from Fig. 4.12b with a1 = 1.300 nm, a2 = 1.960 nm, and β = 90˚, consistent with unit cell in Zhou et al. report and the β-face (102) plane of PTCDA bulk structure within the error limit. The rectangular outline drawn with the lattice vectors a1 and a2 specified on the STM image of Fig. 4.12b is to indicate one herringbone pattern unit [147, 154, 155].

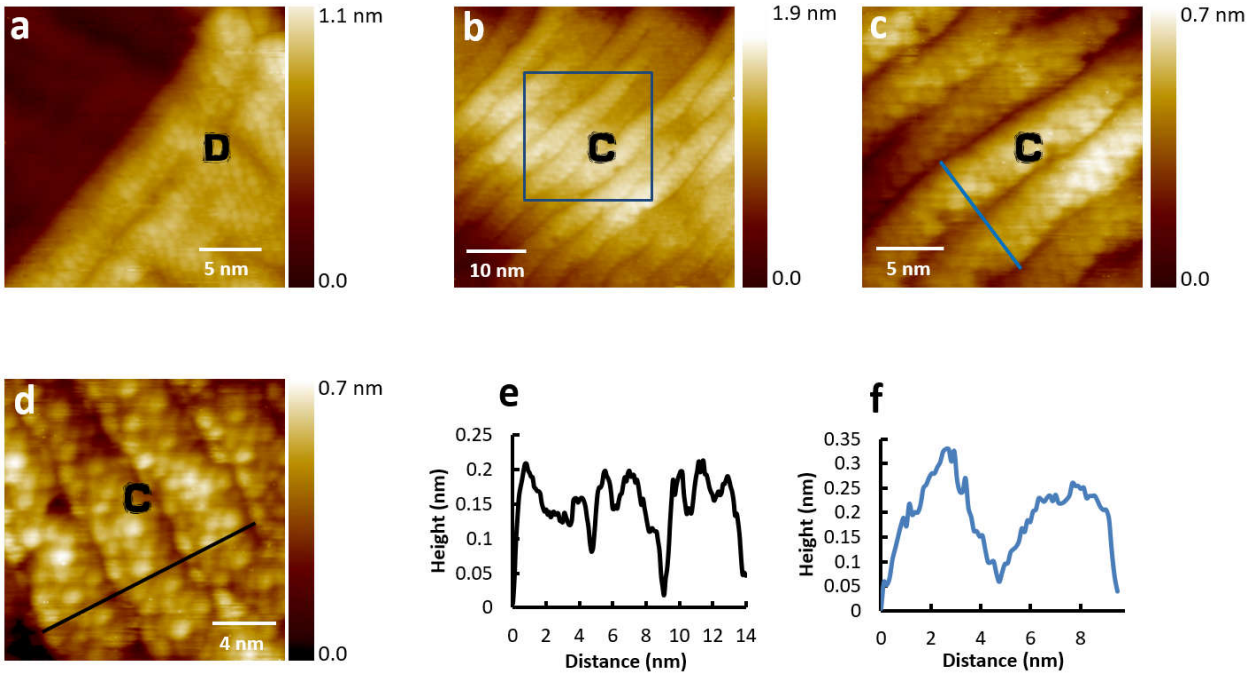

Fig. 4.13. STM images of self-assembled herringbone packed PTCDA on wrinkled type C and D graphene on Cu. (a) STM topographic image of the herringbone packed PTCDA on type D graphene wrinkles (V_s = -2.000 V, I = 0.050 nA). (b) Large STM image of herringbone packed PTCDA on long periodic type C graphene wrinkles (V_s = -2.000 V, I = 0.030 nA). (c) Zoomed-in STM image (measured from the blue frame of (b)) of herringbone packed PTCDA (V_s = -2.000 V, I = 0.032 nA). (d) Another high-resolution image of herringbone packed PTCDA on quasi-1D wrinkled graphene (V_s = -2.000 V, I = 0.053 nA). (e) A line profile showing the wavelength and the modulation of the quasi-1D wrinkles along the black line in (d). (f) A line profile showing the wavelength and the modulation of the quasi-1D wrinkles along the blue line in (c).

After measuring the herringbone pattern of PTCDA on flat graphene, we need to check the morphology of PTCDA molecules on the other two types of wrinkles, as shown in Fig. 4.13. The morphology of PTCDA on type D graphene is shown in Fig. 4.13a with two perpendicular orientations of wrinkles, which is consistent with the bare wrinkled type D graphene in Fig. 4.4d. In this area PTCDA fully covers the bottom right side of wrinkles without any defects, and the top left side is the bare wrinkled graphene. For the morphology on type C wrinkled graphene, fully arranged PTCDA on the quasi-1D long periodic graphene is shown in Figs. 4.13b and c. We also measured the size of the type C wrinkles with PTCDA self-assembled on in Fig. 4.13e and 4.13f, along the blue line in Fig. 4.13c and the black line in Fig. 4.13d. Although they have different wavelength and the modulation, the sizes of them are in the range of the type C graphene wrinkles.

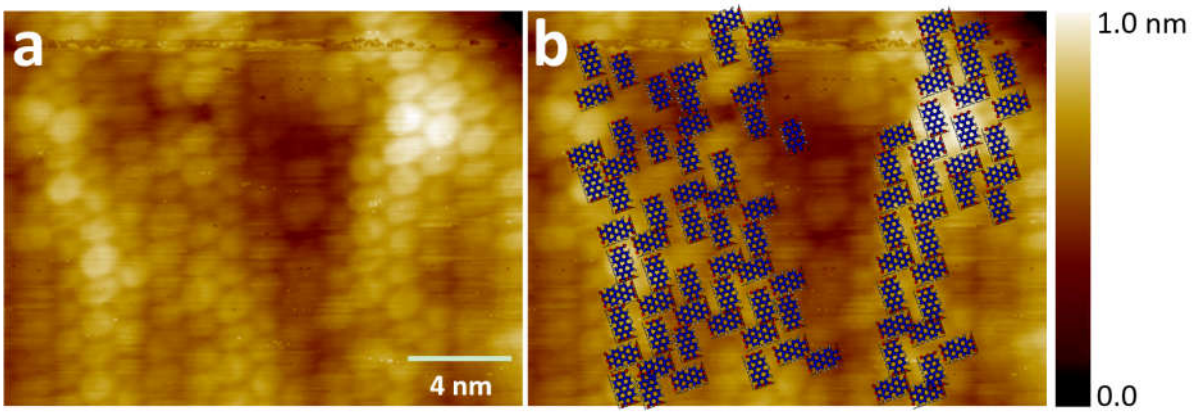

Fig. 4.14. STM images of self-assembled herringbone packed PTCDA on wrinkled graphene type C. (a) STM image of herringbone packed PTCDA on wrinkled graphene showing well-defined quasi-1D linear periodic modulated wrinkles defined as type C (V_s = -2.510 V, I = 0.042 nA). (b)

Schematic model of PTCDA arrangement showing quasi-1D herringbone packed PTCDA on type C wrinkles (V_s = -2.510 V, I = 0.042 nA).

One STM image for PTCDA molecular arrangement on top of wrinkled graphene shows the self-assembled herringbone arrangement, as shown in Fig. 4.14. From the image 4.14a. We can see the orbital structures of most PTCDA molecules on the top part of wrinkles. We combine several images in a series to obtain its molecules arrangement, as shown in Fig. 4.14b, which shows the quasi herringbone patterned PTCDA crossing the waved graphene wrinkles, with each blue schematic PTCDA standing for one PTCDA molecule. Even though some molecules are not clear enough to resolve their orbital structures, we can still see the sub-monolayer PTCDA with herringbone pattern arrangement on top of the wrinkled graphene. The wrinkled graphene does not affect the stable herringbone pattern of PTCDA, which is understandable due to the weaker interaction between PTCDA and graphene/Cu compared to their inter-molecular interactions [158-166].

4.3.6 Dynamic Decay Process of PTCDA on Graphene

Due to the weak interaction between PTCDA molecule and graphene on copper substrate, we predict that PTCDA monolayer islands should decay very easily. In order to get their dynamic decay data, we perform continuous scanning on defined areas, which is keeping the same scanning conditions at the same area. We measure three different PTCDA monolayer islands, and we can observe the decay process. The interesting thing is that in one island there are two different sub-stable PTCDA molecular arrangements. Once there is a sub-stable seed in the scanning area, as shown in the white framed region and in the bright blue curved region in Fig. 4.15a, then these two kinds of sub-stable patterns will grow and change their morphology during the scanning process. While in all these nine STM images, the PTCDA molecules in the half right side all keep self-assembled herringbone structures without any decay, even their molecular orbitals change a little because of different tip states.

We are more interested in the sub-stable structures, so we will focus on discussing the dynamic process of the sub-stable structures in the following part. We define the sub-stable pattern in the

white curved frame as type I and the sub-stable pattern in the bright blue frame as type II. The PTCDA sub-stable island I keeps growing from Fig. 4.15a to Fig. 4.15f shown from the increasing size of the white frames; the island II keeps becoming bigger from Fig. 4.15a to Fig. 4.15c, but from Fig. 4.15c to Fig. 4.15e this island gradually evolves to the type I pattern, which is illustrated by the blue islands gradually becoming smaller in images. As a result, the area of white islands keeps increasing during static scanning. Thus all type II patterned PTCDA molecules switch to the type I pattern in Fig. 4.15f, but the tip state changes in Fig. 4.15g, and the tip begins to remove this sub-stable pattern from the kinked boundary as shown in Fig. 4.15g. After four scanning cycles, we get the Fig. 4.15h with half of the island having been removed; after another two scanning cycles, all this sub-stable patterned island is removed by the tip in Fig. 4.15i. From this evolution process, we can see the type II sub-stable pattern is less stable than type I sub-stable pattern, which is the reason why the type I island can merge with the type II island. However, the type I state is not as stable as the normal herringbone pattern, and it is sensitive to different tip states, so once the tip state changes its island decays quickly. We are still looking for the mechanism for this dynamic decay process.

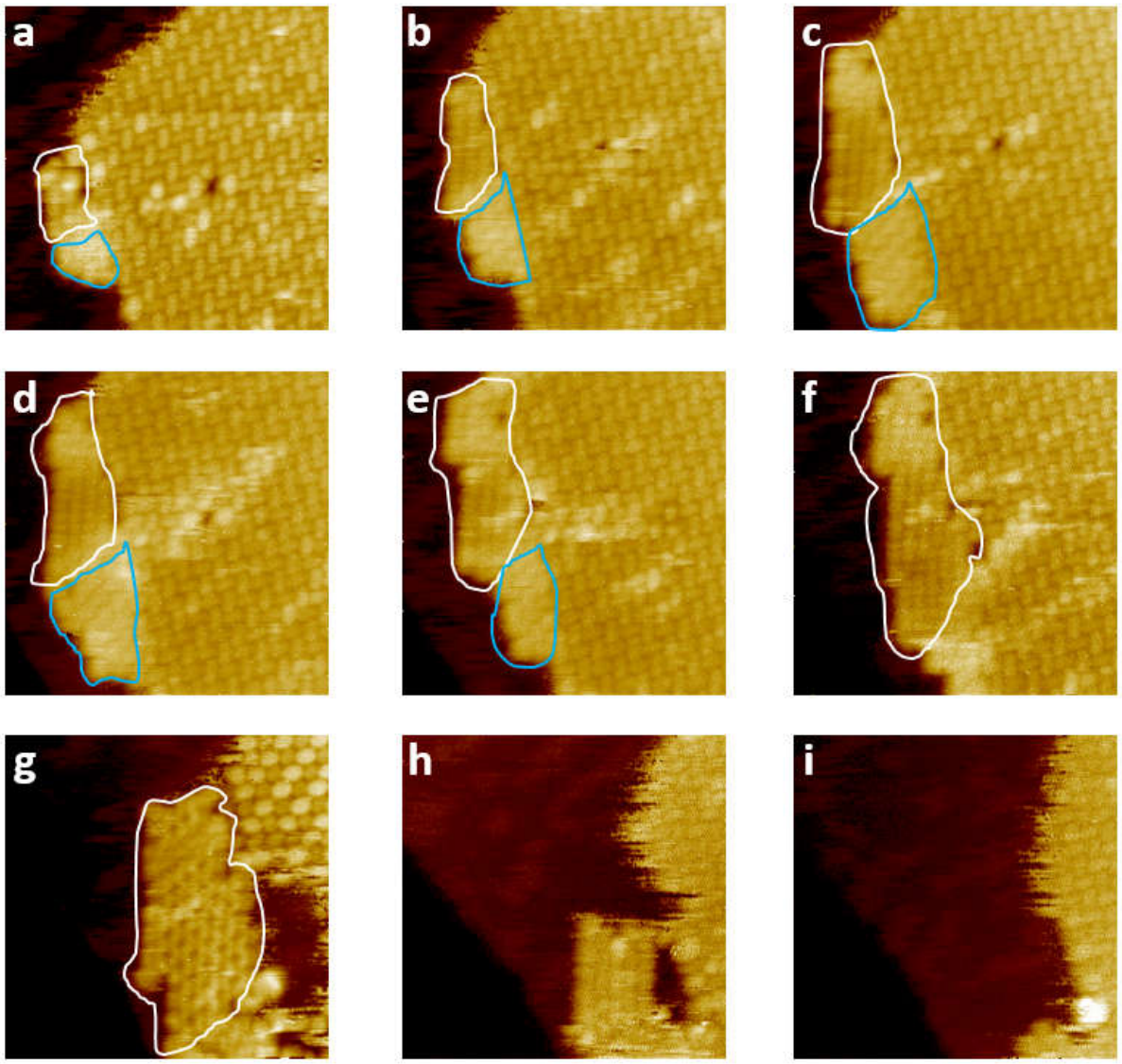

Fig. 4.15. STM images of a set of PTCDA decay data from self-assembled herringbone pattern to two sub-stable arrangements on type A flat graphene. (a-i) The typical decayed images from initial seed state to the final self-assembled herringbone pattern. All nine images have the same scanning conditions: V_s = -2.500 V, I = 0.030 nA, and the same scanning size as 23 nm × 23 nm. The white curved frames in images show the type I sub-stable arrangement, while the bright blue curved frames show the type II sub-stable arrangement.

4.4 Conclusion

In summary, we realized sub-monolayer C_{60} and PTCDA on quasi-1D and quasi-2D periodic wrinkled graphene by carefully controlling the deposition parameters of both molecules. We analyzed the differences between this suspended graphene wrinkles and graphene moiré pattern ripples, which provided us insights for further tuning molecular arrangement on flat and curved graphene. Our successful realization of acceptor-donor binary nanostructures on wrinkled graphene could have important implications in future development of organic solar cells.

Chapter 5. Step Edges in MoS_2 Few Layers and Pyramid Nanostructures

5.1 Introduction

TMDCs have attracted intensive research efforts due to their remarkable physical properties [156]. In the family of layered TMDCs, MoS_2 is a semiconductor, comprised of 2D S-Mo-S sandwich layers held together by van der Waals interactions as schematically shown in Fig. 1a [26]. Bulk MoS_2 has been extensively explored for decades as dry lubricants [27-29]. Recently, mono- to few-layered MoS_2 has captured increasing research attention across disciplines due to their optical, electronic, and catalytic properties [30, 33-42].

Particularly, as an atomically thin semiconductor, MoS_2 has a band gap that makes it a perfect complementary layered material to graphene for future ultrathin electronic and optical devices [35, 38, 157-160]. The monolayer form of MoS_2, due to the symmetry break, is a direct band gap semiconductor with a band gap of 1.90 eV, while bulk MoS_2 has an indirect band gap of 1.29 eV [33, 161, 162]. Monolayer MoS_2 can also be utilized to produce energy efficient field-effect transistors, photodetectors and flexible photoelectronic devices [9, 38, 156, 162, 163]. For any practical applications listed above, synthesis of high quality mono- or few-layered structures with large single-crystalline areas is required. It has been recently shown that synthesis of large films of polycrystalline monolayer and few-layered MoS_2 could be achieved using CVD [36, 164, 165]. Measurements of CVD grown monolayer MoS_2 have shown typical carrier mobility on the order of <10 cm^2 V^{-1} s^{-1}, much lower than mechanically exfoliated samples with typical mobility values of around 300 cm^2 V^{-1} s^{-1} and as high as 1090 cm^2 V^{-1} s^{-1} [166-169]. The difference is attributed to the grain boundaries and other structural defects induced during the growth process [170].

Compared with the transport and optical measurements on atomically thin MoS_2, little is known about the microscopic structures and associated electronic properties. It has been known that the grain boundaries in graphene and edges of graphene nanostructures, such as graphene nanoribbons and nanoplatelets, have significant influence on the electrical, thermal, optical and mechanical properties of 2D materials [170-173]. For example, grain boundaries have been shown to weaken the mechanical strength and reduce the charge mobility of graphene [172, 174, 175]. On the other hand, grain boundaries, edges, and other structural defects provide ample opportunities to tailor the local properties and create new functionalities, such as zigzag edges of

graphene nanoribbons which can host edge states and enhance optical excitations [176, 177]. For energy related applications, MoS_2 could potentially offer an earth abundant replacement to platinum as a catalyst and/or co-catalyst in the hydrogen evolution reaction (HER) as well as be used as a catalyst in the hydrogen desulfurization process [41, 178-181]. The edges of MoS_2 nanostructures are claimed to be closely related to the catalytic properties of MoS_2, such as the hydrodesulphurization reaction [182]. MoS_2 nanoparticles with greater exposure of sulfided edges are believed to be the next step towards producing more viable HER catalysts. Previous STM studies of MoS_2 as catalysts revealed that the edge sites as the catalytically active regions of the nanoparticles [182].

5.2 Experimental Methods

We examined CVD-grown MoS_2 mono- to few-layered nanoplatelets on HOPG and pyramid nanostructures on GaN and HOPG, respectively, by using STM and STS. MoS_2 mono- to few-layers nanoplatelets on HOPG were synthesized in a tube furnace using CVD techniques [183, 184]. Molybdenum chloride ($MoCl_5$) powder was placed at the center of a furnace while sulfur powder was placed upstream towards the entry to the furnace and the receiving HOPG substrate downstream. Conditions for MoS_2 mono- to few-layer growth are a temperature of 850 °C, a flow rate of 50 sccm, and a pressure of 2.0 Torr. The mono- to few-layered MoS_2 samples were transferred through air to the ultra-high vacuum preparation chamber of a customized Omicron STM system with a base pressure of low 10^{-10} Torr and annealed at 420 °C for 7 hours. The sample was then characterized in the STM chamber with a base pressure of low 10^{-11} Torr. The second sample we exanimated is a mono- to few-layered MoS_2 nanoplatelets on GaN. This sample was cleaned by annealing at an elevated temperature with the same procedure for cleaning the layered MoS_2 on HOPG samples. The third sample is a MoS_2 nanostructure with much higher density of edges, called MoS_2 nanopyramids on HOPG. These MoS_2 pyramid nanostructures were synthesized using CVD techniques as well. The same growth conditions were used for synthesizing the pyramid nanostructures as for MoS_2 mono- to few-layers, except that the pressure was kept at a higher 760 Torr [183, 184]. Before the STM measurement, the sample was annealed at 325 ˚C for 12 hours at a base pressure of low 4.8×10^{-10} Torr.

5.3 Results

In our STM experiments, we have observed that there are ripple structures near characteristic curved regions close to the MoS_2 edge terminals. These ripple structures have a typical height of 11.0 ± 3.5 Å and a width of 80.3 ± 20.4 Å. The STS measured on the curved regions reveals a band gap of 1.96 ± 0.10 eV, which is close to previous measured band gap of MoS_2 monolayers. On the basal plane, the measured band gap is 1.44 ± 0.12 eV. The difference in band gap on the curved regions and basal planes can be attributed to the decoupling between layers on the rippled regions near the edge terminals.

5.3.1 Layered MoS_2 Nanoplatelets on HOPG

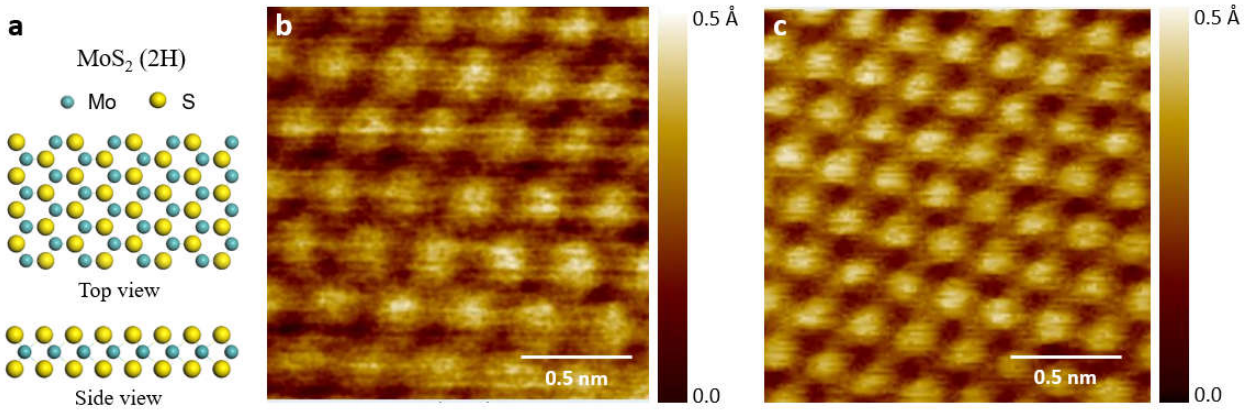

Fig. 5.1. (a) Ball model of MoS_2. (b) Constant current STM image of MoS_2 (V_s = − 1.35 V, I = 1.20 nA). (c) Constant current STM image of HOPG (V_s = −1.50 V, I = 0.80 nA).

MoS_2 mono- to few-layers nanoplatelets on HOPG were synthesized using CVD techniques. The synthesis procedure details were described in our previous experimental sections. This sample showed large area coverage of mono- to few-layers with little edge exposure. Fig. 5.1b is a constant current STM image of MoS_2 monolayer on HOPG, showing a measured lattice constant of 3.1 ± 0.1 Å. As a comparison, Fig. 5.1c is an atomic resolution image of the HOPG substrate.

5.3.2 Layered MoS_2 Nanoplatelets on GaN

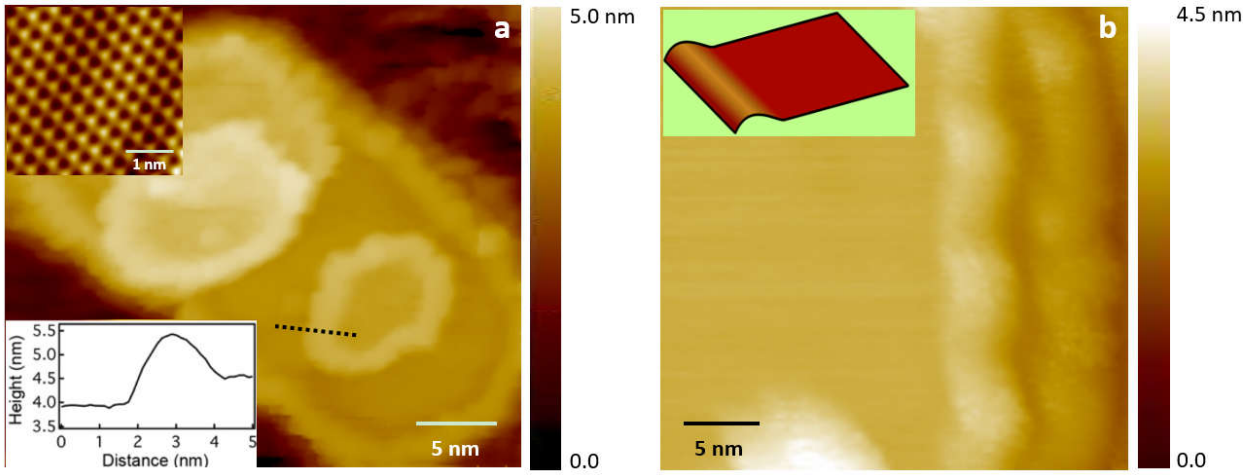

Fig. 5.2. Constant current STM images of few-layered MoS_2 on GaN. (a) A MoS_2 island on top of a larger MoS_2 island with curved edges (V_s = − 2.15 V, I = 0.20 nA). The upper left inset shows an atomic resolution image of the few-layered MoS2 (V_s = − 1.70 V, I = 0.90 nA). The lower left inset is a line profile along the line as marked with the dashed black line. (b) A zoomed-in image of curved MoS_2 edges. The upper left inset is a schematic of a curved edge (V_s = − 2.00 V, I = 0.42 nA).

To investigate the edges of MoS_2 few layers, we exanimated mono- to few-layered MoS_2 nanoplatelets on GaN with high edge exposure and density of edges, as shown in Fig. 5.2. The inset in Fig. 5.2a is an atomic resolution image of MoS_2 on these nanoplatelets. The typical size of these nanoplatelets varies from a few to tens nanometers. An intriguing feature is there is a curved region near the edges, shown as the bright protrusion in Fig. 5.2a and 5.2b. And a line profile in Fig. 5.2a clearly shows this curved feature. The average height of the curving edges of MoS_2 on the GaN substrate is 11.62 ± 4.0 Å while the average width is 40.3 ± 14.2 Å, calculated from 35 different locations on monolayer edges over 9 different scan areas. To interpret the curving edge feature, firstly we are able to confirm that the observed curving parts are a topographic structure, because the measured height is way higher than the height different due to local electronic density that is typically less than one angstrom. For example, Lauritsen et al observed a local protrusion features with a height of 0.4 Å in triangular nanoclusters on Au(111), which were attributed to the metallic properties of the MoS_2 edge sites [182].

5.3.3 MoS_2 Pyramid Nanostructures on HOPG

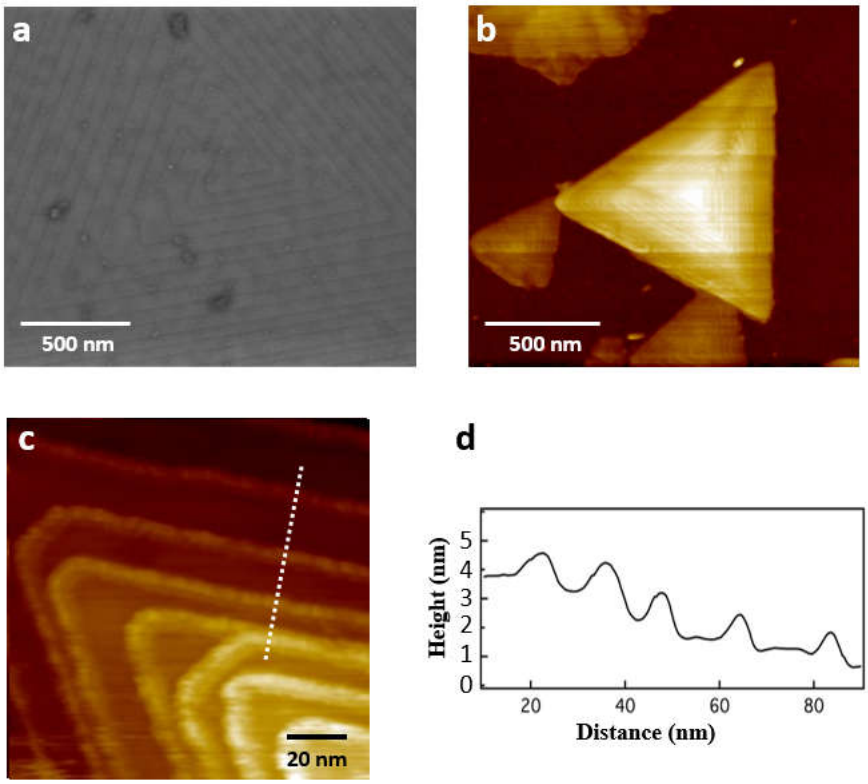

Fig. 5.3. (a) SEM and (b) AFM images of MoS_2 nanopyramids. (c) Constant current STM image of a MoS_2 nanopyramid ($V_s = -1.55$ V, I = 0.20 nA) (d) Line profile from (c) shows cross section over six layers. Monolayer thickness is determined to be 6.3 Å, and the curved regions near edge terminals are shown as bumps in the line profile.

We further examined a MoS_2 pyramid nanostructures on HOPG with much higher density of edges. Fig. 5.3 shows scanning electron microscopy (SEM), AFM, and STM images of the MoS_2 nanopyramids. In both large-scale SEM and AFM images (Figs. 5.3a and 5.3b), a spiraling structure terminating at the top can be clearly seen, indicating spiral driven growth of these nanopyramids. The nanopryamids range in size from 2-8 μm side edges and 40-120 nm in height. One intriguing feature of the pyramid platelets is that they all have a consistent ratio between their height and lateral length. This ratio, along with the fact that all of the nanoparticles regardless of size are complete pyramids, suggests that the pyramids are not likely deposited layer by layer. Instead, they grow out in all three dimensions around an initial starting point. A fairly constant

growth rate under these circumstances would lead to complete pyramids with similar three dimensional proportions, regardless of their size. In Fig. 5.3a, on the top of the MoS_2 pyramid, a spiral structure can be observed. This growth pattern could also help explain the spiraling shape of the pyramids observed by AFM, STM, and SEM. The average hillock slope of the pyramids from AFM measurements was 0.03 ± 0.01, but ranged from 0.02 to 0.06. The average Hillock slope for the pyramid observed in this STM study was 0.06 ± 0.01. The monolayer height is 6.3 ± 0.2 Å and the average terrace width is 11.0 ± 0.3 nm as calculated from the Hillock slope and the measured monolayer height from the STM studies.

5.4 Discussion

From higher resolution STM image of the MoS_2 nanopyramids, as shown in Fig. 5.3c, a prominent feature observed in the MoS_2 nanopyramids is the curving region near the edge terminals, similar to the curved regions near edge terminals observed in few-layered MoS_2 nanoplatelets on GaN substrates in Fig. 5.2. The curving parts appear to be a result of the monolayer curving down and allowing the edge terminal to interact with the lower layer with a small contacting angle. For MoS_2 nanopyramids, if the edge curving features are a result of the monolayer folding down and reducing edge exposure, this could partially explain the poor performance of the nanoparticles in the HER [184]. The edge termination could help explain why this interaction with the underlying layer occurs. There are two types of edges that can occur, S edges and Mo edges. In hexagonal shaped MoS_2 monolayers, both occur alternating around the perimeter. In triangular shaped monolayers, one or the other is the edge termination. S edges have been shown to interact more strongly with supporting substrates than Mo edges on Au(111) and graphene [185]. The corners of the monolayers indicate that both terminations may be equally likely to interact with the supporting layer beneath. While most of the corners terminate at a 60° point, there are still many that have more of a hexagonal, flattened end. These flattened points have different edge terminations than the two edges leading up to it, but still show the same curving edges with the same proportions.

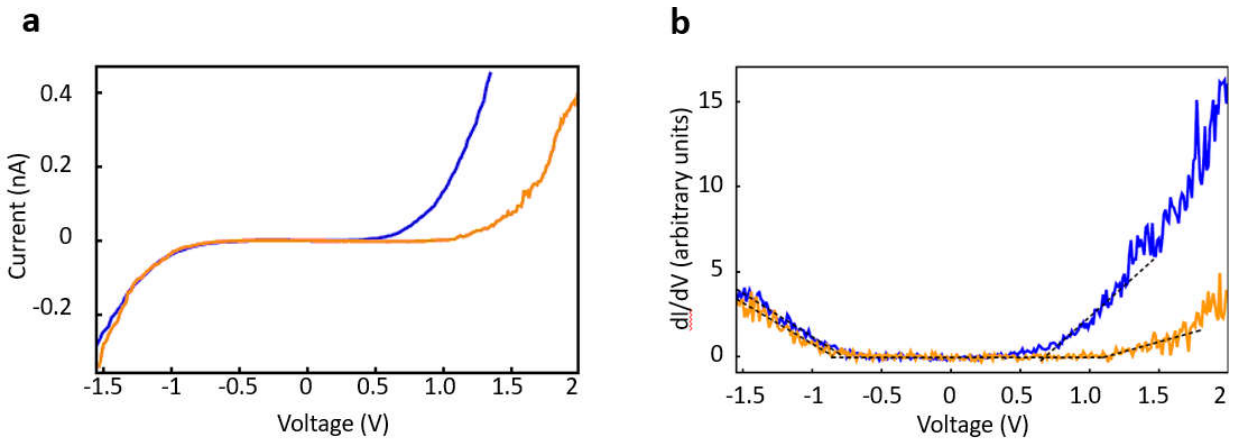

Fig. 5.4. (a) I-V and (b) dI/dV spectra taken on the basal planes of the MoS_2 pyramid terrace (blue) and near the curved regions of the MoS_2 pyramid terraces (yellow) ($V_s = -1.55$ V, I = 0.30 nA, $V_{wigg} = 20$ mV, f = 1 kHz).

Scanning tunneling spectroscopies from the basal planes and the curving regions are shown in Fig. 5.4. In the average dI/dV curves (Fig. 5.4b), we linearly fitted lines to the sloped parts that correspond to the valence band and the conduction band. The band gap is estimated by extrapolating these linear lines to their crossings with the minimum conductance and finding the separation between the two intersections. The spectroscopies on the basal planes of the MoS_2 terraces show a band gap that agrees with the band gap of bulk MoS_2 of 1.44 ± 0.12 eV, as shown the blue line in Fig. 5.4a. However, spectroscopies on the curving part near the corners of the pyramids show a band gap with a value of 1.96 ± 0.10 eV, as shown the yellow line in Fig. 5.4a, consistent with monolayer MoS_2 [33, 162, 186]. Yet, previous STS measurements of the monolayer MoS_2 band gap on graphite measured at 77 K show that monolayer MoS_2 has an energy gap of 2.15 ± 0.06 eV and an exciton binding energy of 0.22 ± 0.1 eV [157]. The discrepancy in band gap is a result of different interactions between the underlying terrace and the curving parts near the edge terminals or terrace basal planes with the layer above. On the basal terrace plane, the layer interaction with lower layers is the same as bulk MoS_2. In conclusion, it appears that there is decoupling around the edges and corners that causes the electronic properties more like its monolayer form.

Spectroscopies from around the edges show somewhat of an intermediate band gap between the corners and the terrace plane. The size of the band gap is sensitive to the distance from the edge whereas the spectroscopies taken from around the corners show less deviation with distance

from the corner and therefore have a much larger effective area to sample from. This is likely a result of greater decoupling at the corners where two edges meet.

5.5 Conclusion

In summary, we have observed an intriguing ripple feature near the edge terminals in MoS_2 few-layered nanoplatelets and pyramid nanostructures. Based on STM images, these ripple features are curved structural segments. Our STS data on these ripple structures show a band gap of 1.96 ± 0.10 eV, near the band gap of monolayer MoS_2. The geometrical and electronic properties likely contribute to the catalytic efficiency of MoS_2 nanostructures, and would potentially provide opportunities for unprecedented applications of atomically thin MoS_2 layers and MoS_2 nanostructures.

Chapter 6. Membrane Trafficking Studies by AFM

6.1 Introduction

In eukaryotic cells, vesicular ubiquitinated cargo is the initial product for the degradation. Toll interacting protein (Tollip) and Target of Myb protein 1 (Tom1) are adaptor proteins that participate in endosomal cargo trafficking [2,187]. In human bodies, as an inhibitory adaptor protein, Tollip is encoded by the Tollip gene [188-190]. Tollip, containing an N-terminal Tom1 binding domain (TBD), a central conserved 2 (C2) domain, and a CUE domain, is an inhibitory adaptor protein in Toll-like receptors (TLR) signaling pathway which is an important part of the innate immune system of humans [189, 190]. In the innate immune system of humans, the TLR pathway is important for structurally recognizing any conserved molecular patterns of microbial pathogens and helping to build a responding inflammatory immune response. Tom1 is another protein involved in membrane trafficking and protein degradation in human bodies. It contains an N-terminal VHS domain followed by a central GAT domain, and similar to Tollip protein, it is encoded by the TOM1 gene.

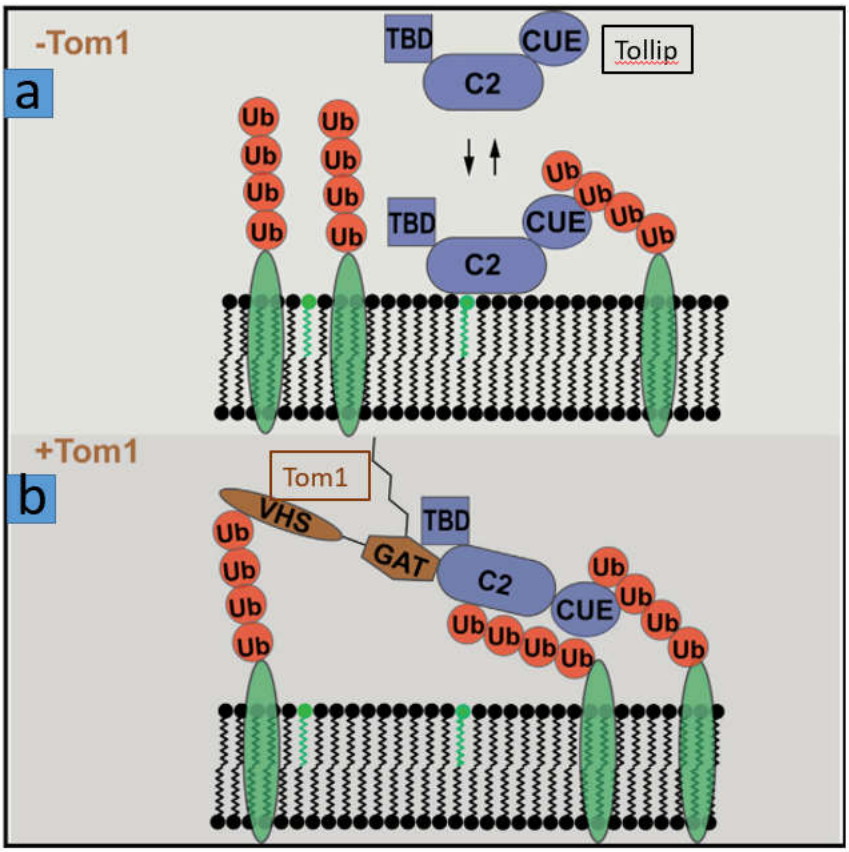

Fig.6.1. Model of Tollip association with/without Tom1 at the surface of early endosomes. (a) Model of Tollip association without Tom1 at the surface of early endosomes, in which Tollip is initially associated with PI(3)P (the green lipid in the membrane) and the ubiquitinated cargo proteins on the endosome. (b) Model of Tollip association with Tom1 at the surface of early endosomes, which is required for receptor degradation, in which Tom1 interactions with Tollip induces the unfolded TBD domain of Tollip to fold, and then this folding modulates binding of Tollip to PI(3)P lipid [2].

The contrast model aims to explain the role of Tom1 in the endosomal cargo trafficking process shown in Fig. 6.1 [2]. As shown in Fig. 6.1a, initially, Tollip is located on the endosome membrane via association with PI(3)P. When the ubiquitinated cargo protein is transported to the endosome, adaptor protein Tom1 can be recruited (Fig. 6.1b). Then, the N-terminal TBD of Tollip is induced from its initial unfolding state to folding state through binding to Tom1. This folding can mediate the dissociation of Tollip from PI(3)P lipid and participate in cargo trafficking with Tom1. However, this theoretical model proposed by Xiao et al. through the nuclear magnetic resonance analysis, HeLa cells experiment, and SPR measurement still needs to be demonstrated by some more visualization tools [2]. AFM is a powerful microscope with excellent resolution as high as 10^{-9} m that can be used in liquid and has already been widely applied in exploring biological properties on living or model biological systems [3, 191-194]. Therefore, AFM is applied in this study to "observe" how this Tollip can specifically associate on PI(3)P lipid.

6.2 Introduction of AFM and Liquid Mode

As one of the highest resolution microscopes, AFM can scan a variety of specimens, with good resolution on the order of 10^{-9}m, 1000 times higher than the optical microscope. The core part of AFM is a sharp probe at the end of a cantilever which can directly scan the measured surface. Because it can probe the surface on both conductors and insulators, it is widely used across disciplines. Additionally, the scanning efficiency of the AFM overall is much higher than that of STM due to the ease of changing a new AFM tip compared to the time consuming process of replacing a tip for STM scanner. Another convenience is that AFM does not need the UHV environment. Thus AFM is a fast probe instrument in labs and companies. It is a good supplement

for STM in our lab. We usually do a quick look at our new sample first with AFM, especially when its overall morphology is not so clear.

The most common scanning environment of AFM is in air, but when the specimen is a biological sample that must be kept in solution environment we have to use the liquid mode to detect it.

Fig. 6.2. Photos of Bruker Dimension Icon AFM and its scanning head.

Fig.6.2a is Bruker Dimension Icon AFM. It mainly contains scanning head, sample stage, controller and display. Scanning head is the core component shown in Fig. 6.2b. There is no scanning tip on the scanning head now. The four golden pins at its bottom side is the position where we need to amount AFM tip. After the installment of a suitable AFM tip with the liquid cell (Fig. 6.3a), liquid cell cover is always required in liquid mode. In Fig. 6.3b, it shows the ready-to-scan scanning head with a scanning tip protected by a white liquid cell cover. The reason why a liquid cell cover is compelling at the end of the scanning head is that it can always isolate the scanning head from the liquid that the scanning tip needs to touch. Otherwise, liquid may flow into the liquid cell when the scanning tip is immersed in the liquid, which will damage the scanning head.

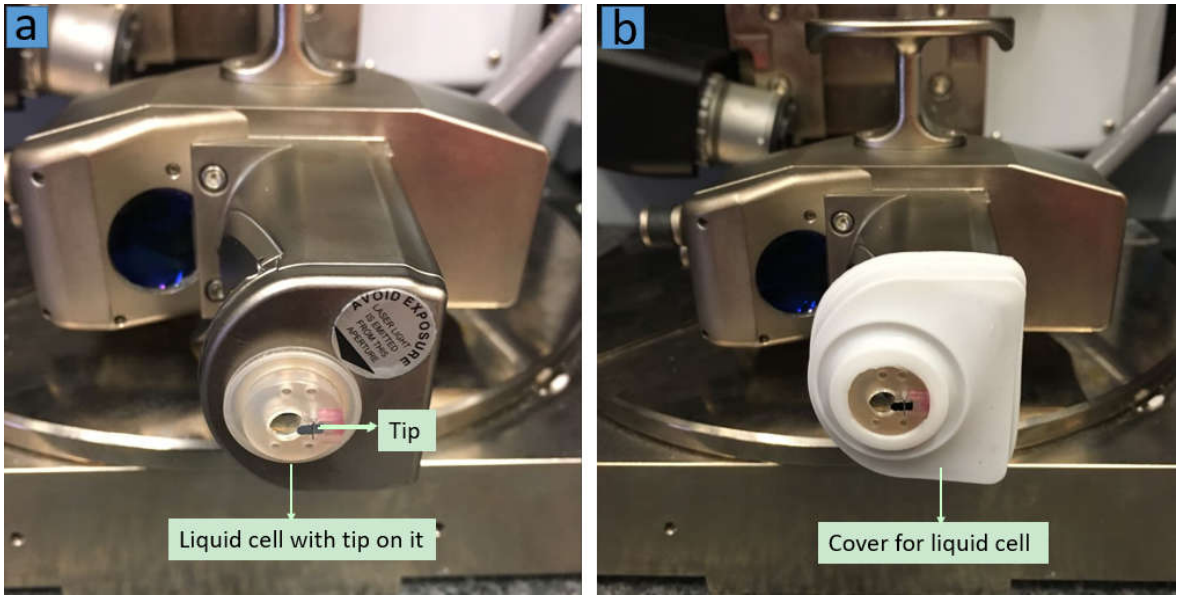

Fig. 6.3. Photos of AFM tip, liquid cell and cover mounted in scanning head. (a) A tip is mounted in the liquid cell first, then the whole cell is plugged into the golden pins. The white plastic cover in (b) is for protecting scanning head.

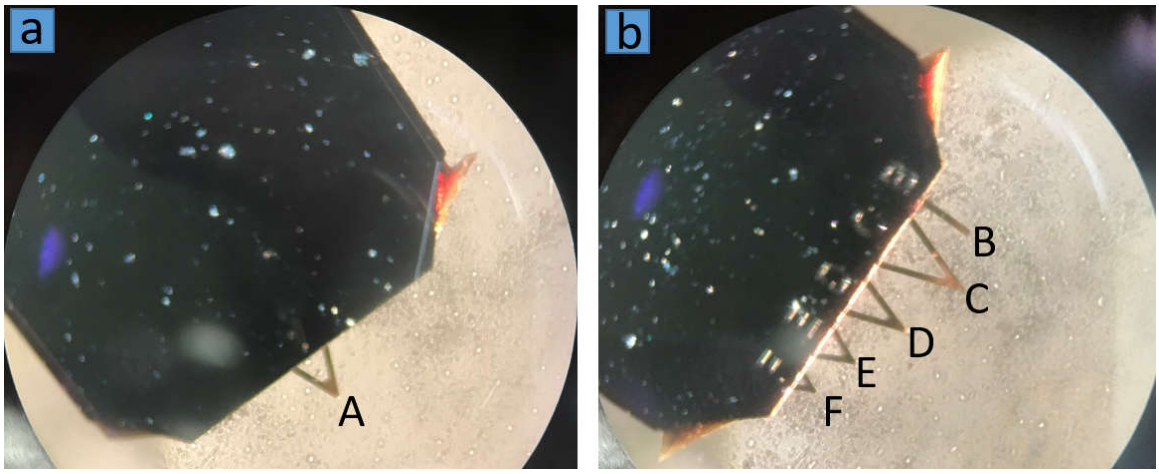

Fig. 6.4. Optical microscope images of all the six tips in one MSCT model AFM tip. (a) One tip on one side. (b) Five different tips on the other side.

The model for our AFM is Dimension Icon from Bruker Company. The tip we are using is the MSCT model from Bruker, a tiny micro lever AFM probe having soft silicon nitride cantilevers with sharpened silicon nitride tips, ideal for all modes in liquid operation. MSCT model is a complicated one with six different tips at two ends shown in Fig. 6.4. There is only one triangular

tip A on one side of this MSCT model, while five tips labeled from B to F on the other side. All these six tips have different tip sizes and different spring constants. In order to get the most stable AFM images and not to damage the soft sample surface, all our measurements are done with tip C, the softest tip with the spring constant as 0.01 N/m, and the size as 310µm L × 20µm W. In all our measurements, we use the tapping mode in liquid.

The difficult part for the liquid mode is how to focus the laser on the end of the C tip. The focal point will change from air to solution due to the diffraction effect, so it is a little more complicated than the focusing process in air mode. There are two typical methods for focusing, but we usually use the basic one because it is easier. Firstly, we need to focus the laser in the air, and approach the tip close to the sample so that we can clearly see the optical microscope image of it; then add water to both the sample and the tip side (avoid bubbles in the tip side); adjust the position of tip mildly. When the reflected signal from the tip end is the maximum value, the focusing process is finished. Besides the challenge of the laser focusing in liquid, tuning the driving frequency and the amplitude of the cantilever is also difficult. Because the auto tune does not work in the liquid mode, we need to manually tune the frequency and amplitude through fast thermal tune method.

6.3 Protein Measurement under AFM Liquid Mode

6.3.1 Morphology of Pure Mica

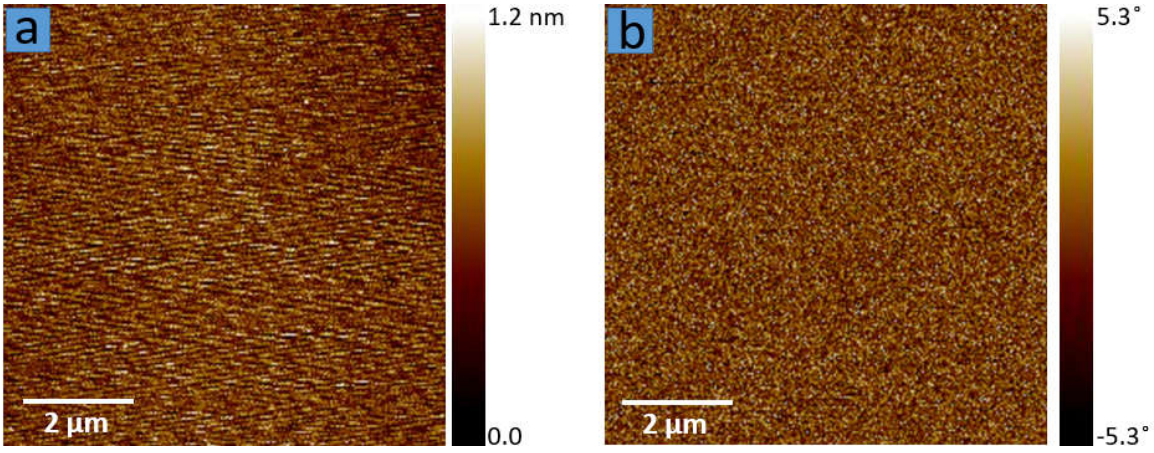

Fig. 6.5. AFM images of bare mica substrate. (a) The height image and (b) the phase image.

We choose mica as our substrate, and grade V1 mica is purchased from TED PELLA, INC. The mica substrate needs to be newly cleaved by scotch tape before each experiment in order to keep the whole sample system clean. The fresh mica substrate is really flat even in the scanning range of 10 μm × 10 μm, just as shown in Fig. 6.5.

6.3.2 Morphology of Lipid on Mica

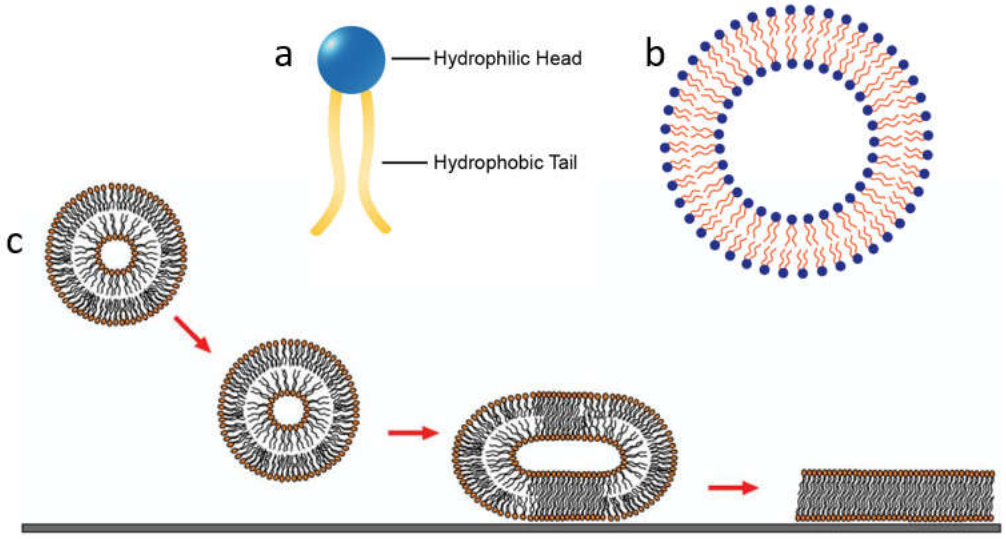

Fig. 6.6. The method commonly used for preparing SLBs for AFM analysis-fusion of lipid vesicles. (a) The schematic drawing for lipid, including the hydrophilic head and the hydrophobic tail. (b) Representative structure of liposome. (c) The schematic diagram for the formation of the SLBs on top of mica [3].

In order to study the protein-lipid association, the suspended lipid bilayers (SLBs) are applied to mimic a membrane environment. SLBs need to be prepared from lipid solution. As a background, each lipid has a hydrophilic head and a hydrophobic tail, as shown in Fig. 6.6a. In chemistry, hydrophilic means a molecule or other molecular entity that is attracted to water molecules and tends to be dissolved by water. Hydrophobic means the physical property of a molecule (known as a hydrophobe) that is seemingly repelled from a mass of water. Therefore, lipids will automatically form a liposome structure (Fig. 6.6b) in a water environment. A liposome is a spherical vesicle having at least one lipid bilayer, which can be used as a vehicle for administration of nutrients and pharmaceutical drugs. Fig. 6.6c shows the whole process from the liposome to

SLBs on top of mica: drop the fresh lipid solution from a dropper onto the fresh mica surface, then incubate the liposome on top of mica above the transition temperature for 10 to 15 minutes. The liposome will form plane SLBs by itself on mica surface shown like the right down final image in Fig. 6.6c. In this study, different lipids 1,2-Dioleoyl-sn-glycero-3-phosphocholine (DOPC) and PI(3)P [1 mM, DOPC: PI(3)P in a 97: 3 M ratio] are dissolved in an organic solvent (methanol: chloroform: H_2O = 2:1:0.8). Once the lipid solution turns clear, the solvent is removed under a gentle nitrogen stream to yield a lipid film. The vial is placed in a vacuum chamber for overnight to get rid of all the residual organic solvent. The formed lipid films are hydrated by adding a preheated HEPES-buffered saline (HBS; 100 mM NaCl, 20 mM HEPES, 10 mM $MgCl_2$, pH 7.4) above the transition temperature of the lipids. After vortex, the mixture can form different types of liposomes, which include small unilamellar vesicles (SUV), large unilamellar vesicles (LUV), MLV, and multivesicular vesicles (MVL), as shown in Fig. 6.7. In order to get homogeneous SUV, a probe tip sonication is used to disrupt MLVs and MVLs into SUV. After sonication, the diameter of vesicles is between 70 nm and 150 nm.

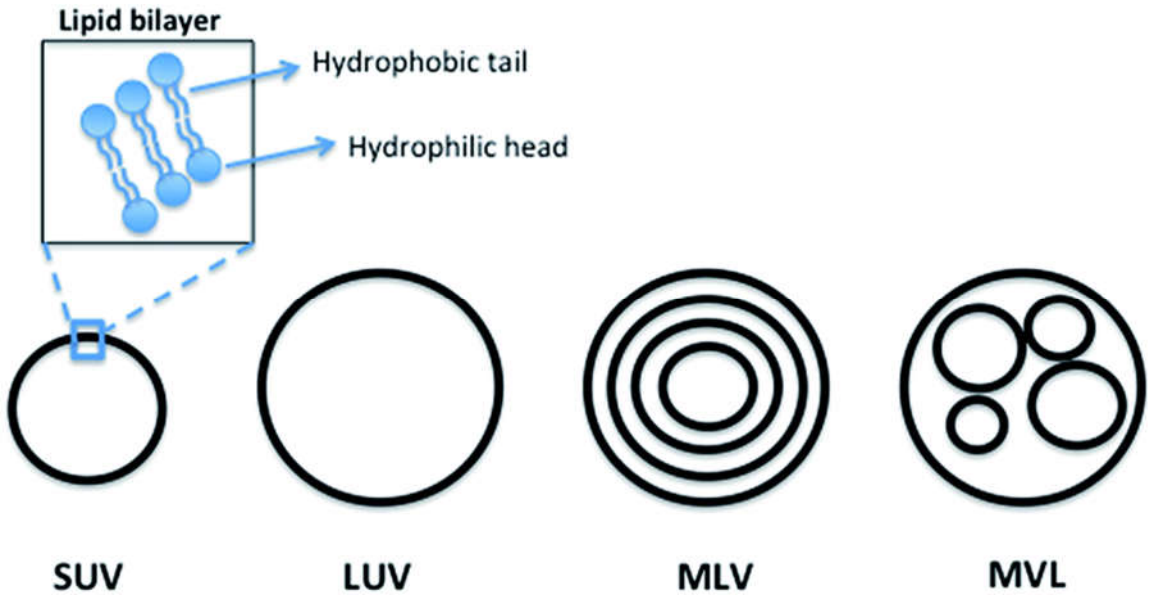

Fig. 6.7. Schematic drawing for different types of vesicles formed in solution. SUV, small unilamellar vesicles; LUV, large unilamellar vesicles; MLV, multilamellar vesicle; MVL, multivesicular lamella [4].

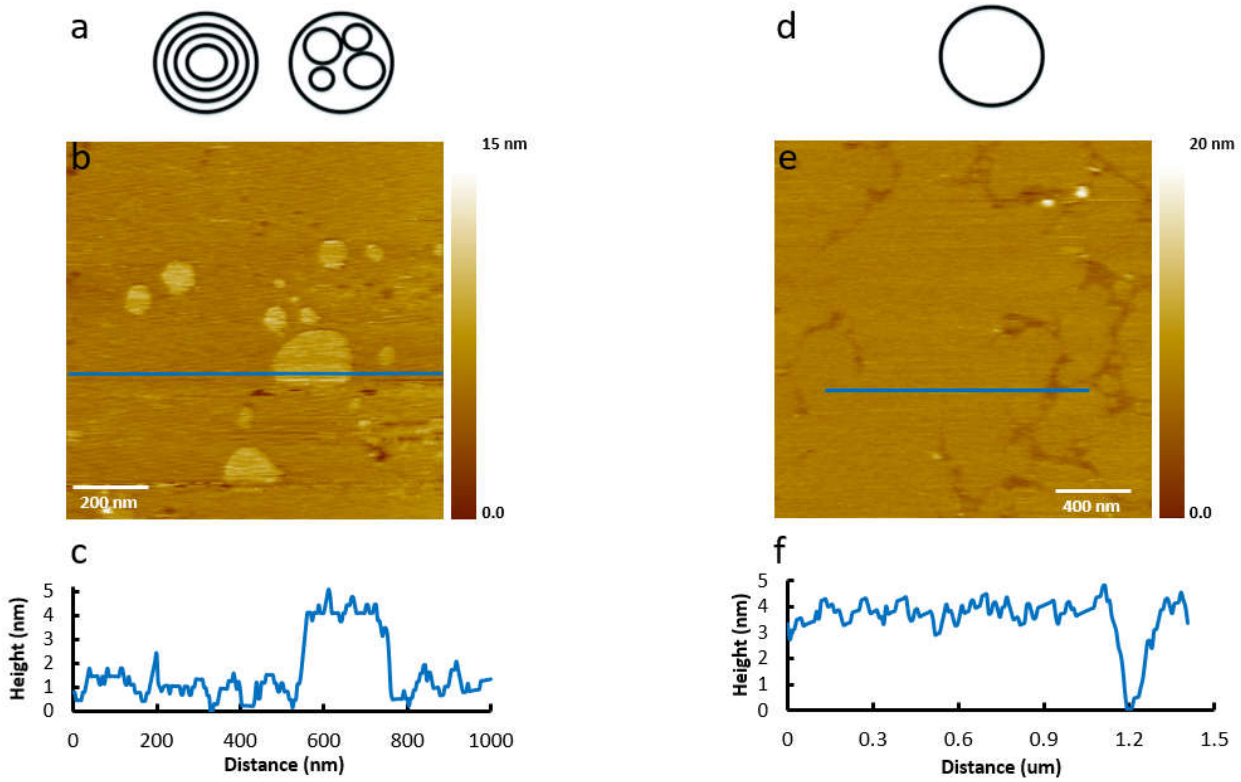

Fig. 6.8. AFM images of SLBs on mica and the corresponding types of vesicles. (a) Schematic drawing of the MLV and MVL. (b) Representative AFM image of SLBs formed by liposomes without sonication treatment. (c) The typical step height of SLB measured from the second SLB to the first SLB along the blue line in (b). (d) The model of SUV or LUV. (e) Representative AFM image of SLBs formed by liposomes with sonication treatment. (f) The step height of SLB from the mica substrate.

AFM images of SLBs show the existence and coexistence of these several types of liposomes, as in Fig. 6.8. The topography of SLBs in Figs. 6.8b and 6.8e is recorded using the tapping mode of AFM. For Fig. 6.8b, there are about 1.2 SLBs on top of mica, and almost no bare mica left, the light yellow circular SLB is the second layer on top of the first SLB. This kind of circular toppings are formed due to these two types of vesicles-MLV and MVL. The step height of it is 2.8 nm ± 0.2 nm in Fig. 6.8c, consistent with the height of lipid bilayer. There are several curved dark lines in Fig. 6.8e, which are the bare mica surface, but the majority area is the lipid bilayer. The line profile in Fig. 6.8f along the blue line marked in the image shows the height of the SLB on mica, consistent with the theoretical height of it.

6.3.3 Morphology of Protein on Lipid

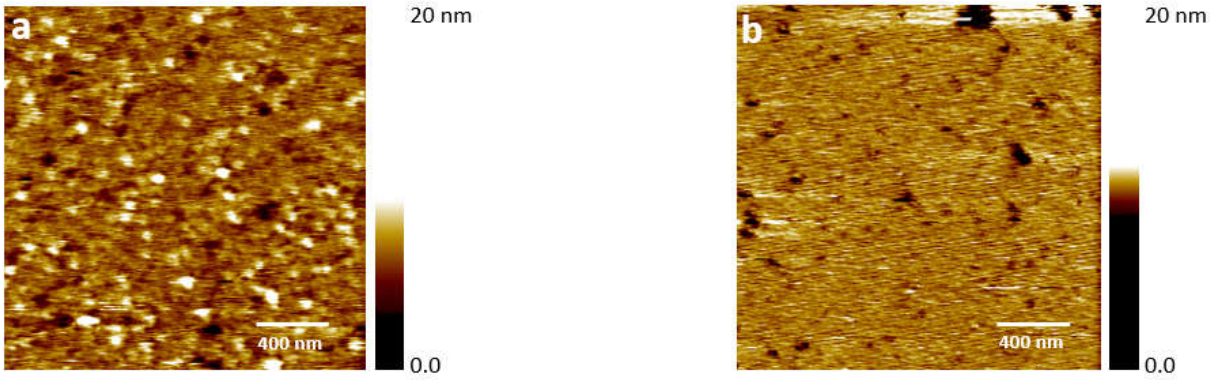

Fig. 6.9. AFM images of Tollip binding PI(3)P on SLBs. Both topographies are recorded using the tapping mode of AFM, and obtained in HEPES-buffered saline (HBS; 100 mM NaCl, 20 mM HEPES, 10 mM $MgCl_2$, pH 7.4). (a) Representative AFM image of SLB assembled using liposomes with PI(3)P pre-incubated with Tollip. The bright dots show the PI(3)P liposomes with Tollip clusters. (b) Representative AFM image of SLB assembled using liposomes without PI(3)P pre-incubated with Tollip. The earthy yellow area stands for the bare SLB, and the dark dots show the bare mica.

As we predicted from the introduction part, Tollip is assembled on the SLBs membrane via association with PI(3)P, shown in Fig. 6.9a. The bright dots show the PI(3)P liposomes with Tollip clusters. The dark yellow area shows the bare SLB. In order to demonstrate our prediction, we prepared another check experiment: it is similar to the original one except the choice of lipid, where we only add DOPC lipid, without PI(3)P in preparation for lipid solution. The check result shown in Fig. 6.9b is obviously different from the assembled clusters with PI(3)P lipid, because there is no Tollip on top of the SLB, which, however, are observed as bright dots in Fig. 6.9a. This set of check experiments successfully demonstrate that Tollip is located on the endosome membrane via association with PI(3)P. This specific association is the first step we need to demonstrate, which gives us a good start.

6.4 Discussion

From the aforementioned experiments, we successfully demonstrate that the Tollip can be located on the endosome membrane via association with PI(3)P, and the AFM can be properly used in the protein-lipid study. For the future study, we will further illustrate the formation of Tollip-Tom1 complex on the endosome membrane and the association with ubiqitinated cargo proteins.

6.5 Conclusion

We successfully demonstrate that the adaptor protein Tollip is specifically associated with the endosome membrane through PI(3)P, which is an important initial step for exploring this folding theoretical model. And liquid mode of AFM is a perfect technique to detect this kind of soft and tiny nanostructures, so AFM will be further applied in this study.

Chapter 7. Conclusion and Outlook

The experiments in this dissertation focus on organic solar cells taking advantages of 2D materials. 2D materials, such as graphene and atomically-thin TMDCs, provide options for building economic, safe, mechanically flexible solar cells with adjustable sunlight absorption and desirable optical/electronic properties. C_{60}, as the common used material in organic solar cells, especially with the combination of graphene for flexible transparent electrodes, is promising candidates for building future solar cells. In our experiments, novel C_{60} 1D structures were realized on rippled graphene. The width of 1D pattern is controlled by the annealing temperature, with a range from single C_{60} to three C_{60} molecules, and then to a quasi-hexagonal close packed 1D stripe structure. Besides the 1D C_{60} structures, quasi-hexagonal close packed 1D C_{60} structures on quasi-1D or quasi-2D wrinkled graphene are observed in our second experiment. We explored the mechanism why C_{60} forms various nanostructures on graphene moiré pattern ripples and the suspended graphene wrinkles, and calculated the binding energies for different configurations, which would provide us critical information for further tuning molecular arrangement on different types of graphene. PTCDA, a good electron acceptor, can be utilized in the active layer by combing with C_{60} for organic solar cells. We realized sub-monolayer C_{60} and PTCDA on quasi-1D and quasi-2D real periodic wrinkled graphene, by carefully controlling the deposition parameters of both molecules. Based on the subtle balance between the intermolecular and the molecule-substrate interactions, as well as the different kinds of the ripples due to the moiré patterns or suspended structures, we expect that we will be able to further tune and control the 1D C_{60} molecule structures on 1D graphene by varying the types of the ripples, the coverage of adsorbed C_{60} and PTCDA molecules, and the temperature. Other combinations for organic solar cells can also be explored in the future, for example, C_{60}/ Boron subphthalocyanine chloride (SubPc) bulk heterojunctions. Our results pave a way for optimizing bulk heterojunctions with a combination of emerging 2D materials for organic solar cells in the future. We also performed SPM measurements on one of atomically thin TMDCs, the mono- to few-layered MoS_2, which has potential applications as active layer in solar cells. In addition to applications in solar cells, our study on MoS_2 atomically thin nanostructures are also important in in photovoltaics, electronics and quantum information.

In the final chapter of this thesis, we used liquid-cell AFM to verify that the adaptor protein Tollip on biological membranes (a very different type of 2D materials) is associated with the endosome membrane through PI(3)P in the proposed membrane trafficking process. In order to understand this series of actions in more details, other works still need to be investigated in the future, for example, the formation of the Tollip-Tom1 complex on SLBs, the morphology of different lipid compositions of membrane, and the impact of polyubiquitin chain topology on membrane trafficking process.

References:

[1] C.H. Chen, H.S. Zheng, A. Mills, J.R. Heflin, C.G. Tao, Temperature Evolution of Quasi-One-Dimensional C60 Nanostructures on Rippled Graphene, Scientific Reports, 5 (2015) 14336.

[2] S.Y. Xiao, M.K. Brannon, X.L. Zhao, K.I. Fread, J.F. Ellena, J.H. Bushweller, C.V. Finkielstein, G.S. Armstrong, D.G.S. Capelluto, Tom1 Modulates Binding of Tollip to Phosphatidylinositol 3-Phosphate via a Coupled Folding and Binding Mechanism, Structure, 23 (2015) 1910-1920.

[3] M.P. Mingeot-Leclercq, M. Deleu, R. Brasseur, Y.F. Dufrene, Atomic Force Microscopy of Supported Lipid Bilayers, Nature Protocols, 3 (2008) 1654-1659.

[4] M. Salim, H. Minamikawa, A. Sugimura, R. Hashim, Amphiphilic Designer Nano-Carriers for Controlled Release: from Drug Delivery to Diagnostics, Medicinal Chemical Communications, 5 (2014) 1602-1618.

[5] D. Jariwala, T. Marks, M. Hersam, As Thin as It Gets, Nature Materials, 16 (2017) 155-155.

[6] Y. Chen, H.Q. Sun, W.C. Peng, 2D Transition Metal Dichalcogenides and Graphene-Based Ternary Composites for Photocatalytic Hydrogen Evolution and Pollutants Degradation, Nanomaterials, 7 (2017) 62.

[7] Z.B. Li, S.L. Wong, Functionalization of 2D Transition Metal Dichalcogenides for Biomedical Applications, Materials Science and Engineering:C, 70 (2017) 1095-1106.

[8] C. Pierluigi, G. Matteo, R. Angel, Local-Field Effects on the Plasmon Dispersion of Two-Dimensional Transition Metal Dichalcogenides, New Journal of Physics, 15 (2013) 125005.

[9] B. Radisavljevic, A. Kis, Mobility Engineering and a Metal-Insulator Transition in Monolayer MoS2, Nature Materials, 12 (2013) 815-820.

[10] D.J. Rahn, E. Ludwig, J. Buck, F. Kronast, M. Marczynski-Buhlow, E. Kroger, L. Kipp, K. Rossnagel, Laterally Confined Metal-to-insulator and Quasi-Two-Dimensional-to-Two-Dimensional Transition by Focused Rb Intercalation of 1T-TaS2, Physical Review B, 84 (2011) 233105.

[11] H. Wang, L.L. Yu, Y.H. Lee, Y.M. Shi, A. Hsu, M.L. Chin, L.J. Li, M. Dubey, J. Kong, T. Palacios, Integrated Circuits Based on Bilayer MoS2 Transistors, Nano Letters, 12 (2012) 4674-4680.

[12] X.Y. Yu, A. Rahmanudin, X.A. Jeanbourquin, D. Tsokkou, N. Guijarro, N. Banerji, K. Sivula, Hybrid Heterojunctions of Solution-Processed Semiconducting 2D Transition Metal Dichalcogenides, ACS Energy Letters, 2 (2017) 524-531.
[13] T. Yun, J.S. Kim, J. Shim, D.S. Choi, K.E. Lee, S.H. Koo, I. Kim, H.J. Jung, H.W. Yoo, H.T. Jung, S.O. Kim, Ultrafast Interfacial Self-Assembly of 2D Transition Metal Dichalcogenides Monolayer Films and Their Vertical and In-Plane Heterostructures, ACS Applied Materials & Interfaces, 9 (2017) 1021-1028.
[14] K.S. Novoselov, A.K. Geim, S.V. Morozov, D. Jiang, Y. Zhang, S.V. Dubonos, I.V. Grigorieva, A.A. Firsov, Electric Field Effect in Atomically Thin Carbon Films, Science, 306 (2004) 666-669.
[15] A.H. Castro Neto, F. Guinea, N.M.R. Peres, K.S. Novoselov, A.K. Geim, The Electronic Properties of Graphene, Reviews of Modern Physics, 81 (2009) 109-162.
[16] A.K. Geim, K.S. Novoselov, The Rise of Graphene, Nature Materials, 6 (2007) 183-191.
[17] X.S. Li, W.W. Cai, J.H. An, S. Kim, J. Nah, D.X. Yang, R. Piner, A. Velamakanni, I. Jung, E. Tutuc, S.K. Banerjee, L. Colombo, R.S. Ruoff, Large-Area Synthesis of High-Quality and Uniform Graphene Films on Copper Foils, Science, 324 (2009) 1312-1314.
[18] C. Mattevi, H. Kim, M. Chhowalla, A Review of Chemical Vapour Deposition of Graphene on Copper, Journal of Materials Chemistry, 21 (2011) 3324-3334.
[19] H. Gao, Z. Liu, L. Song, W.H. Guo, W. Gao, L.J. Ci, A. Rao, W.J. Quan, R. Vajtai, P.M. Ajayan, Synthesis of S-Doped Graphene by Liquid Precursor, Nanotechnology, 23 (2012) 275605.
[20] H. Gao, L. Song, W.H. Guo, L. Huang, D.Z. Yang, F.C. Wang, Y.L. Zuo, X.L. Fan, Z. Liu, W. Gao, R. Vajtai, K. Hackenberg, P.M. Ajayan, A Simple Method to Synthesize Continuous Large Area Nitrogen-Doped Graphene, Carbon, 50 (2012) 4476-4482.
[21] L. Guo, X.K. Chen, L.X. Wang, S.Z. Gao, X.H. Bai, C. Zhang, Y.M. He, H. Gao, Controllable Synthesis of Single-Crystal Monolayer Graphene on Copper Foils by Low-Pressure Chemical Vapor Deposition, InKey Engineering Materials, 562-565 (2013) 79-84.
[22] O.K. Park, M.G. Hahm, S. Lee, H.I. Joh, S.I. Na, R. Vajtai, J.H. Lee, B.C. Ku, P.M. Ajayan, In Situ Synthesis of Thermochemically Reduced Graphene Oxide Conducting Nanocomposites, Nano Letters, 12 (2012) 1789-1793.

[23] H. Wang, G.Z. Wang, P.F. Bao, S.L. Yang, W. Zhu, X. Xie, W.J. Zhang, Controllable Synthesis of Submillimeter Single-Crystal Monolayer Graphene Domains on Copper Foils by Suppressing Nucleation, Journal of the American Chemical Society, 134 (2012) 3627-3630.
[24] Q.K. Yu, L.A. Jauregui, W. Wu, R. Colby, J.F. Tian, Z.H. Su, H.L. Cao, Z.H. Liu, D. Pandey, D.G. Wei, T.F. Chung, P. Peng, N.P. Guisinger, E.A. Stach, J.M. Bao, S.S. Pei, Y.P. Chen, Control and Characterization of Individual Grains and Grain Boundaries in Graphene Grown by Chemical Vapour Deposition, Nature Materials, 10 (2011) 443-449.
[25] J. Zhang, P.A. Hu, X.N. Wang, Z.L. Wang, D.Q. Liu, B. Yang, W.W. Cao, CVD Growth of Large Area and Uniform Graphene on Tilted Copper Foil for High Performance Flexible Transparent Conductive Film, Journal of Materials Chemistry, 22 (2012) 18283-18290.
[26] Mattheis.Lf, Band Structures of Transition-Metal-Dichalcogenide Layer Compounds, Physical Review B, 8 (1973) 3719-3740.
[27] Z.J. Zhang, J. Zhang, Q.J. Xue, Synthesis and Characterization of a Molybdenum-Disulfide Nanocluster, The Journal of Physical Chemistry, 98 (1994) 12973-12977.
[28] P.D. Fleischauer, R. Bauer, Chemical and Structural Effects on the Lubrication Properties of Sputtered Mos2 Films, Tribology Transactions, 31 (1988) 239-250.
[29] P.D. Fleischauer, Effects of Crystallite Orientation on Environmental Stability and Lubrication Properties of Sputtered MoS2 Thin-Films, ASLE Transactions, 27 (1984) 82-88.
[30] H.S. Lee, S.W. Min, Y.G. Chang, M.K. Park, T. Nam, H. Kim, J.H. Kim, S. Ryu, S. Im, MoS2 Nanosheet Phototransistors with Thickness-Modulated Optical Energy Gap, Nano Letters, 12 (2012) 3695-3700.
[31] G. Eda, H. Yamaguchi, D. Voiry, T. Fujita, M.W. Chen, M. Chhowalla, Photoluminescence from Chemically Exfoliated MoS2, Nano Letters, 12 (2012) 5111-5116.
[32] T. Cao, G. Wang, W.P. Han, H.Q. Ye, C.R. Zhu, J.R. Shi, Q. Niu, P.H. Tan, E. Wang, B.L. Liu, J. Feng, Valley-Selective Circular Dichroism of Monolayer Molybdenum Disulphide, Nature Communications, 3 (2012) 887.
[33] A. Splendiani, L. Sun, Y.B. Zhang, T.S. Li, J. Kim, C.Y. Chim, G. Galli, F. Wang, Emerging Photoluminescence in Monolayer MoS2, Nano Letters, 10 (2010) 1271-1275.
[34] B. Radisavljevic, M.B. Whitwick, A. Kis, Integrated Circuits and Logic Operations Based on Single-Layer MoS2, ACS Nano, 5 (2011) 9934-9938.

[35] S. Kim, A. Konar, W.S. Hwang, J.H. Lee, J. Lee, J. Yang, C. Jung, H. Kim, J.B. Yoo, J.Y. Choi, Y.W. Jin, S.Y. Lee, D. Jena, W. Choi, K. Kim, High-Mobility and Low-Power Thin-Film Transistors Based on Multilayer MoS2 Crystals, Nature Communications, 3 (2012) 1011.
[36] K.K. Liu, W.J. Zhang, Y.H. Lee, Y.C. Lin, M.T. Chang, C. Su, C.S. Chang, H. Li, Y.M. Shi, H. Zhang, C.S. Lai, L.J. Li, Growth of Large-Area and Highly Crystalline MoS2 Thin Layers on Insulating Substrates, Nano Letters, 12 (2012) 1538-1544.
[37] V. Podzorov, M.E. Gershenson, C. Kloc, R. Zeis, E. Bucher, High-Mobility Field-Effect Transistors Based on Transition Metal Dichalcogenides, Applied Physics Letters, 84 (2004) 3301-3303.
[38] B. Radisavljevic, A. Radenovic, J. Brivio, V. Giacometti, A. Kis, Single-Layer MoS2 Transistors, Nature Nanotechnology, 6 (2011) 147-150.
[39] B. Seger, A.B. Laursen, P.C.K. Vesborg, T. Pedersen, O. Hansen, S. Dahl, I. Chorkendorff, Hydrogen Production Using a Molybdenum Sulfide Catalyst on a Titanium-Protected n plus p-Silicon Photocathode, Angewandte Chemie International Edition, 51 (2012) 9128-9131.
[40] L.P. Hansen, Q.M. Ramasse, C. Kisielowski, M. Brorson, E. Johnson, H. Topsoe, S. Helveg, Atomic-Scale Edge Structures on Industrial-Style MoS2 Nanocatalysts, Angewandte Chemie International Edition, 50 (2011) 10153-10156.
[41] T.F. Jaramillo, K.P. Jorgensen, J. Bonde, J.H. Nielsen, S. Horch, I. Chorkendorff, Identification of Active Edge Sites for Electrochemical H2 Evolution from MoS2 Nanocatalysts, Science, 317 (2007) 100-102.
[42] J.V. Lauritsen, M. Nyberg, J.K. Norskov, B.S. Clausen, H. Topsoe, E. Laegsgaard, F. Besenbacher, Hydrodesulfurization Reaction Pathways on MoS2 Nanoclusters Revealed by Scanning Tunneling Microscopy, Journal of Catalysis, 224 (2004) 94-106.
[43] M.L. Tsai, S.H. Su, J.K. Chang, D.S. Tsai, C.H. Chen, C.I. Wu, L.J. Li, L.J. Chen, J.H. He, Monolayer MoS2 Heterojunction Solar Cells, ACS Nano, 8 (2014) 8317-8322.
[44] E. Singh, K.S. Kim, G.Y. Yeom, H.S. Nalwa, Atomically Thin-Layered Molybdenum Disulfide (MoS2) for Bulk-Heterojunction Solar Cells, ACS Applied Materials & Interfaces, 9 (2017) 3223-3245.
[45] D.C. Guozhen Shen, One-Dimensional Nanostructures for Electronic and Optoelectronic Devices, Frontiers of Optoelectronics in China, 3 (2010) 125-138.

[46] Y. Li, F. Qian, J. Xiang, C.M. Lieber, Nanowire Electronic and Optoelectronic Devices, Materials Today, 9 (2006) 18-27.
[47] J. Zhang, P.C. Chen, G.Z. Shen, J.B. He, A. Kumbhar, C.W. Zhou, J.Y. Fang, p-Type Field-Effect Transistors of Single-Crystal Zinc Telluride Nanobelts, Angewandte Chemie International Edition, 47 (2008) 9469-9471.
[48] X.F. Duan, Y. Huang, Y. Cui, J.F. Wang, C.M. Lieber, Indium Phosphide Nanowires as Building Blocks for Nanoscale Electronic and Optoelectronic Devices, Nature, 409 (2001) 66-69.
[49] Y. Huang, X.F. Duan, Y. Cui, L.J. Lauhon, K.H. Kim, C.M. Lieber, Logic Gates and Computation from Assembled Nanowire Building Blocks, Science, 294 (2001) 1313-1317.
[50] G.Z. Shen, Y. Bando, J.Q. Hu, D. Golberg, High-Symmetry ZnS Hepta- and Tetrapods Composed of Assembled ZnS Nanowire Arrays, Applied Physics Letters, 90 (2007) 123101.
[51] G.Z. Shen, Y. Bando, C.H. Ye, X.L. Yuan, T. Sekiguchi, D. Golberg, Single-Crystal Nanotubes of II3-V-2 Semiconductors, Angewandte Chemie International Edition, 45 (2006) 7568-7572.
[52] X.F. Qiu, Y.B. Lou, A.C.S. Samia, A. Devadoss, J.D. Burgess, S. Dayal, C. Burda, PbTe Nanorods by Sonoelectrochemistry, Angewandte Chemie International Edition, 44 (2005) 5855-5857.
[53] J.D. Meindl, Q. Chen, J.A. Davis, Limits on Silicon Nanoelectronics for Terascale Integration, Science, 293 (2001) 2044-2049.
[54] P.C. Chen, G.Z. Shen, C.W. Zhou, Chemical Sensors and Electronic Noses Based on 1-D Metal Oxide Nanostructures, IEEE Transactions on Nanotechnology, 7 (2008) 668-682.
[55] X.F. Duan, Y. Huang, R. Agarwal, C.M. Lieber, Single-Nanowire Electrically Driven Lasers, Nature, 421 (2003) 241-245.
[56] Z.H. Zhong, F. Qian, D.L. Wang, C.M. Lieber, Synthesis of p-Type Gallium Nitride Nanowires for Electronic and Photonic Nanodevices, Nano Letters, 3 (2003) 343-346.
[57] Y.Q. Zheng, J.Y. Wang, J. Pei, One-Dimensional (1D) Micro/Nanostructures of Organic Semiconductors for Field-Effect Transistors, Science China Chemistry, 58 (2015) 937-946.
[58] T. Hasegawa, J. Takeya, Organic Field-Effect Transistors Using Single Crystals, Science and Technology of Advanced Materials, 10 (2009) 024314.
[59] C. Reese, Z.N. Bao, Organic Single-Crystal Field-Effect Transistors, Materials Today, 10 (2007) 20-27.

[60] C.D. Dimitrakopoulos, D.J. Mascaro, Organic Thin-Film Transistors: A Review of Recent Advances, IBM Journal of Research and Development, 45 (2001) 11-27.
[61] H. Hoppe, N.S. Sariciftci, Organic Solar Cells: An Overview, Journal of Materials Research, 19 (2004) 1924-1945.
[62] R.B. Laprairie, A.M. Bagher, M.E.M. Kelly, D.J. Dupre, E.M. Denovan-Wright, Type 1 Cannabinoid Receptor Ligands Display Functional Selectivity in a Cell Culture Model of Striatal Medium Spiny Projection Neurons, Journal of Biological Chemistry, 289 (2014) 24845-24862.
[63] F.C. Krebs, J. Alstrup, H. Spanggaard, K. Larsen, E. Kold, Production of Large-Area Polymer Solar Cells by Industrial Silk Screen Printing, Lifetime Considerations and Lamination with Polyethyleneterephthalate, Solar Energy Materials and Solar Cells, 83 (2004) 293-300.
[64] H. Spanggaard, F.C. Krebs, A Brief History of the Development of Organic and Polymeric Photovoltaics, Solar Energy Materials and Solar Cells, 83 (2004) 125-146.
[65] S. Karg, W. Riess, V. Dyakonov, M. Schwoerer, Electrical and Optical Characterization of Poly(Phenylene-Vinylene) Light-Emitting-Diodes, Synthetic Metals, 54 (1993) 427-433.
[66] C.W. Tang, 2-Layer Organic Photovoltaic Cell, Applied Physics Letters, 48 (1986) 183-185.
[67] J. You, L. Dou, K. Yoshimura, T. Kato, K. Ohya, T. Moriarty, K. Emery, C.C. Chen, J. Gao, G. Li, Y. Yang, A Polymer Tandem Solar Cell with 10.6% Power Conversion Efficiency, Nature Communications, 4 (2013) 1446.
[68] M.A. Green, K. Emery, Y. Hishikawa, W. Warta, E.D. Dunlop, Solar Cell Efficiency Tables, Progress in Photovoltaics: Research and Applications, 23 (2015) 805-812.
[69] B. Kan, Q. Zhang, M. Li, X. Wan, W. Ni, G. Long, Y. Wang, X. Yang, H. Feng, Y. Chen, Solution-Processed Organic Solar Cells Based on Dialkylthiol-Substituted Benzodithiophene Unit with Efficiency Near 10%, Journal of the American Chemical Society, 136 (2014) 15529-15532.
[70] M.C. Scharber, D. Wuhlbacher, M. Koppe, P. Denk, C. Waldauf, A.J. Heeger, C.L. Brabec, Design Rules for Donors in Bulk-Heterojunction Solar Cells - Towards 10 % Energy-Conversion Efficiency, Advanced Materials, 18 (2006) 789-794.
[71] W.R. Cao, J.G. Xue, Recent Progress in Organic Photovoltaics: Device Architecture and Optical Design, Energy & Environmental Science, 7 (2014) 2123-2144.
[72] A.M. Bagher, Introduction to Organic Solar Cells, Sustainable Energy, 2 (2014) 85-90.
[73] N.S. Sariciftci, L. Smilowitz, A.J. Heeger, F. Wudl, Photoinduced Electron-Transfer from a Conducting Polymer to Buckminsterfullerene, Science, 258 (1992) 1474-1476.

[74] W.L. Ma, C.Y. Yang, X. Gong, K. Lee, A.J. Heeger, Thermally Stable, Efficient Polymer Solar Cells with Nanoscale Control of the Interpenetrating Network Morphology, Advanced Functional Materials, 15 (2005) 1617-1622.
[75] G. Li, V. Shrotriya, Y. Yao, Y. Yang, Investigation of Annealing Effects and Film Thickness Dependence of Polymer Solar Cells Based on Poly(3-hexylthiophene), Journal of Applied Physics, 98 (2005) 043704.
[76] G.D. Wei, S.Y. Wang, K. Sun, M.E. Thompson, S.R. Forrest, Solvent-Annealed Crystalline Squaraine: PC70BM (1:6) Solar Cells, Advanced Energy Materials, 1 (2011) 184-187.
[77] M.T. Dang, L. Hirsch, G. Wantz, P3HT:PCBM, Best Seller in Polymer Photovoltaic Research, Advanced Materials, 23 (2011) 3597-3602.
[78] C.W. Chu, V. Shrotriya, G. Li, Y. Yang, Tuning Acceptor Energy Level for Efficient Charge Collection in Copper-Phthalocyanine-Based Organic Solar Cells, Applied Physics Letters, 88 (2006) 153504.
[79] F. Padinger, R.S. Rittberger, N.S. Sariciftci, Effects of Postproduction Treatment on Plastic Solar Cells, Advanced Functional Materials, 13 (2003) 85-88.
[80] D. Muhlbacher, M. Scharber, M. Morana, Z.G. Zhu, D. Waller, R. Gaudiana, C. Brabec, High Photovoltaic Performance of a Low-Bandgap Polymer, Advanced Materials, 18 (2006) 2884-2889.
[81] S. Morita, A.A. Zakhidov, K. Yoshino, Doping Effect of Buckminsterfullerene in Conducting Polymer - Change of Absorption-Spectrum and Quenching of Luminescence, Solid State Communications, 82 (1992) 249-252.
[82] L. Smilowitz, N.S. Sariciftci, C. Gettinger, A.J. Heeger, F. Wudl, G. Wang, J.E. Bowers, Photoexcitation Spectroscopy of Photoinduced Electron-Transfer in Conducting Polymer-Buckminsterfullerene Composites, International Society for Optics and Photonics, 1852 (1993) 316-326.
[83] L. Smilowitz, N.S. Sariciftci, R. Wu, C. Gettinger, A.J. Heeger, F. Wudl, Photoexcitation Spectroscopy of Conducting-Polymer-C60 Composites - Photoinduced Electron-Transfer, Physical Review B, 47 (1993) 13835-13842.
[84] S. Gunes, H. Neugebauer, N.S. Sariciftci, Conjugated Polymer-Based Organic Solar Cells, Chemical Reviews, 107 (2007) 1324-1338.

[85] M.M. Wienk, J.M. Kroon, W.J.H. Verhees, J. Knol, J.C. Hummelen, P.A. van Hal, R.A.J. Janssen, Efficient Methano[70]Fullerene/MDMO-PPV Bulk Heterojunction Photovoltaic Cells, Angewandte Chemie International Edition, 42 (2003) 3371-3375.
[86] Y.Y. Liang, Z. Xu, J.B. Xia, S.T. Tsai, Y. Wu, G. Li, C. Ray, L.P. Yu, For the Bright Future-Bulk Heterojunction Polymer Solar Cells with Power Conversion Efficiency of 7.4%, Advanced Materials, 22 (2010) 135-138.
[87] L. Wang, Q. Chen, G.B. Pan, L.J. Wan, S.M. Zhang, X.W. Zhan, B.H. Northrop, P.J. Stang, Nanopatterning of Donor/Acceptor Hybrid Supramolecular Architectures on Highly Oriented Pyrolytic Graphite: a Scanning Tunneling Microscopy Study, Journal of the American Chemical Society, 130 (2008) 13433-13441.
[88] Y.H. Kim, C. Sachse, M.L. Machala, C. May, L. Muller-Meskamp, K. Leo, Highly Conductive PEDOT:PSS Electrode with Optimized Solvent and Thermal Post-Treatment for ITO-Free Organic Solar Cells, Advanced Functional Materials, 21 (2011) 1076-1081.
[89] L. D'Olieslaeger, M. Pfannmoller, E. Fron, I. Cardinaletti, M. Van der Auweraer, G. Van Tendeloo, S. Bals, W. Maes, D. Vanderzande, J. Manca, A. Ethirajan, Tuning of PCDTBT:PC71BM Blend Nanoparticles for Eco-Friendly Processing of Polymer Solar Cells, Solar Energy Materials and Solar Cells, 159 (2017) 179-188.
[90] Z.Y. Liu, W.G. Jiang, W. Li, L. Hong, T. Lei, D.B. Mi, R.X. Peng, X.H. Ouyang, Z.Y. Ge, Reducible Fabrication Cost for P3HT-Based Organic Solar Cells by Using One-Step Synthesized Novel Fullerene Derivative, Solar Energy Materials and Solar Cells, 159 (2017) 172-178.
[91] Y. Xie, P. Dutta, D. Cengher, V. Bommisetty, J. Li, D. Galipeau, Q.Q. Qiao, Solvent Effect on the Morphology of P3HT/PCBM Films, Proceedings of SPIE, 7416 (2009) 74161Q.
[92] D. Coffey, D. Ginger, Mapping Nanoscale Efficiency Variations in Plastic Solar Cells, SPIE-the International Society for Optical Engineering, 2 (2007) 636-638.
[93] Y. Minami, H. Yamaki, I. Katayama, J. Takeda, Broadband Pump-Probe Imaging Spectroscopy Applicable to Ultrafast Single-Shot Events, Applied Physics Express, 7 (2014) 022402.
[94] G. Binning, H. Rohrer, C. Gerber, E. Weibel, Surface Studies by Scanning Tunneling Microscopy, Physical Review Letters, 49 (1982) 57-61.
[95] G. Binnig, H. Rohrer, C. Gerber, E. Weibel, Tunneling through a Controllable Vacuum Gap, Applied Physics Letters, 40 (1982) 178-180.

[96] F. Besenbacher, Scanning Tunnelling Microscopy Studies of Metal Surfaces, Reports on Progress in Physics, 59 (1996) 1737-1802.
[97] F. Besenbacher, E. Laegsgaard, K. Mortensen, U. Nielsen, I. Stensgaard, Compact, High-Stability, Thimble-Size Scanning Tunneling Microscope, Review of Scientific Instruments, 59 (1988) 1035-1038.
[98] J.H. Ferris, J.G. Kushmerick, J.A. Johnson, M.G.Y. Youngquist, R.B. Kessinger, H.F. Kingsbury, P.S. Weiss, Design, Operation, and Housing of an Ultrastable, Low Temperature, Ultrahigh Vacuum Scanning Tunneling Microscope, Review of Scientific Instruments, 69 (1998) 2691-2695.
[99] J.A. Jensen, K.B. Rider, Y. Chen, M. Salmeron, G.A. Somorjai, High Pressure, High Temperature Scanning Tunneling Microscopy, Journal of Vacuum Science & Technology B: Microelectronics and Nanometer Structures Processing, Measurement, and Phenomena, 17 (1999) 1080-1084.
[100] M. Kugler, C. Renner, O. Fischer, V. Mikheev, G. Batey, A He-3 Refrigerated Scanning Tunneling Microscope in High Magnetic Fields and Ultrahigh Vacuum, Review of Scientific Instruments, 71 (2000) 1475-1478.
[101] B.J. Mcintyre, M. Salmeron, G.A. Somorjai, A Variable Pressure Temperature Scanning Tunneling Microscope for Surface Science and Catalysis Studies, Review of Scientific Instruments, 64 (1993) 687-691.
[102] J. Bardeen, Tunnelling from a Many-Particle Point of View, Physical Review Letters, 6 (1961) 57-59.
[103] T. Chenggang, Fluctuations on Metal Surfaces and Molecule/Metal Interfaces, University of Maryland, 2007.
[104] C.J. Chen, Introduction to Scanning Tunneling Microscopy, Oxford University Press, 1993.
[105] R. Wiesendanger, Contributions of Scanning Probe Microscopy and Spectroscopy to the Investigation and Fabrication of Nanometer-Scale Structures, Journal of Vacuum Science & Technology B: Microelectronics and Nanometer Structures Processing, Measurement, and Phenomena, 12 (1994) 515-529.
[106] J. Tersoff, D.R. Hamann, Theory and Application for the Scanning Tunneling Microscope, Physical Review Letters, 50 (1983) 1998-2001.

[107] R. Wiesendanger, Scanning Probe Microscopy and Spectroscopy : Methods and Applications, Cambridge University Press, 1994.
[108] A.P. Labonté, Scanning Tunneling Spectroscopy on Organic Molecules, Purdue University, 2002.
[109] K.M. Kadish, R.S. Ruoff, Fullerenes: Chemistry, Physics, and Technology, John Wiley & Sons, 2000.
[110]G.Dresselhaus, P.C. Eklund, M.S. Dresselhaus, Science of Fullerenes and Carbon Nanotubes: Their Properties and Applications, Academic Press, 1996.
[111] H. Liu, P. Reinke, C60 Thin Film Growth on Graphite: Coexistence of Spherical and Fractal-Dendritic Islands, The Journal of Chemical Physics, 124 (2006) 164707.
[112] H.B. Yu, J.J. Yan, Y.F. Li, W.S. Yang, Z.N. Gu, Y.Q. Wu, Scanning Tunneling Microscopy of C60 on Graphite, Surface Science, 286 (1993) 116-121.
[113] D.J. Kenny, R.E. Palmer, Nucleation and Growth of C60 Thin Films on Graphite, Surface Science, 447 (2000) 126-132.
[114] T. Hashizume, K. Motai, X.D. Wang, H. Shinohara, Y. Saito, Y. Maruyama, K. Ohno, Y. Kawazoe, Y. Nishina, H.W. Pickering, Y. Kuk, T. Sakurai, Intramolecular Structures of C60 Molecules Adsorbed on the Cu(111)-(1x1) Surface, Physical Review Letters, 71 (1993) 2959-2962.
[115] W. Harneit, Fullerene-Based Electron-Spin Quantum Computer, Physical Review A, 65 (2002) 032322.
[116] G. Burkard, D. Loss, D.P. DiVincenzo, Coupled Quantum Dots as Quantum Gates, Physical Review B, 59 (1999) 2070-2078.
[117] C. Joachim, M.A. Ratner, Molecular Electronics: Some Views on Transport Junctions and Beyond, Proceedings of the National Academy of Sciences of the United States of America, 102 (2005) 8801-8808.
[118] D.J. Hornbaker, S.J. Kahng, S. Misra, B.W. Smith, A.T. Johnson, E.J. Mele, D.E. Luzzi, A. Yazdani, Mapping the One-Dimensional Electronic States of Nanotube Peapod Structures, Science, 295 (2002) 828-831.
[119] B.W. Smith, M. Monthioux, D.E. Luzzi, Encapsulated C60 in Carbon Nanotubes, Nature, 396 (1998) 323-324.
[120] H.L. Zhang, W. Chen, L. Chen, H. Huang, X.S. Wang, J. Yuhara, A.T.S. Wee, C60 Molecular Chains on A-Sexithiophene Nanostripes, Small, 3 (2007) 2015-2018.

[121] A. Tamai, W. Auwarter, C. Cepek, F. Baumberger, T. Greber, J. Osterwalder, One-Dimensional Chains of C60 Molecules on Cu(221), Surface Science, 566 (2004) 633-637.
[122] C.G. Zeng, B. Wang, B. Li, H.Q. Wang, J.G. Hou, Self-assembly of One-Dimensional Molecular and Atomic Chains Using Striped Alkanethiol Structures as Templates, Applied Physics Letters, 79 (2001) 1685-1687.
[123] H.I. Rasool, E.B. Song, M.J. Allen, J.K. Wassei, R.B. Kaner, K.L. Wang, B.H. Weiller, J.K. Gimzewski, Continuity of Graphene on Polycrystalline Copper, Nano Letters, 11 (2011) 251-256.
[124] J. Cho, L. Gao, J.F. Tian, H.L. Cao, W. Wu, Q.K. Yu, E.N. Yitamben, B. Fisher, J.R. Guest, Y.P. Chen, N.P. Guisinger, Atomic-Scale Investigation of Graphene Grown on Cu Foil and the Effects of Thermal Annealing, ACS Nano, 5 (2011) 3607-3613.
[125] H. Ulbricht, G. Moos, T. Hertel, Interaction of C60 with Carbon Nanotubes and Graphite, Physical Review Letters, 90 (2003) 095501.
[126] H.I. Rasool, E.B. Song, M. Mecklenburg, B.C. Regan, K.L. Wang, B.H. Weiller, J.K. Gimzewski, Atomic-Scale Characterization of Graphene Grown on Copper (100) Single Crystals, Journal of the American Chemical Society, 133 (2011) 12536-12543.
[127] S.S. Wong, W.W. Pai, C.H. Chen, M.T. Lin, Coverage-Dependent Adsorption Superstructure Transition of C60/Cu(001), Physical Review B, 82 (2010) 125442.
[128] N. Xie, H.Q. Gong, Z. Zhou, X.D. Guo, S.C. Yan, Q. Sun, S.R. Xing, W. Wu, S.S. Pei, J.M. Bao, X.Y. Shan, Y. Guo, X.H. Lu, Visualization of a Maze-Like Reconstruction of Graphene on a Copper Surface at the Atomic Scale, Chinese Physics Letters, 30 (2013) 056802.
[129] L. Zhao, K.T. Rim, H. Zhou, R. He, T.F. Heinz, A. Pinczuk, G.W. Flynn, A.N. Pasupathy, Influence of Copper Crystal Surface on the CVD Growth of Large Area Monolayer Graphene, Solid State Communications, 151 (2011) 509-513.
[130] N. Reckinger, E. Van Hooijdonk, F. Joucken, A.V. Tyurnina, S. Lucas, J.F. Colomer, Anomalous Moir, Pattern of Graphene Investigated by Scanning Tunneling Microscopy: Evidence of Graphene Growth on Oxidized Cu(111), Nano Research, 7 (2014) 154-162.
[131] L. Gao, J.R. Guest, N.P. Guisinger, Epitaxial Graphene on Cu(111), Nano Letters, 10 (2010) 3512-3516.
[132] T.C. Niu, M. Zhou, J.L. Zhang, Y.P. Feng, W. Chen, Growth Intermediates for CVD Graphene on Cu(111): Carbon Clusters and Defective Graphene, Journal of the American Chemical Society, 135 (2013) 8409-8414.

[133] P. Sule, M. Szendro, C. Hwang, L. Tapaszto, Rotation Misorientated Graphene Moire Superlattices on Cu (111): Classical Molecular Dynamics Simulations and Scanning Tunneling Microscopy Studies, Carbon, 77 (2014) 1082-1089.
[134] W. Kim, K. Yoo, E.K. Seo, S.J. Kim, C. Hwang, Scanning Tunneling Microscopy Study on a Graphene Layer Grown on a Single-Crystal Cu(111) Surface by Using Chemical Vapor Deposition, Journal of the Korean Physical Society, 59 (2011) 71-74.
[135] I. Jeon, H. Yang, S.H. Lee, J. Heo, D.H. Seo, J. Shin, U.I. Chung, Z.G. Kim, H.J. Chung, S. Seo, Passivation of Metal Surface States: Microscopic Origin for Uniform Monolayer Graphene by Low Temperature Chemical Vapor Deposition, ACS Nano, 5 (2011) 1915-1920.
[136] S.Y. Kim, H.J. Hwang, J.W. Kang, One-Dimensional Self-Assembly of C60 Molecules on Periodically Wrinkled Graphene Sheet: A Monte Carlo Approach, Phys Lett A, 377 (2013) 3136-3143.
[137] J. Cho, J. Smerdon, L. Gao, O. Suzer, J.R. Guest, N.P. Guisinger, Structural and Electronic Decoupling of C60 from Epitaxial Graphene on SiC, Nano Letters, 12 (2012) 3018-3024.
[138] M. Jung, D. Shin, S.D. Sohn, S.Y. Kwon, N. Park, H.J. Shin, Atomically Resolved Orientational Ordering of C60 Molecules on Epitaxial Graphene on Cu(111), Nanoscale, 6 (2014) 11835-11840.
[139] L. Tapaszto, T. Dumitrica, S.J. Kim, P. Nemes-Incze, C. Hwang, L.P. Biro, Breakdown of Continuum Mechanics for Nanometre-Wavelength Rippling of Graphene, Nature Physics, 8 (2012) 739-742.
[140] J.S. Choi, Y.J. Chang, S. Woo, Y.W. Son, Y. Park, M.J. Lee, I.S. Byun, J.S. Kim, C.G. Choi, A. Bostwick, E. Rotenberg, B.H. Park, Correlation between Micrometer-Scale Ripple Alignment and Atomic-Scale Crystallographic Orientation of Monolayer Graphene, Scientific Reports , 4 (2014) 7263.
[141] D.W. Kim, J. Lee, S.J. Kim, S. Jeon, H.T. Jung, The Effects of the Crystalline Orientation of Cu Domains on the Formation of Nanoripple Arrays in CVD-Grown Graphene on Cu, Journal of Materials Chemistry C, 1 (2013) 7819-7824.
[142] Y.F. Zhang, T. Gao, Y.B. Gao, S.B. Xie, Q.Q. Ji, K. Yan, H.L. Peng, Z.F. Liu, Defect-Like Structures of Graphene on Copper Foils for Strain Relief Investigated by High-Resolution Scanning Tunneling Microscopy, ACS Nano, 5 (2011) 4014-4022.

[143] K.K. Bai, Y. Zhou, H. Zheng, L. Meng, H.L. Peng, Z.F. Liu, J.C. Nie, L. He, Creating One-Dimensional Nanoscale Periodic Ripples in a Continuous Mosaic Graphene Monolayer, Physical Review Letters, 113 (2014) 086102.
[144] Z.Wang, M. Devel, Periodic Ripples in Suspended Graphene, Physical Review B, 83 (2011) 125422.
[145] Q.H. Wang, M.C. Hersam, Nanofabrication of Heteromolecular Organic Nanostructures on Epitaxial Graphene via Room Temperature Feedback-Controlled Lithography, Nano Letters, 11 (2011) 589-593.
[146] P. Lauffer, K.V. Emtsev, R. Graupner, T. Seyller, L. Ley, Molecular and Electronic Structure of PTCDA on Bilayer Graphene on SiC(0001) Studied with Scanning Tunneling Microscopy, Physica Status Solidi B, 245 (2008) 2064-2067.
[147] H.T. Zhou, J.H. Mao, G. Li, Y.L. Wang, X.L. Feng, S.X. Du, K. Mullen, H.J. Gao, Direct Imaging of Intrinsic Molecular Orbitals Using Two-Dimensional, Epitaxially-Grown, Nanostructured Graphene for Study of Single Molecule and Interactions, Applied Physics Letters, 99 (2011) 153101.
[148] Q.H. Wang, M.C. Hersam, Room-Temperature Molecular-Resolution Characterization of Self-Assembled Organic Monolayers on Epitaxial Graphene, Nature Chemistry, 1 (2009) 206-211.
[149] J.M.P. Alaboson, Q.H. Wang, J.D. Emery, A.L. Lipson, M.J. Bedzyk, J.W. Elam, M.J. Pellin, M.C. Hersam, Seeding Atomic Layer Deposition of High-K Dielectrics on Epitaxial Graphene with Organic Self-Assembled Monolayers, ACS Nano, 5 (2011) 5223-5232.
[150] X.Q. Tian, J.B. Xu, X.M. Wang, Self-Assembly of PTCDA Ultrathin Films on Graphene: Structural Phase Transition and Charge Transfer Saturation, The Journal of Physical Chemistry C, 114 (2010) 20917-20924.
[151] J.D. Emery, Q.H. Wang, M. Zarrouati, P. Fenter, M.C. Hersam, M.J. Bedzyk, Structural Analysis of PTCDA Monolayers on Epitaxial Graphene with Ultra-High Vacuum Scanning Tunneling Microscopy and High-Resolution X-Ray Reflectivity, Surface Science, 605 (2011) 1685-1693.
[152] H. Huang, S. Chen, X.Y. Gao, W. Chen, A.T.S. Wee, Structural and Electronic Properties of PTCDA Thin Films on Epitaxial Graphene, ACS Nano, 3 (2009) 3431-3436.
[153] E.C.H. Sykes, Surface Assembly: Graphene Goes Undercover, Nature Chemistry, 1 (2009) 175-176.

[154] F.S. Tautz, Structure and Bonding of Large Aromatic Molecules on Noble Metal Surfaces: The Example of PTCDA, Progress in Surface Science, 82 (2007) 479-520.
[155] K. Glockler, C. Seidel, A. Soukopp, M. Sokolowski, E. Umbach, M. Bohringer, R. Berndt, W.D. Schneider, Highly Ordered Structures and Submolecular Scanning Tunnelling Microscopy Contrast of PTCDA and DM-PBDCI Monolayers on Ag(111) and Ag(110), Surface Science, 405 (1998) 1-20.
[156] Q.H. Wang, K. Kalantar-Zadeh, A. Kis, J.N. Coleman, M.S. Strano, Electronics and Optoelectronics of Two-Dimensional Transition Metal Dichalcogenides, Nature Nanotechnology, 7 (2012) 699-712.
[157] C.D. Zhang, A. Johnson, C.L. Hsu, L.J. Li, C.K. Shih, Direct Imaging of Band Profile in Single Layer MoS2 on Graphite: Quasiparticle Energy Gap, Metallic Edge States, and Edge Band Bending, Nano Letters, 14 (2014) 2443-2447.
[158] K.S. Novoselov, D. Jiang, F. Schedin, T.J. Booth, V.V. Khotkevich, S.V. Morozov, A.K. Geim, Two-Dimensional Atomic Crystals, Proceedings of the National Academy of Sciences of the United States of America, 102 (2005) 10451-10453.
[159] S. Bertolazzi, D. Krasnozhon, A. Kis, Nonvolatile Memory Cells Based on MoS2/Graphene Heterostructures, ACS Nano, 7 (2013) 3246-3252.
[160] K.C. Santosh, R.C. Longo, R. Addou, R.M. Wallace, K. Cho, Impact of Intrinsic Atomic Defects on the Electronic Structure of MoS2 Monolayers, Nanotechnology, 25 (2014) 375703.
[161] K.F. Mak, C. Lee, J. Hone, J. Shan, T.F. Heinz, Atomically Thin MoS2: A New Direct-Gap Semiconductor, Physical Review Letters, 105 (2010) 136805.
[162] J.K. Ellis, M.J. Lucero, G.E. Scuseria, The Indirect to Direct Band Gap Transition in Multilayered MoS2 as Predicted by Screened Hybrid Density Functional Theory, Applied Physics Letters, 99 (2011) 261908.
[163] Y.H. Lee, X.Q. Zhang, W.J. Zhang, M.T. Chang, C.T. Lin, K.D. Chang, Y.C. Yu, J.T.W. Wang, C.S. Chang, L.J. Li, T.W. Lin, Synthesis of Large-Area MoS2 Atomic Layers with Chemical Vapor Deposition, Advanced Materials, 24 (2012) 2320-2325.
[164] Y.M. Shi, W. Zhou, A.Y. Lu, W.J. Fang, Y.H. Lee, A.L. Hsu, S.M. Kim, K.K. Kim, H.Y. Yang, L.J. Li, J.C. Idrobo, J. Kong, Van der Waals Epitaxy of MoS2 Layers Using Graphene as Growth Templates, Nano Letters, 12 (2012) 2784-2791.

[165] M. Amani, M.L. Chin, A.G. Birdwell, T.P. O'Regan, S. Najmaei, Z. Liu, P.M. Ajayan, J. Lou, M. Dubey, Electrical Performance of Monolayer MoS2 Field-Effect Transistors Prepared by Chemical Vapor Deposition, Applied Physics Letters, 102 (2013) 193107.
[166] Y. Yoon, K. Ganapathi, S. Salahuddin, How Good Can Monolayer MoS2 Transistors Be?, Nano Letters, 11 (2011) 3768-3773.
[167] D. Lembke, A. Kis, Breakdown of High-Performance Monolayer MoS2 Transistors, ACS Nano, 6 (2012) 10070-10075.
[168] B. Radisavljevic, M.B. Whitwick, A. Kis, Integrated Circuits and Logic Operations Based on Single-Layer MoS2, ACS Nano, 5 (2011) 9934-9938.
[169] F. Banhart, J. Kotakoski, A.V. Krasheninnikov, Structural Defects in Graphene, ACS Nano, 5 (2011) 26-41.
[170] C.G. Tao, L.Y. Jiao, O.V. Yazyev, Y.C. Chen, J.J. Feng, X.W. Zhang, R.B. Capaz, J.M. Tour, A. Zettl, S.G. Louie, H.J. Dai, M.F. Crommie, Spatially Resolving Edge States of Chiral Graphene Nanoribbons, Nature Physics, 7 (2011) 616-620.
[171] O.V. Yazyev, R.B. Capaz, S.G. Louie, Theory of Magnetic Edge States in Chiral Graphene Nanoribbons, Physical Review B, 84 (2011) 115406.
[172] Q. Yu, L.A. Jauregui, W. Wu, R. Colby, J. Tian, Z. Su, H. Cao, Z. Liu, D. Pandey, D. Wei, T.F. Chung, P. Peng, N.P. Guisinger, E.A. Stach, J. Bao, S.-S. Pei, Y.P. Chen, Control and Characterization of Individual Grains and Grain Boundaries in Graphene Grown by Chemical Vapour Deposition, Nature Materials, 10 (2011) 443-449.
[173] R. Grantab, V.B. Shenoy, R.S. Ruoff, Anomalous Strength Characteristics of Tilt Grain Boundaries in Graphene, Science, 330 (2010) 946-948.
[174] Y. Wei, J. Wu, H. Yin, X. Shi, R. Yang, M. Dresselhaus, The Nature of Strength Enhancement and Weakening by Pentagon-Heptagon Defects in Graphene, Nature Materials, 11 (2012) 756-763.
[175] O.V. Yazyev, S.G. Louie, Electronic Transport in Polycrystalline Graphene, Nature Materials, 9 (2010) 806-809.
[176] L. Yang, M.L. Cohen, S.G. Louie, Magnetic Edge-State Excitons in Zigzag Graphene Nanoribbons, Physical Review Letters, 101 (2008) 186401.
[177] W. Zhou, S.J. Pennycook, J.-C. Idrobo, Localization of Inelastic Electron Scattering in the Low-Loss Energy Regime, Ultramicroscopy, 119 (2012) 51-56.

[178] H.G. Fuchtbauer, A.K. Tuxen, Z. Li, H. Topsoe, J.V. Lauritsen, F. Besenbacher, Morphology and Atomic-Scale Structure of MoS2 Nanoclusters Synthesized with Different Sulfiding Agents, Topics in Catalysis, 57 (2014) 207-214.
[179] Y. Li, H. Wang, L. Xie, Y. Liang, G. Hong, H. Dai, MoS2 Nanoparticles Grown on Graphene: an Advanced Catalyst for the Hydrogen Evolution Reaction, Journal of the American Chemical Society, 133 (2011) 7296-7299.
[180] X. Zong, H. Yan, G. Wu, G. Ma, F. Wen, L. Wang, C. Li, Enhancement of Photocatalytic H2 Evolution on CdS by Loading MoS2 as Cocatalyst under Visible Light Irradiation, Journal of the American Chemical Society, 130 (2008) 7176-7177.
[181] J. Shi, D. Ma, G.-F. Han, Y. Zhang, Q. Ji, T. Gao, J. Sun, X. Song, C. Li, Y. Zhang, X.-Y. Lang, Y. Zhang, Z. Liu, Controllable Growth and Transfer of Monolayer MoS2 on Au Foils and Its Potential Application in Hydrogen Evolution Reaction, ACS Nano, 8 (2014) 10196-10204.
[182] J.V. Lauritsen, M. Nyberg, J.K. Norskov, B.S. Clausen, H. Topsoe, E. Laegsgaard, F. Besenbacher, Hydrodesulferization Reaction Pathways on MoS2 Nanoclusters Revealed by Scanning Tunneling Microscopy, Journal of Catalysis, 224 (2004) 94-106.
[183] Y.F. Yu, C. Li, Y. Liu, L.Q. Su, Y. Zhang, L.Y. Cao, Controlled Scalable Synthesis of Uniform, High-Quality Monolayer and Few-Layer MoS2 Films, Scientific Reports, 3 (2013) 1866.
[184] Y.F. Yu, S.Y. Huang, Y.P. Li, S.N. Steinmann, W.T. Yang, L.Y. Cao, Layer-Dependent Electrocatalysis of MoS2 for Hydrogen Evolution, Nano Letters, 14 (2014) 553-558.
[185] C. Tsai, F. Abild-Pedersen, J.K. Norskov, Tuning the MoS2 Edge-Site Activity for Hydrogen Evolution via Support Interactions, Nano Letters, 14 (2014) 1381-1387.
[186] T. Cheiwchanchamnangij, W.R.L. Lambrecht, Quasiparticle Band Structure Calculation of Monolayer, Bilayer, and Bulk MoS2, Physical Review B, 85 (2012) 205302.
[187] S.Y. Xiao, M.K. Brannon, G.S. Armstrong, K. Fread, J. Ellena, J.H. Bushweller, C.V. Finkielstein, D.G.S. Capelluto, Tom1 Modulates the Endosomal Function of Tollip via a Folding-Upon-Binding Mechanism, Biophysical Journal, 108 (2015) 343a.
[188] K. Burns, J. Clatworthy, L. Martin, F. Martinon, C. Plumpton, B. Maschera, A. Lewis, K. Ray, J. Tschopp, F. Volpe, Tollip, a New Component of the IL-1RI Pathway, Links IRAK to the IL-1 Receptor, Nature Cell Biology, 2 (2000) 346-351.
[189] Y. Bulut, E. Faure, L. Thomas, O. Equils, M. Arditi, Cooperation of Toll-Like Receptor 2 and 6 for Cellular Activation by Soluble Tuberculosis Factor and Borrelia Burgdorferi Outer

Surface Protein A lipoprotein: Role of Toll-interacting Protein and IL-1 Receptor Signaling Molecules in Toll-Like Receptor 2 Signaling, The Journal of Immunology, 167 (2001) 987-994.
[190] D.G.S. Capelluto, Tollip: a Multitasking Protein in Innate Immunity and Protein Trafficking, Microbes and Infection, 14 (2012) 140-147.
[191] A. Engel, D.J. Muller, Observing Single Biomolecules at Work with the Atomic Force Microscope, Nature Structural & Molecular Biology, 7 (2000) 715-718.
[192] D.J. Muller, Y.F. Dufrene, Atomic Force Microscopy as a Multifunctional Molecular Toolbox in Nanobiotechnology, Nature Nanotechnology, 3 (2008) 261-269.
[193] E. Lesniewska, P.E. Milhiet, M.C. Giocondi, C. Le Grimellec, Atomic Force Microscope Imaging of Cells and Membranes, Methods in Cell Biology, 68 (2002) 51-65.
[194] S. Kasas, G. Dietler, Probing Nanomechanical Properties from Biomolecules to Living Cells, Pflügers Archiv-European Journal of Physiology, 456 (2008) 13-27.